Structural Characterization of Fe/Pd/Fe/GaAs(001) Thin Films by X-Ray Absorption Fine Structure Spectroscopy

by

Petr S. Budnik

M.Sc., Moscow State University, 1999

A Thesis Submitted In Partial Fulfillment of the
Requirements for the Degree of
Doctor of Philosophy

in the
Department of Physics
Faculty of Science

SIMON FRASER UNIVERSITY

Summer 2012

APPROVAL

Name:	Petr S. Budnik
Degree:	Doctor of Philosophy
Title of Thesis:	Structural Characterization of Fe/Pd/Fe/GaAs(001) Thin Films by X-ray Absorption Fine Structure Spectroscopy

Supervisory Committee: Dr. J. Steven Dodge, Associate Professor (Chair)

Dr. E. Daryl Crozier, Professor Emeritus
(Senior Supervisor)

Dr. Karen Kavanagh, Professor (Supervisor)

Dr. Bret Heinrich, Professor Emeritus (Supervisor)

Dr. Neil Alberding, Senior Lecturer
(Internal Examiner)

Dr. Tsun-Kong (T.K.) Sham, Professor, University of Western Ontario (External Examiner)

Date Approved: August 20, 2012

Partial Copyright Licence

The author, whose copyright is declared on the title page of this work, has granted to Simon Fraser University the right to lend this thesis, project or extended essay to users of the Simon Fraser University Library, and to make partial or single copies only for such users or in response to a request from the library of any other university, or other educational institution, on its own behalf or for one of its users.

The author has further granted permission to Simon Fraser University to keep or make a digital copy for use in its circulating collection (currently available to the public at the “Institutional Repository” link of the SFU Library website (www.lib.sfu.ca) at http://summit/sfu.ca and, without changing the content, to translate the thesis/project or extended essays, if technically possible, to any medium or format for the purpose of preservation of the digital work.

The author has further agreed that permission for multiple copying of this work for scholarly purposes may be granted by either the author or the Dean of Graduate Studies.

It is understood that copying or publication of this work for financial gain shall not be allowed without the author’s written permission.

Permission for public performance, or limited permission for private scholarly use, of any multimedia materials forming part of this work, may have been granted by the author. This information may be found on the separately catalogued multimedia material and in the signed Partial Copyright Licence.

While licensing SFU to permit the above uses, the author retains copyright in the thesis, project or extended essays, including the right to change the work for subsequent purposes, including editing and publishing the work in whole or in part, and licensing other parties, as the author may desire.

The original Partial Copyright Licence attesting to these terms, and signed by this author, may be found in the original bound copy of this work, retained in the Simon Fraser University Archive.

Simon Fraser University Library
Burnaby, British Columbia, Canada

revised Fall 2011

Abstract

The small lateral dimensions of spintronic devices and high density memory bits require the employment of magnetic ultrathin metallic film structures. Understanding the structure of such films is a critical component of developing the correct interpretation of their magnetic behaviour.

The Molecular Beam Epitaxy facility, MBE-1, was developed for use on the undulator beamline of the Pacific Northwest Consortium Collaborative Access Team at the Advanced Photon Source to permit *in situ* epitaxial growth of metal films and their structural characterization by synchrotron radiation techniques. In this thesis it was used to characterize the trilayer system iron/palladium/iron on GaAs(001). Three categories of samples were prepared and examined *in situ*. Iron films were deposited on the 4×6-reconstructed surface of GaAs(001) with thicknesses ranging from 0.5 to 38.5 monolayers. Palladium films were deposited on iron as follows: 1 monolayer palladium on 9 monolayers of iron, and 3.5 and 7 monolayers palladium on 38.5 monolayers of iron. Finally, iron films 4 and 10 monolayers thick were deposited on 7 monolayers of palladium on 38.5 monolayers of iron.

The polarization-dependent X-ray absorption fine structure (XAFS) technique in total reflection mode was employed to examine the samples and compare in-plane to out-of-plane structure in these films. This technique allows extracting identities of nearest neighbours, nearest neighbour radial distances, coordination numbers, and mean square relative displacement to characterize the probed system.

Iron and palladium K-edge spectra were obtained both above and below the critical angle for total reflection. Near 4 monolayers for iron films on GaAs(001), a transition from island to layer-by-layer growth modes is accompanied by the observation of a body-centered tetragonal structure with a c/a ratio of 1.030(8), with no thickness dependence observed up to 38.5 monolayers. The intermediate palladium layer shows a face-centered tetragonal structure. Alloying at the interface with the underlying iron is restricted to a depth of 0.5-1.0 monolayers. The upper layer of iron shows tetragonal distortion similar to the layers of iron grown on GaAs(001)-4×6. There is also evidence of alloy formation at the interface involving the underlying palladium with the thickness of the alloy region being 1.5-2.0 monolayers.

Acknowledgments

I would like to express my deepest gratitude to my supervisor, Prof. E. Daryl Crozier. His continuous support throughout the course of the work and tremendous scientific expertise were invaluable, and are greatly appreciated.

I also would like to thank Dr. Robert Gordon, the beamline scientist at the PNC-CAT, for generously sharing his knowledge and experience in operating the beamline and the MBE-1 system, and conducting XAFS experiments in general.

I would like to thank Prof. Bret Heinrich and Prof. Karen Kavanagh for their input on the subject of MBE growth and the structural analysis of thin films in the course of this work. I also wish to thank all of the members of my supervisory committee for their comments which were very helpful in the preparation for the thesis submission.

I would like to thank Prof. Steve Dodge and all of the Physics department administrative staff for their help in organizational proceedings leading to the defence.

And last, but not the least, I want to thank Mom, Dad and my grandparents for always being there for me, no matter what; Chandra for who she is; Karen for being wise; and Dan for being a great guy with a laptop.

Finally, I gratefully acknowledge the financial support provided by Simon Fraser University, the NSERC operational grant of Prof. E. Daryl Crozier, and the US Department of Energy grant for PNC-CAT operation.

Contents

List of Tables

List of Figures

Chapter 1

Review of the Literature

In this chapter the review of the literature relevant to the properties, fabrication and use of ultrathin magnetic films is presented. First, a short description of their characteristic magnetic properties and technological applications is given. Then, the structure of such films is discussed with the main focus being on iron films grown on a gallium arsenide substrate.

1.1 Magnetic Properties

The last two decades were marked by the constantly increasing interest in ultrathin ferromagnetic (FM) structures [1, 2, 3]. Giant Magneto Resistance (GMR) read-heads, for example, have proved to be crucial for the huge 100 % year-on-year increase in hard disk storage capacity. Spin-injection and spin filtering, on the other hand, opens exciting possibilities to revolutionize conventional semiconductor (SC) device physics by introducing the state of spin polarization as a new device parameter. In the core of these innovative developments is progress in the fabrication of ultrathin ferromagnetic films as well as advances in the understanding of their magnetic properties.

1.1.1 Magnetic Anisotropy

In this section a qualitative phenomenological description of magnetic anisotropy (MA) in ultrathin magnetic films will be given. By ultrathin magnetic films we refer to films with thickness comparable to or less than the exchange length, $l_{ex} = \sqrt{2A/\mu_0 M_S^2}$ length scale over which the exchange interaction is dominant compared to the demagnetizing energy. Here, A is the coefficient of the exchange interaction, $\mu_0 = 4\pi 10^7$ N·A^{-2} is the permeability of free space, and M_S is the saturation magnetization.

The anisotropy defines favorable (easy axis) and unfavorable (hard axis) directions of the magnetization with respect to the crystal axes and, therefore, plays an important role in magnetic properties of such ultrathin films. Since magnetic anisotropy is strongly related to the crystal symmetry of the sample, a general expression for the anisotropy energy is a complex function which reflects this symmetry (see, for example, [4]). Often, however, a uniaxial description is sufficient [1]:

$$E = -K \cos^2 \theta. \tag{1.1}$$

Here, E is the orientation dependent energy of magnetization, K is an anisotropy constant determining the anisotropy strength, and θ is the angle between the direction of magnetization and the sample normal. A second-order uniaxial term $K_2 \cos^4 \theta$ is sometimes needed to account for experimental observations, but, usually, is small. For the analysis of thin films it is useful to separate between volume (K_V) and surface (K_S) contributions to magnetic anisotropy K of a layer of thickness d:

$$K = K_V + \frac{2K_S}{d} \tag{1.2}$$

where K_V and K_S are normalized per unit volume and surface, respectively. The volume part favors in-plane magnetization, while the surface part favors perpendicular magnetization. Doubling the surface contribution accounts for two identical surfaces bounding the film, and in case of more complicated layered structures is modified accordingly.

The two main sources of magnetic anisotropy are magnetic dipolar interaction and spin-orbit interaction. The first one is a long range interaction between magnetic dipoles and creates a demagnetizing field. The energy of two dipoles $\overrightarrow{\mu_1}$ and $\overrightarrow{\mu_2}$ separated by distance r is given by

$$E_{dipole} = \frac{1}{r^3}(\overrightarrow{\mu_1} \cdot \overrightarrow{\mu_2} - \frac{3(\overrightarrow{\mu_1} \cdot \overrightarrow{r})(\overrightarrow{\mu_2} \cdot \overrightarrow{r})}{r^2}). \tag{1.3}$$

By treating the sample as a magnetic continuum and summing up over all dipoles the expression for the demagnetizing energy density is obtained:

$$E_D = \frac{1}{2}\mu_0 M_S^2 \cos^2 \theta. \tag{1.4}$$

As it can be seen, the magnetic dipolar anisotropy favors in-plane orientation for the magnetization. Since there is no dependence on the film thickness d, it enters only the volume part of anisotropy, K_V. For films of thickness of a few monolayers (ML), however, the sample should not be treated as a magnetic continuum, but as a collection of discrete magnetic dipoles. In this case, the average magnetic dipolar anisotropy will have both the volume and the surface anisotropy parts. Yet, the magnitude of its surface part is usually small compared to the surface contribution arising from spin-orbit coupling.

In the absence of spin-orbit interaction the total energy of electron-spin systems is independent of the direction of magnetization. In the presence of it, the total magnetic moment is coupled to the crystal lattice due to the crystal field, and, as a consequence, total energy becomes dependent on orientation of the magnetization relative to the crystal axes. The directional dependence gives the magnetocrystalline contribution to the magnetic anisotropy. In general, the magnetocrystalline anisotropy for cubic systems has three terms: perpendicular uniaxial anisotropy, in-plane uniaxial anisotropy and four-fold symmetry surface anisotropy due to lower symmetry.

In thin films, strain is induced due to to the lattice mismatch between the substrate and the deposited material, and this fact gives rise to a magnetoelastic anisotropy, E_{ME}. For systems with isotropic in-plane strain $\epsilon_{11} = \epsilon_{22} = \epsilon_{\|}$ and $\epsilon_{33} = \epsilon_{\perp}$ it is given by

$$E_{ME} = B_1(\epsilon_{\perp} - \epsilon_{\|}) \cos^2 \theta \tag{1.5}$$

where B_1 is the magnetostatic constant.

Additionally, roughness and interdiffusion between the film and the substrate and/or different layers of the films will result in changes to magnetic anisotropy, and, therefore, magnetic properties of the films. Roughness creates local demagnetizing fields at the surface and reduces the magnetic dipolar anisotropy [5]. Step atoms also reduce the magnetocrystalline contributions [6]. Interdiffusion introduces randomness in the magnetic pair bonds and also reduces the surface anisotropy. It is, therefore, important to know the structure of the sample to understand its magnetic properties.

Applications

Studies of magnetic films on semiconductors have not only deepened our understanding of magnetism in reduced dimensionality, but have also opened a door for new technological applications. Incorporation of magnetic elements into the world of semiconductor devices creates exciting new possibilities, a few of which are discussed in the following section.

Non-Volatile Magnetic Memory. Design of Magneto-resistive Random Access Memory (MRAM) [2] relies upon arrays of ferromagnetic sandwich structure (see Fig. 1.1). Each sandwich consists of two FM layers separated by an exchange breaking nonmagnetic (NM) layer between them. The magnetizations of the FM layers lie in the plane of the film but are antiparallel to each other. Such antiferromagnetic (AFM) coupling ensures that fringing fields from each FM layer are captured by each other, hence overcoming the problem of early MRAM design with parallel alignment of the magnetizations. This effectively allows a reduction in the size of the "bit".

A unique easy axis of magnetization is formed in the FM layers by depositing them in the presence of a reference magnetic field. The logical states of "0" and "1" are defined as two possible orientations of magnetization in FM layers (parallel/antiparallel or antiparallel/parallel for top/bottom layer) with respect to this fixed axis. The switching between two logical states is accomplished by a current pulse through an overlaid conducting line. The change of resistance in the FM/NM/FM sandwich structure under the influence of a small current in the same overlay line serves as the indication of the bit's logical state. The change is caused by altering the relative orientation of the magnetization and the sense current passing through the sandwich structure. Comparing to conventional designs of RAM such as

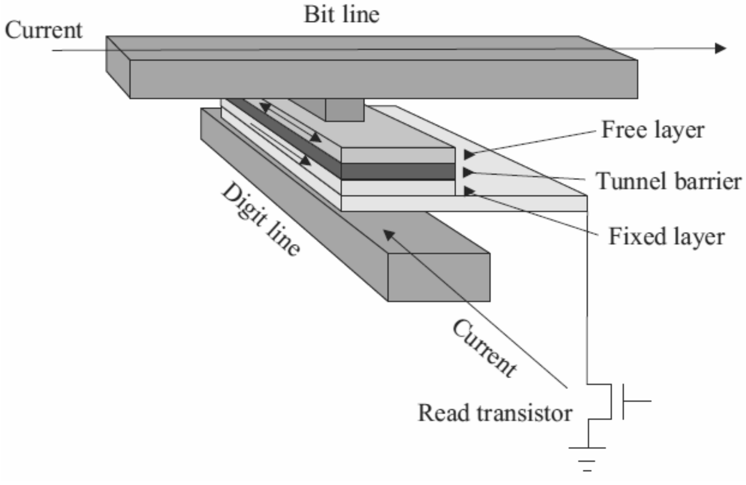

Figure 1.1: MRAM.

Dynamic RAM (DRAM), Static RAM (SRAM) and Flash RAM, MRAM is seen as somewhat "universal memory" [7]. It combines non-volatility, durability, fast read and write times and relatively low power consumption. While the recent advances in conventional RAM (notably Flash RAM) kept MRAM in a niche role in the market, it seems to be only a matter of time before MRAM becomes more widely employed and joins the mainstream of memory modules. At the same time MRAM is already being produced commercially and utilized in the special field of military and aerospace applications [8].

Microwave Devices. The effect of coupling of magnetization in thin magnetic films to a in-plane polarized microwave radiation field, $\overrightarrow{h}$, passing through it opens possibilities for creating compact devices to alter spectral characteristics of the radiation. Torque exerted by the in-plane component of the radiation $\overrightarrow{h}$ on magnetization vector $\overrightarrow{M_0}$ causes the former to exhibit gyroscopic rotation. The condition of resonance [2] when $\overrightarrow{h} \perp \overrightarrow{M_0}$ is given by $\omega_0 = 2\pi\nu_0 = \gamma\sqrt{H_{eff}(H_{eff} + 4\pi M_0)}$ where ω_0 is the cyclic frequency of the radiation, γ is the gyromagnetic ratio and $H_{eff} = H_{app} + H_{an}$ is the sum of the externally applied magnetic field and internal anisotropy field. For Fe films ($4\pi M_0 = 21.5$ kOe, $H_{an} = 0.5$ kOe) with no external field applied this resonance occurs at $\nu_0 \approx 10$ GHz, which is a useful frequency for microwave devices.

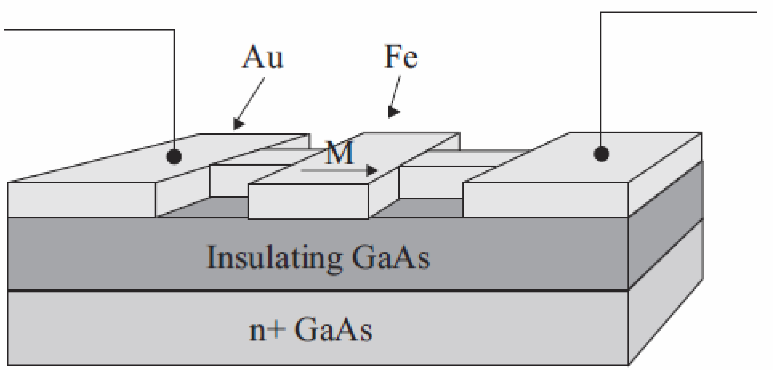

Figure 1.2: Microwave Spectral Filter.

A microwave device (see Fig. 1.2) is essentially a guided wave device in which microwave signal is injected on one side and picked up on the other via coaxial cables. It consists of a Si-doped n$^+$-GaAs layer (ground plate) and a ferromagnetic conducting strip separated by a GaAs insulating layer. Under the condition when the magnetization is parallel to the direction of the propagation of the radiation and $\overrightarrow{h} \perp \overrightarrow{M_0}$, the energy transfer from the radiation field into the film will occur via coupling. The coupling will be most effective only at the ferromagnetic resonance frequency and a sharp decrease in transmitted power will be observed making such device an effective spectral filter. The resonance frequency ω_0 can be shifted by applying an external magnetic field $\overrightarrow{H}_{app}$ parallel to the magnetization $\overrightarrow{M_0}$. If the applied magnetic field is applied perpendicular to $\overrightarrow{M_0}$ and is sufficiently large to reorient magnetization in the direction perpendicular to the signal propagation, the coupling between the radiation field and $\overrightarrow{M_0}$ is no longer present, effectively turning the filter "off".

The width of the power transmission drop is just the width of the ferromagnetic resonance in the film and is a measure of quality of the film and, consequently, of the device itself. Prinz et al. [9] have shown, for example, that epitaxial Fe films on ZnSe(001) exhibited the narrowest resonance width observed in a ferromagnetic, 45 Oe at 35 GHz, which is comparable to those in ferrimagnetic insulators, the materials widely used in high-frequency applications.

Spin-Injection Devices. The rapidly developing field of spintronics - devices that operate not only on the electrical charge of electrons, but also utilize their spin, - is, perhaps, one of the most exciting research areas in the physics of thin films. For several decades spin-polarized electrons have been created in a semiconductor by means of illuminating it with circularly polarized light. Yet, for electrical spintronic devices, which should not have to rely on optics, an electrical method of spin injection into semiconductors is required. While injecting spins from a dilute magnetic semiconductor in the presence of external magnetic field works well at temperatures below 4 K, with almost 100 % of the spins polarized in the direction of the applied field, at room temperature this method does not perform so well due to loss of spin-aligning characteristics by magnetic semiconductors just above 4 K. An alternative approach which relies on utilizing a thin ferromagnetic film involves injecting spin-polarized electrons from a ferromagnetic material, where almost all of the conducting electrons are intrinsically aligned, into a semiconductor. There are, however, difficulties related to this approach as well.

Most of the experiments on spin injection from a ferromagnetic contact are carried out using a spin-polarized field effect transistor (Spin-FET) design originally proposed by Datta et al. [10] (see Fig. 1.3). The spin-polarized carriers are injected into a two dimensional electron gas (2DEG) which provides a high electron mobility, free of spin-flip scattering events. They are created in the first ferromagnetic layer as a consequence of the different conductivities resulting from the different densities of states for spin-up and spin-down electrons in the ferromagnet. The second ferromagnetic layer serves as a spin collector. Perpendicular to the current, an internal electric field expected to exist in the heterostructure interface region (2DEG) will cause precession of spins due to spin-orbit coupling, effectively decreasing the spin current. The gate electrode deposited on top of the device allows to control the effect of the internal electric field by applying a gate voltage.

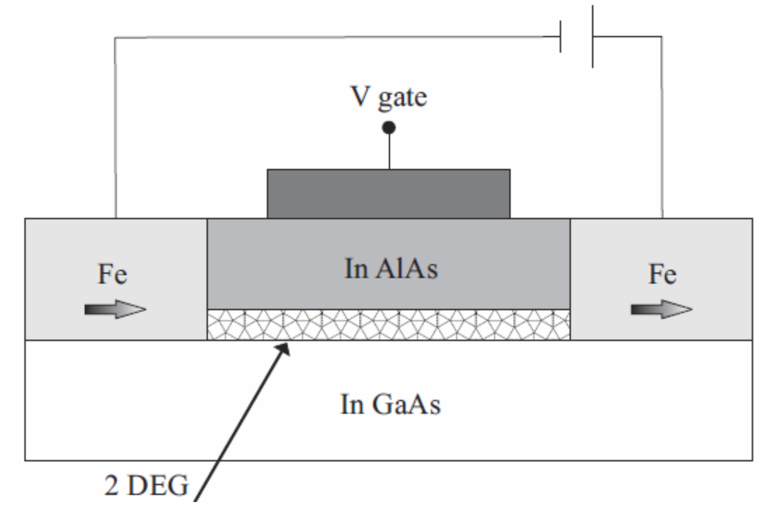

Figure 1.3: Spin FET. The spin-polarized carriers are injected from the left ferromagnetic pad into electron gas (2DEG) and collected in the right ferromagnetic pad.

Theoretical calculations done by Schmidt et al. [11] predict, however, that due to the resistance mismatch between ferromagnetic and 2DEG semiconductor with long spin-flip length, the spin injection efficiency will be low. By calculating the electrochemical potential they found the ratio $(R_{\uparrow\uparrow} - R_{\uparrow\downarrow})/R_{\uparrow\uparrow}$ to be equal ≈0.1 %, where $R_{\uparrow\uparrow}$ and $R_{\uparrow\downarrow}$ are resistances across the device for parallel and antiparallel magnetization. In addition, magnetically dead layers (randomly oriented spins) which can possibly form at the FM/SC interface due to intermixing would serve as a barrier for effective spin injection. It is important, therefore, to establish growth conditions under which such intermixing of the ferromagnetic layer and semiconductor substrate atoms is minimized.

Several experimental works, however, [12, 13] indicate that spin injection efficiency is not limited by the diffusion equation model: Fe layers on semiconductor form Schottky-type contacts which give rise to tunnelling under appropriate bias conditions. Such a tunneling process can lead to an enhanced spin injection efficiency, since it is not affected by the resistance mismatch. For example, Zhu et al. [12] report efficiency $(R_{\uparrow\uparrow} - R_{\uparrow\downarrow})/R_{\uparrow\uparrow} \approx 2$ %. They were one of the first to demonstrate that spin injection from the ferromagnetic metal Fe into the semiconductor GaAs is indeed possible. The spin polarization of injected electrons was detected by the circular polarization of the electroluminescence in an $\mathrm{In}_x\mathrm{Ga}_{1x}\mathrm{As}$/GaAs light emitting diode (LED) with the degree of polarization being directly proportional to spin injection efficiency. They showed that the tunnelling process does not depend on the temperature in accordance with the constant spin injection efficiency observed between 25 K and RT. Hanbicki et al. [13] using similar experimental technique to investigate Fe/$\mathrm{Al}_{0.1}\mathrm{Ga}_{0.9}\mathrm{As}$ achieved a significantly larger spin injection efficiency $(R_{\uparrow\uparrow} - R_{\uparrow\downarrow})/R_{\uparrow\uparrow} \approx 32$ %. Their detailed study of the transport mechanism through the metal/semiconductor interface gives conclusive evidence that Schottky-barrier tunnelling plays a significant role in it.

These experimental findings show that effective spin injection from ferromagnetic into semiconductor in Spin-FET can be achieved at RT, making commercial use of spintronics devices a matter of time.

1.2 Growth and Structure

1.2.1 Epitaxial Fe Films on GaAs(001)

Fe/GaAs(001) is an obvious and most widely used choice for the fabrication of an ultrathin ferromagnetic(FM)/semiconductor(SC) system. While Fe is a robust FM with high Curie temperature ($T_C^{Fe} = 1043$ K) [14] and high spin polarization, GaAs is a readily available III-V SC, which is widely used in todays SC industry and has well-known properties. The good epitaxial growth of Fe on GaAs is attributed to the fact that the lattice constant of body-centered cubic (bcc) Fe ($a_{Fe} = 2.866$ Å) is almost half that of GaAs ($a_{GaAs} = 5.645$ Å), yielding a relatively low misfit of $\nu = 1.4$ % in cube-on-cube epitaxy with Fe periodicity doubled compared to GaAs. In this section the more detailed specifics of epitaxial growth of Fe on GaAs will be presented.

GaAs(001)

The compound semiconductor GaAs has the cubic zincblende structure, which can be viewed as a face-centered cubic (fcc) lattice of Ga with another fcc lattice of As displaced by $\frac{\sqrt{3}}{4}a_{GaAs}$ in the [111] crystallographic direction (see Fig. 1.4). Such atomic structure gives rise to tetrahedral coordination. It has evenly spaced monoatomic (001) planes, resulting in the GaAs(001) surface being either Ga- or As-terminated. In the first case the upward-pointing Ga bonds all lie in the $(1\bar{1}0)$ plane, while in the second the upward As bonds are all in the orthogonal (110) plane.

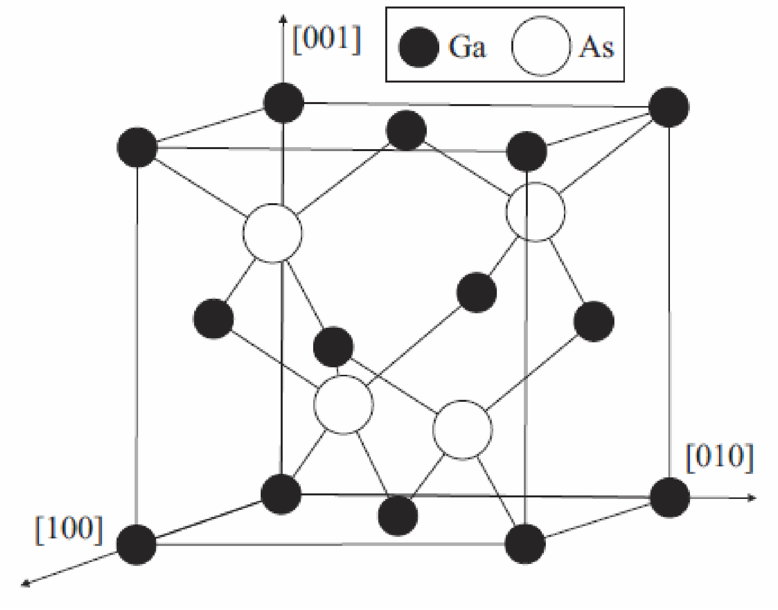

Figure 1.4: GaAs crystal structure.

The GaAs(001) surface is known to exhibit a whole range of surface reconstructions. A surface reconstruction of an ideal bulk-terminated surface is a significant rearrangement of surface atoms and modifications of the surface periodicity. In general the reconstructions on semiconductor surfaces are the result of the large surface free energy associated with the unpaired electrons (dangling bonds). While a detailed understanding of the reconstruction process requires complicated total-energy calculations [15], a few general principles have been derived from both calculations and experiments [16]. The relevant chemical, electronic and kinetic principles in the case of tetrahedrally coordinated compound semiconductors are [3]:

1. For a given surface stoichiometry, the surface atomic geometry is determined primarily by a rehybridization-induced lowering of the surface-state bands associated with the (filled) anion dangling bond orbitals.
2. Surfaces tend to be autocompensated ("non-metallicity" condition).
3. The surface structure observed will be the lowest energy structure kinetically accessible under the preparation conditions.

In the case of GaAs(001) these principles have the following implications:

The first principle results in the formation of dimers of Ga-Ga bonds or As-As bonds of adjacent surface atoms. This reduces the number of energetically unfavourable dangling bonds by half comparing to an ideal bulk-terminated surface. The surface dimers are formed along the direction of the dangling bonds and yield a surface periodicity twice as large as the bulk value parallel to the dimer directions: [110] on Ga-terminated surfaces and $[1\bar{1}0]$ on As-terminated surfaces. While there is an energy cost associated with surface dimerization due to induced surface and subsurface strain, for most low index faces of tetrahedrally coordinated semiconductors the energy gains due to rehybridization by far outweigh these costs.

The second principle determines the surface stoichiometry, by requiring that no charge accumulate at the surface. In general, a tetrahedrally coordinated atom contributes $Z/4$ electrons to each bond where Z is the valence of the atom. On the GaAs surface this would yield 3/4 and 5/4 electrons per dangling bond for Ga and As, respectively. However, the big difference in energy between the Ga and As dangling bond states dictates that it is energetically favorable to transfer charge from the Ga-derived surface states to the As-derived ones. The energy of these dangling bonds has been estimated from the energies of s and p atomic levels of Ga and As atoms which form sp^3-hybridized bonding [17]. While the As dangling bond states lie below the valence-band maximum of bulk GaAs, the Ga dangling bond states are well within the conduction band (see Fig. 1.5). This implies that in order to preserve charge neutrality all of the Ga dangling bond states must be empty and all of the As dangling bond states (two electrons) and any AsAs and GaGa dimer bonds (two electrons) on the surface must be filled. This is not possible on an ideal GaAs(001) surface and some dimers must be removed. This compensates for any lack or excess of electrons in the first surface layer by transferring charge from or to the exposed atoms in the second surface layer. The resulting surfaces are said to be autocompensated and their missing dimers give rise to an N-fold periodicity orthogonal to the two-fold periodicity achieved as a result of the first principle. The second principle forms a basis for the electron counting model [18] which is a useful tool to quickly identify possible surface stoichiometries.

The third principle addresses the fact that an experimentally observed surface reconstruction depends on the surface preparation conditions. Each GaAs(001) (and any other semiconductor) surface reconstruction corresponds to a local (but not necessarily the global) minimum in the free energy. These different energy minima often have very small energy differences between them and a slight modification of the preparation method can easily yield a significantly different surface reconstruction. In any case, the resulting surface reconstruction corresponds to the lowest free-energy minimum kinetically accessible under the preparation conditions.

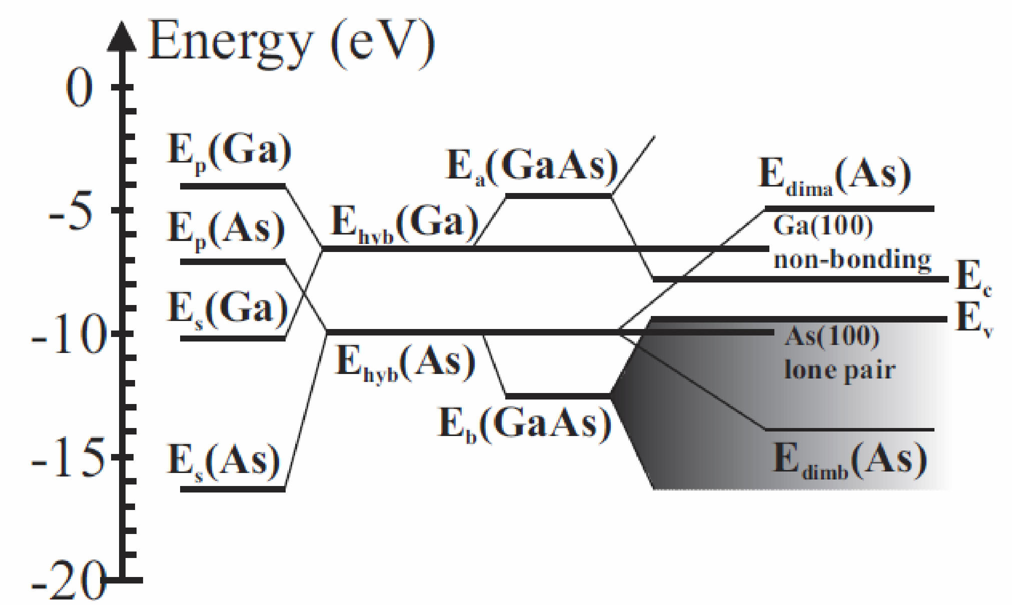

Figure 1.5: GaAs(001) As-terminated surface energy band. From s and p Ga and As states, sp^3-hybridized bonding (E_{hyb}) form bonding (E_a) and antibonding (E_b) states into valence and conduction bands respectively. Dimer formation As-As dimer bonding and antibonding (E_{dimb} and E_{dima}, respectively) with one dangling As bond left at the As sp^3-hybridization energy (As(100)$_{lonepair}$). Since the former is inside the valence band and has to be filled, it results in removal of some As dimers and creation of Ga dangling bonds (Ga(100)$_{lonepair}$) inside the conduction band, with subsequent charge transfer from Ga dangling bonds into the As dangling bonds, achieving autocompensation. Figure is based on figure in reference [17].

A considerable number of reconstructions have been observed for the GaAs(001) surface [19]. Following the conventional two-number notation accepted for specifying a given reconstruction (numbers are the sizes of the unit cell (in units of atomic spacings) in the [110] and [$1\bar{1}0$] direction), these are the reconstructions observed for the GaAs(001) surface in the order of decreasing As content: $c(4\times4)$, $\alpha(2\times4)$, $\beta(2\times4)$, 1×6, 4×6, 4×2 and $c(8\times2)$. Due to the fact that As is more volatile, the As-terminated surfaces are obtained at lower preparation temperatures than Ga-terminated surfaces. With temperature increase more As atoms evaporate leaving a more Ga-rich surface. At too high temperature As is lost to the point that Ga droplets form on the surface.

GaAs(001)-(4×6). The GaAs(001)-(4×6) surface reconstruction is of particular interest since it was used as a starting point for the growth of thin films investigated in this thesis. There are several possible different arrangements of atoms on the surface of GaAs(001) that produce the 4×6 RHEED diffraction pattern. Following Xue et al. [19] they are identified as "Genuine 4×6" (G(4×6)) and "Pseudo 4×6" (P(4×6)) surface reconstructions. Furthermore, for P(4×6) two cases are distinguished: it can be either a mixture of 1×6 and G(4×6) phases (denoted $\mathrm{P}_\alpha(4\times6)$ in this thesis) or a mixture of 1×6 and 4×2 phases (denoted $\mathrm{P}_\beta(4\times6)$). Which particular phase of these Ga-rich surface reconstructions is formed on the surface depends entirely on the surface preparation procedure.

High temperature resulting in evaporation of As or extremely heavy Ga flux can lead to the formation of a regular array of Ga clusters which is a unique signature of G(4×6) surface reconstruction. Each cluster consists of approximately 6 to 8 Ga atoms. Interestingly, charge transfer from these clusters to Ga dimers results in partial filling of Ga dangling bonds which in turn results in higher contrast in filled state Scanning Tunneling Microscopy (STM) images. The contrast enhancement allows a clear view of Ga dimers and serves as a supporting evidence of the bilayer Ga-dimer model proposed by Biegelsen et al. [20].

Both of the P(4×6) surface reconstructions are mixtures of either G(4×6) or 4×2 phases with 1×6. The $\mathrm{P}_\beta(4\times6)$ surface was used in MBE growth of samples studied in this thesis. The phases it consists of, namely, 1×6 (Fig. 1.6) and 4×2 (Fig. 1.7), are shown below. The white and black circles represent As and Ga atoms, respectively; the smaller circles are farther away from the surface. Both phases are characterized by the presence of Ga dimers along the [110] direction. The 1×6 phase also has rows of As dimers running along the [$1\bar{1}0$] direction. The STM analysis shows also that for the 4×2 phase, As atoms in the second layer have filled dangling bonds along $[1\bar{1}0]$ direction (shown in grey in figure 1.6). This is in accordance with the aforementioned second principle for the GaAs surface reconstruction.

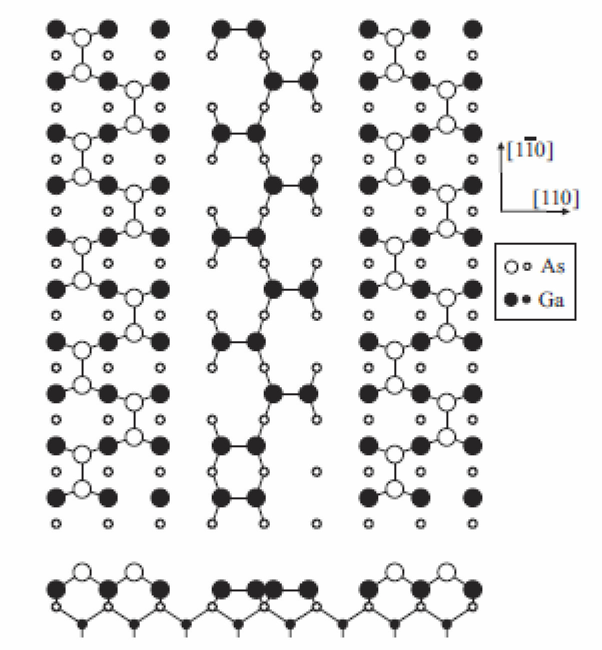

Figure 1.6: GaAs 1×6 surface reconstruction [20]. Top and side views.

Due to the differences in number and arrangement of surface atoms it is not surprising that surface reconstructions have a significant effect on the initial growth morphology of Fe on GaAs(001). First, we consider reports on Fe growth on Ga-rich GaAs(001) surfaces and then on surfaces that are As-rich.

Ga-rich Surfaces. Already in 1986 the growth of Fe on sputtered and annealed Ga(001)-$c(8\times2)$ Ga-rich surface was reported by Chambers et al. [21] in their LEED I-V studies. They found that for deposition thicknesses of up to 3 ML, Fe forms clusters with interstitial inclusions of Ga and As. Above this coverage, the clusters coalesce into continuous Fe film with in-plane lattice constant equal to $a_{GaAs}/2$ and the concentration of Ga and As decreases with the film thickness. The surface segregation of As atoms was also observed.

Bensch et al. [22] reported disappearance of the Reflection High-Energy Electron Diffraction (RHEED) spots of their GaAs(001)-(4×2) substrate after deposition of just 0.5 ML of Fe, but a Fe diffraction pattern did appear after at least 2 ML of Fe were deposited in total. Their magnetic data suggests that FM and magnetic anisotropy (MA) set in at 2.5

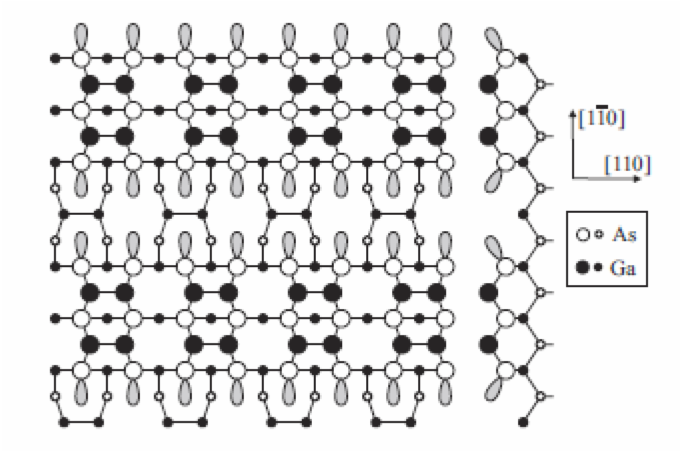

Figure 1.7: GaAs 4×2 surface reconstruction [20]. Top and side views.

ML in the ground state (and at larger thicknesses at higher temperatures). This led them to speculate about island growth at low coverages followed by a coalescence at coverages around 2.5 ML. The same group reported similar growth mode for the GaAs(001)-(2×6) reconstructed surface.

The Fe growth on GaAs(001)-(4×6) reconstructed surface has been reported by numerous groups [23, 24, 25, 26, 27]. Sano et al. [23] reported a rapid decrease in the RHEED intensity during the deposition of the first monolayer of Fe which they attributed to increased surface roughness due to cluster formation. Subsequently the RHEED intensity remained at this low level up to a total Fe thickness of about 4 monolayers where a gradual increase was observed. By 5.5 monolayers the RHEED intensity had regained almost its original strength and from this thickness onwards clear RHEED oscillations appear. This clearly demonstrates the clusters coalesce and then layer-by-layer growth occurs. Similarly, Xu et al. [25] suggest that the Fe islands formed on GaAs(001)-(4×6) coalesce at about 5.0 monolayers in their LEED measurements. Monchesky et al. [27] give detailed analysis of the initial growth regime on sputter annealed GaAs(001)-(4×6). They found that up to 2 ML, RHEED features from the GaAs substrate coexisted with those from the Fe islands. They suggest coalescence between 3 and 4 ML, followed by gradual smoothing and quasi-layer-by-layer growth after 5 ML. This is confirmed by combined RHEED and STM studies reported in [24, 26].

To summarize, on Ga-rich GaAs(001) surfaces the initial Fe growth exhibits nucleation of 3D islands (Volmer-Weber growth) while at higher coverages (starting from several ML onwards) it becomes quasi-layer-by-layer.

As-rich Surfaces. On the As rich $\alpha(2\times4)$ and $c(4\times4)$ reconstructions Kneedler et al. [28, 29] report that the growth of Fe at 175 °C proceeds via nucleation of 2D islands followed by predominantly layer-by-layer growth with growth front of 1 ML. On $\alpha(2\times4)$ Thibado et al. [30] found, even in films as thick as 35 ML, only three Fe layers at the growth front via STM. However, there are reports that at lower substrate temperatures (specifically, RT and 95 °C) 3D type growth on GaAs(001)-(2×4) was observed.

1.2.2 Epitaxial Fe Films on Other Semiconductors

Fe epitaxy has also been reported on a whole range of other III-V as well as II-IV and group IV semiconductors. Compared to GaAs ($a_{GaAs} = 5.645$ Å) these substrates exhibit not only a different lattice parameter, but also a different mix of ionic and covalent bonding (while maintaining tetrahedral atomic coordination). Below is given an overview of Fe epitaxy on (001) faces of these zincblende and diamond structure semiconductors.

Fe/ZnSe(001). ZnSe has the same zincblende crystal structure as GaAs, consists of two atomic species of different valence and electronegativity as does GaAs, and has only a marginally larger lattice constant which results in Fe/ZnSe(001) lattice mismatch of $\nu = 1.14$ %. It is not a surprise, therefore, that Fe films can be grown epitaxially on this semiconductor surface [3]. The ZnSe(001) surface is less reactive than GaAs(001) and chemically stable up to 380 °C. At high temperatures (175 °C) layer-by-layer growth mode was observed [9, 31], while at RT 3D growth mode was reported with islands coalescing at thickness $\approx$7 ML [32]. Irrespective of whether the surface is Zn- or Se-terminated, Se atoms form a $\approx$1 ML thick surface segregation layer [33]. Even though the Fe/ZnSe(001) interface appears to be more stable at higher temperatures, growing at suitably low temperatures yields sharper interfaces.

Fe/Ge(001). While general structural parameters of Ge are similar to GaAs yielding a lattice mismatch to Fe of $\nu = 1.33$ %, it is an elemental semiconductor with only one atomic species and, therefore, allows one to estimate the influence of the chemical difference between atoms in the zincblende structure on the Fe overlayer. The problem, however, arises due to the fact that Ge forms a large number of alloys with Fe. For example, Prinz [31] reports magnetically dead layers for films up to 100 Å in thickness grown at 150 °C even though excellent RHEED patterns were observed during the growth. On the other hand, Fe films grown on S-passivated Ge(001) substrate at 150 °C and 25 °C exhibit ferromagnetism starting at 4 ML onwards [34]. Auger Electron Spectroscopy (AES) revealed that Fe layers were not contaminated with either Ge or S. Angle-Resolved AES (ARAES) showed a bcc structure for these Fe films. While growth at lower than a substrate temperature of 25 °C leads to increasing structural disorder [34], it was shown [35] that growth at such low temperatures also decreases interfacial intermixing to the extent that the S-passivation is no longer required. This enables to fabricate Fe films of reasonable quality on unpassivated Ge(001)-(2×1) at RT. A small amount of Ge intermixed into the Fe layer (6 %) does not influence ferromagnetism which occurs at 4 ML coverage. The magnetic anisotropy of Fe/Ge(001) has been reported to be cubic In-Plane Magnetic Anisotropy (IPMA) with easy axes along [100] and [010] for thicker films and uniaxial IPMA in the ultrathin regime [35].

Fe/AlAs(001). Fe/AlAs(001) is another system with an epitaxial mismatch ($\nu = 1.25$ %) very close to Fe/GaAs(001). Moreover, it is perhaps the most closely related system to Fe/GaAs(001): it not only has the zincblende structure with lattice constant value very close to that of GaAs, but it is also a true III-V semiconductor. Yet so far only Lepine et al. [36] have reported on the Fe/AlAs system. They studied the magnetic properties of a 1.7 nm Fe film on AlAs(001), which turned out to be dominated by a uniaxial IPMA with an easy axis along [110].

A detailed analysis of spin injection and detection in the Fe/$Al_xGa_{1-x}As$/GaAs heterostructures for temperatures from 2 to 295 K was done in [37]. The samples analysed in this work were a complex multilayer system composed of $Al_xGa_{1-x}As$ layers with different doping concentrations (total thickness 625 nm), while the Fe layer was 5 nm thick. While At temperatures below 70 K, spin-polarized electrons injected into quantum well structures form excitons, and the spin polarization in the quantum well depends strongly on the electrical bias conditions. At intermediate temperatures, the spin polarization is determined primarily by the spin-relaxation rate for free electrons in the quantum well. This process is slow relative to the excitonic spin-relaxation rate at lower temperatures and is responsible for a broad maximum in the spin polarization between 100 and 200 K. The spin injection efficiency of the Fe/$Al_xGa_{1-x}As$ Schottky barrier decreases at higher temperatures, although a steady-state spin polarization of at least 6 % is observed at 295 K. While no structural information on the nature of the Fe/$Al_xGa_{1-x}As$ interface was provided, one can speculate that a strong correlation must exist between the spin injection efficiency and the roughness/interdiffusion at the interface.

Fe/InP(001). Comparing to the systems discussed so far, the Fe/InP(001) system is different because Fe film grown on InP(001) experiences in-plane expansion rather than compression (ν = 2.32 %). Zavaliche et al. [38] deposited Fe on P-rich InP(001)-(2×4) at RT as well as at 150 K. Scanning Tunneling Microscopy (STM) revealed that Fe films exhibit a 3D growth morphology with small islands of isotropic shape nucleating at the top of the rows of atoms given by the surface reconstruction. As a result surface roughness is significant in these films. The Low Energy Electron Diffraction (LEED) pattern disappeared at 1ML and did not reappear at higher coverages up to 25 ML (the thickest film studied). It is evident that Fe/InP(001) system shows a significantly higher degree of disorder compared to the Fe/GaAs(001) system. Substrate atom outdiffusion was also found to be different, with only In segregating to the surface during RT growth, while no outdiffusion at all was detected at low temperature of 150 K. Despite the disorder, FM is reported to set in at a coverage of 3.6 ML for RT samples and 2.6 ML for 150 K samples with uniaxial IPMA persisting up to 13-15 ML.

Fe/InAs(001). Xu et al. [25] achieved epitaxial growth of Fe on InAs(001) (ν = 5.37 %) on the In-rich (4×2) surface at 175 °C. The growth morphology is similar to the one observed during Fe growth on Ga rich GaAs(001) surfaces: 3D clusters nucleate in the channels between the In dimer rows and at a critical thickness of 3.5 ML the phase transition from superparamagnetic to ferromagnetic Fe occurs. Reports on outdiffusion of substrate atoms and surface segregation are somewhat contradictory with some authors reporting As [39] and others reporting In [40] atoms to be the predominant atomic species in the surface segregation layer. There were also suggestions that interfacial FeAs compounds are somewhat less As driven comparing to Fe/GaAs(001) system [41]. According to Xu et al. [42] the magnetic anisotropy within the Fe/InAs(001) system is uniaxial with easy axis along $[\bar{1}10]$ up to a thickness of about 10ML and cubic with easy axes along [100] and [010] for larger thicknesses.

Fe/GaSb(001). Out of all semiconductor substrates so far investigated, GaSb(001) has the largest mismatch (ν = 5.95 %) on which epitaxial α-Fe(001) films have been grown without an in-plane rotation. Lepine et al. [36] successively grew Fe at RT on the Sb-rich GaSb(001)-(1×3) surface. Magnetically they detected only cubic IPMA with easy axes parallel to [100] and [010]. The measured films, however, were relatively thick (from 12 ML onwards). It is possible that for thinner coverages uniaxial IPMA exists as suggested by measurements carried out on Fe/InP(001) ($\nu = 2.32$ %) and Fe/InAs(001) ($\nu = 5.37$ %) where the uniaxial IPMA persists only up to about 13-15 ML and 10 ML, respectively.

1.2.3 Thin Films on Metal Substrates

So far we have discussed FM/SC systems. There is also a significant number of experiments on thin films epitaxially grown on metal substrates. Since part of this thesis deals with thin metal layers grown on metal buffers, selected works on metal-on-metal thin films will be briefly reviewed below.

A number of magnetic and structural measurements were performed on different samples (Co, Cd, Fe) grown on Cu substrate. Tischer et. al [43] employed Magnetic X-ray Circular Diochroism (MXCD) in their study of Co/Cu(100) magnetic samples. They observed an increase in both orbital and spin moments compared to the bulk Co. The $1/d$ dependence of orbital moment versus the thickness of the sample was also established in their experiment. They concluded that growth undergoes change from island formation to layer-by-layer growth at 3 ML.

Thomassen et al. [44] investigated the Fe/Cu(100) (lattice mismatch 1 %) system using Magneto-Optic Kerr Effect (MOKE) at $T = 170$ K. They observed perpendicular magnetization up to rather large thickness of 11 ML at which it switched to in-plane orientation. They attributed it to the relaxation of epitaxial strain at this thickness via creation of dislocation in the film. Their results are similar to that of the MXCD study by Dunn et al. [45].

An interesting study of one-dimensional Fe stripes on Cu(111) was done by Shen et al. [46]. An array of long Fe stripes of 1-2 atoms in height and 5-15 atoms in width was produced by step-edge decoration of stepped Cu crystal. MOKE measurements carried out at 100 and 160 K showed perpendicular magnetization, unlike Fe stripes on W(110), where in-plane magnetization was reported [47].

Boeglin et. al [48] described the growth and the interface of Fe/Pd(100) ultrathin films grown at room temperature by several techniques, including core photoemission and Extended X-ray Absorption Fine Structure (EXAFS). A structural transition was reported to occur after 4 ML where a face-centered cubic (fct) $Fe_{55}Pd_{45}$ alloy structure is evidenced with a further deposit of body-centered cubic (bct) Fe layers. Analysis of the magnetic properties obtained by MOKE and MXCD lead to a conclusion that the in-plane anisotropy and the large orbital moment measured on the Fe $L_{2,3}$ edges for the 3 ML Fe/Pd(100) film are related to the interface alloying and fct structure.

A large number of epitaxially grown, both *in situ* and *ex situ*, samples were investigated by Professor B.Heinrich and Professor E.D. Crozier of Simon Fraser University. For example, for Ag(001) substrate Fe, Cr ([49]), and Cu, Ni and Ni/Fe ([50]) thin films were studied utilizing the glancing incidence XAFS technique, discussed in greater detail in the following chapters. Fe/Cu/Fe system [51] and ultrathin InAs films [52] grown on GaAs(001) was also studied using surface XAFS (as well as other techniques).

Briefly, it was shown that Cu on Ag(001) exhibits a bct structure with $c/a = 1.076$ for thicknesses up to 8 ML. Both Fe and Cr also exhibited bct structures with rather large out-of-plane expansions which cannot be accounted for by a small lattice matching in-plane contraction in case of the Fe and a small in-plane expansion in the case of Cr. A larger than bulk disorder was observed in both samples with in-plane component surpassing out-of-plane. In addition, the XAFS technique was tested on a deeply buried interface of a complex multilayered Fe/Cu/Cr/Cu/Fe/Ag(001) sample [49] - since many actual devices consist of a stack of different layers, and the ability to probe buried interfaces becomes an essential part of analysis for precise structural determination. Interestingly enough, unlike Cu, Ni grown on Ag(001) exhibits a fcc-like structure for 9 and 37 ML, while it is bcc-like for low coverages [50]. While exact coordination numbers are smaller than bulk fcc values, they are greater than bcc bulk values. It is suggested that around 9 ML thickness a phase transition from bcc- to fcc-like Ni structure occurs. In the Fe/Cu/Fe system tetragonal distortion of Fe from bcc to bct structure was reported [51] with the in-plane expansion and out-of-plane contraction of 0.8 % and 0.2 %, respectively.

The structural and magnetic properties of ultrathin Mn layers grown on Si(001) were studied in [53]. XAFS analysis revealed that the structure of the silicide layer that forms depends on the growth temperature of the capping layer. A capping layer grown at 200 °C on 0.35 monolayers Mn results in a metastable MnSi phase with a B2-like (CsCl) structure, whereas a cap grown at room temperature on 0.5 ML followed by annealing at 200 °C produces a lower coordinated MnSi phase with a B20-like structure.

A polarization-dependent EXAFS measurements were done to experimentally prove the theoretically predicted contraction of interatomic distances in nanoscale Co islands on Cu(001) [54]. It was shown that 0.3 monolayers Co grown on Cu, Co and Cu atoms are exchanged, forming an alloy to up 20 % of the thickness.

Extensive work on growth of Fe/GaAs(001) was carried out by the two aforementioned groups. However, we reserve discussion of it for later chapters.

Chapter 2

X-Ray Absorption Fine Structure

In this chapter the principles of the XAFS technique will be reviewed. First, a conceptual description of the process will be given.

2.1 Principles of XAFS

2.1.1 X-ray Absorption

X-ray photons are absorbed by atoms when their energy is sufficient enough to free a bound electron in the atom [1]. This energy is commonly referred to in spectroscopy as the absorption edge of the atom. When the electrons are in the most inner ($n = 1$) shell, the absorption edge is called the K-edge. For the next shell ($n = 2$) the edge is known as the L-edge, and so on. For photon energies up to 40 keV this process is dominated by photoelectron absorption when the incident photon is completely absorbed and its energy is transferred to excite a photoelectron leaving behind a core hole. As a result, the intensity of the transmitted radiation is modified with respect to the intensity of the incident radiation and, consequently, the absorption coefficient of the absorbing atomic species can be determined. Such transmission measurements are typical in spectroscopic applications where surface sensitivity is not required. In surface experiments when the photon beam is near parallel to the sample, however, fluorescence and total electron yield signal detection are utilized. The core hole created during photoexcitation is subsequently filled by an electron from the higher shell with emission of a fluorescent photon or a secondary Auger electron. Both of these signals provide the same information as the transmission experiments.

Neglecting for now the possible multi-electron excitations and assuming that all the absorbed photon's energy is used to excite the core electron, the kinetic energy of the photoelectron is given by the difference between the incident photon energy and the electron's binding energy within the atom. Quantum mechanically the photoelectron is treated as a wave with the de Broglie wavelength $\lambda = 2\pi\hbar/p$. The momentum of the photoelectron, p, is determined by

$$p = \sqrt{2m_e(\hbar\omega - E_0)} \tag{2.1}$$

where m_e is the electron mass, $\hbar$ - the reduced Planck's constant, ω - the angular frequency of the x-ray photon with energy $\hbar\omega$, and E_0 is the binding energy of the electron in the atom.

The absorption coefficient, μ, can be described then by Fermi's Golden Rule within the dipole approximation for the photon-induced transition of the electron from its initial core state, $|i\rangle$, with energy E_i into the final photoelectron state, $|f\rangle$, with energy $E_f = E_i + \hbar\omega$ [2]:

$$\mu(E) = \frac{4\pi^2\omega e^2}{c}|\langle f|\overrightarrow{\epsilon}\cdot\overrightarrow{r}|i\rangle|^2\rho(E_f) \tag{2.2}$$

where $\overrightarrow{\epsilon}$ is the polarization unit vector of the electric field, e - electron's electric charge, c - speed of light in vacuum, $\overrightarrow{r}$ - electron's coordinate, and $\rho(E_f)$ is the density of final unoccupied states at the X-ray absorbing atom.

If there are no atoms surrounding the absorbing atom, i.e. a monoatomic gas, the absorption coefficient is a smooth decreasing function of energy above the absorption edge. If, however, the absorbing atom is surrounded by other atoms, as in molecules or in the condensed state, the outgoing photoelectron wave is scattered from these neighbouring atoms (Fig 2.1).

The interference between the backscattered and the outgoing waves at the center of the absorbing atom modifies the electron wave function reducing or enhancing the probability of the x-ray absorption. In other words, the matrix element in equation (2.2) is modulated by this interference and, as a result, an oscillatory fine structure appears above the absorption edge in the absorption coefficient μ. This fine structure is commonly referred as XAFS. The high energy part of XAFS is usually referred to as Extended X-Ray Absorption Fine Structure (EXAFS), while the low energy part (typically below 40 eV) is referred to as X-Ray Absorption Near Edge Structure (XANES) (Fig. 2.2). In the simplest approximation for nearest atomic neighbours (with an effective two-body harmonic potential and absence

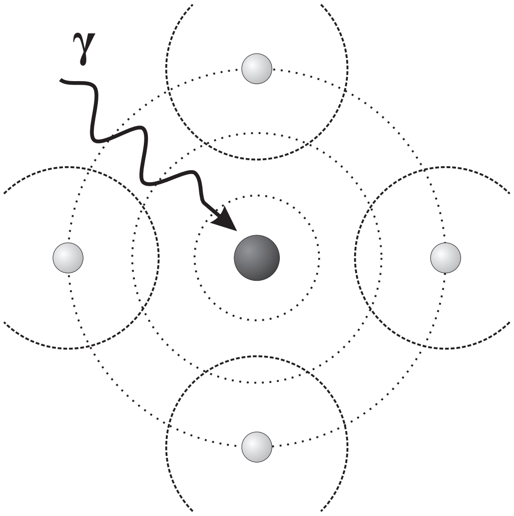

Figure 2.1: The propagation of the spherical photoelectron wave from the central absorbing atom in the cubic lattice. Outgoing (dashed line) and backscattered (heavily dashed line) parts of the wave are shown.

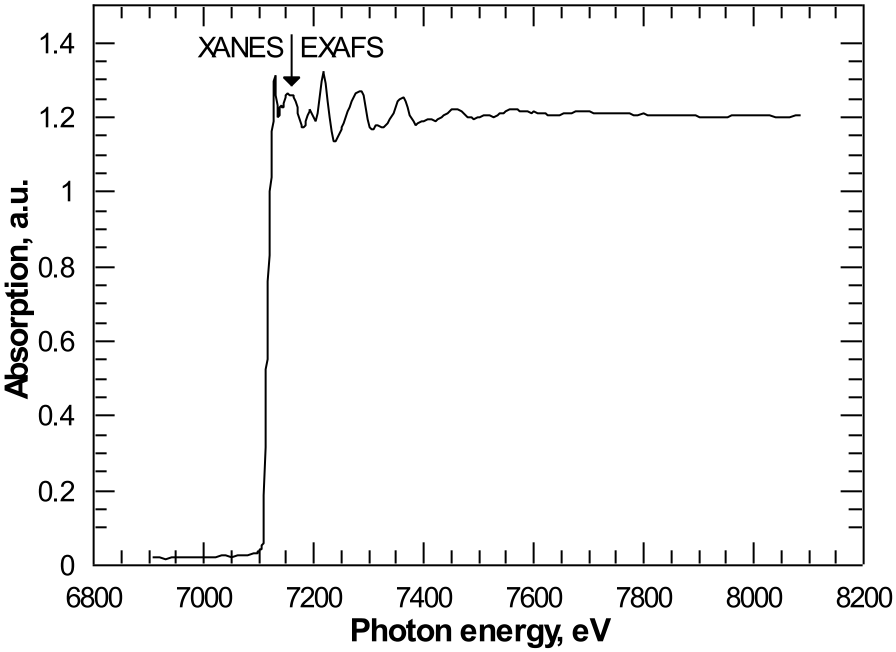

Figure 2.2: Typical XAFS K-edge spectrum of BCC Fe taken in transmission. XANES and EXAFS regions are indicated loosely.

of multiple scattering), the EXAFS is well understood and has been used extensively in many branches of science for decades. However, comprehensive structural analysis that goes beyond this approach to include multiple contributions from different atomic species at the same radial distance, multiple scattering, polarization-dependence etc, can be complex. In this thesis, we will mostly concentrate on the EXAFS part of the spectrum.

The phase of the backscattered wave depends on the internuclear distance between the absorbing and backscattering atoms. The phase is also shifted by the interaction of the photoelectron with the charge densities of the absorbing and backscattering atoms. Plus the amplitude of the backscattered wave depends on the atomic species and coordination of the backscatterer. As a consequence EXAFS contains information about the immediate environment of the absorber. Extracting this information by means of data analysis allows one to learn about structural characteristics of the sample.

2.2 The EXAFS Expression

The EXAFS function, $\chi(E)$, appears as an additional term in the total absorption for the incident photon energies E greater than the absorption edge E_0:

$$\mu(E) = \mu_0(E)(1 + \chi(E)) \tag{2.3}$$

where $\mu_0(E)$ is a slowly varying background that reflects the atomic features. Rearranging, the fine structure is given by

$$\chi(E) = \frac{\mu(E) - \mu_0(E)}{\mu_0(E)} \tag{2.4}$$

In order to relate $\chi(E)$ to structural parameters, it is transformed from energy space into wavevector space using $k = \sqrt{2m_e(E - E_0)}/\hbar$. The common EXAFS expression $\chi(E)$ for a K-edge in the plane-wave single-scattering approximation for a Gaussian distribution of atoms with small structural disorder and an effective two-body harmonic potential is given then by [3, 4, 5, 6, 7]

$$\chi(k) = \sum_i \frac{N_i}{kR_i^2} S_0^2(k) F_i(k) e^{-2R_i/\lambda_i(k)} e^{-2k^2\sigma_i^2} \sin(2kR_i + 2\delta(k) + \phi_i(k)). \tag{2.5}$$

Systems with large disorder, anharmonic potentials and asymmetric distribution functions are discussed in references [8, 9, 10, 11]. In equation (2.5), N_i, is the number of atoms of type i located at an average distance R_i from the absorber. $e^{-2R_i/\lambda_i(k)}$ is a reduction term due to inelastic losses in the scattering process with $\lambda_i(k)$ being the electron mean free path. $e^{-2k^2\sigma_i^2}$ is the EXAFS Debye-Waller reduction factor due to structural and thermal disorder with σ_i^2 being the mean-square relative displacement about the average distance R_i. $S_0^2(k)$ is a slow-varying amplitude reduction factor due to multiple excitation effects, describing the overlap between the wavefunctions of the passive electrons in the absorbing atom before and after the ejection of the core photoelectron [12, 13]. The EXAFS community normally ignores the k-dependence and replaces $S_0^2(k)$ by a constant, S_0^2. It is determined by the calibration with a reference system and typically takes values between 0.6 and 1.2. $F_i(k)$ and $\phi_i(k)$ are the backscattering amplitude and phase shift, respectively, while $2\delta(k)$ accounts for the phase shift associated with the absorbing atom. These functions can be either extracted from a reference compound spectrum, or calculated from first principles. With advances in the theory and the computational power of modern computers the second method is routinely used in analysis. In this thesis, the "FEFF7" [14] software package was used for obtaining backscattering amplitudes and phase shifts.

Equation (2.5) in the given form does not take into account the spherical nature of the photoelectron wave, multiple scattering events and polarization of the incident photon. These factors, however, cannot be ignored in comprehensive EXAFS analysis and need to be incorporated into equation (2.5). This is done by modifying $F_i(k)$ and $\phi_i(k)$ without changing the simple formalism of the EXAFS expression itself.

At large distances from the absorber, the curvature of a spherical wave front lessens and the plane-wave approximation is valid. However, at low energies or short distances between absorber and backscatterers, the curvature is pronounced. It was shown by Rehr [15] that the simple form of equation (2.5) can be retained if the effective backscattering amplitude and phase shift are replaced with $F_i(k, R)$ and $\phi_i(k, R)$, with the effective backscattering amplitude having an overall $1/R$ dependence.

Multiple scattering refers to the scattering in which the outgoing photoelectron wave is scattered by more than one atom. Figure 2.3 shows two of the possibles scattering paths for an arrangement of three atoms with photoelectron wave originating at the absorber A. In both cases, the outgoing photoelectron wave is scattered at atom B, then scattered at atom C. The return paths, however, can be different - in one case it is backscattered to atom B and then returns to the absorber, while in the other it is scattered directly to the absorber.

While single scattering (backscattering) has dominant overall contribution to the EXAFS signal, multiple scattering plays an important role, especially at low energies. Even at higher

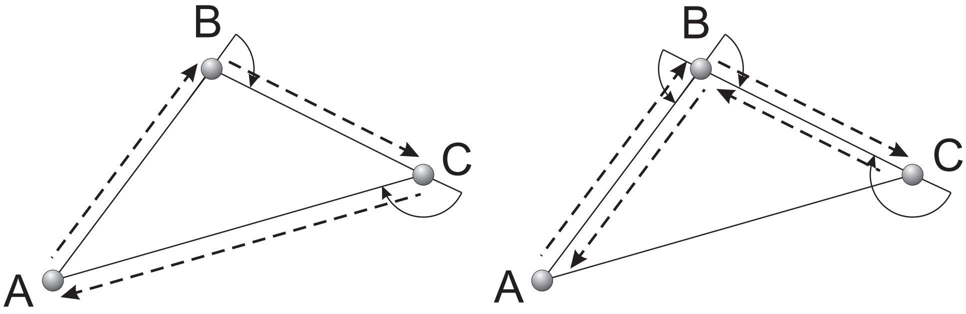

Figure 2.3: Multiple scattering paths.

energies, multiple scattering by atoms along a linear path (shadowing effect) can actually be comparable in the signal amplitude with direct backscattering, because the photoelectron wave is strongly enhanced by the forward-scattering of the intermediate atom. In fact, both amplitude and phase are modified significantly in the range of scattering angles from 0° to ≈ 15° [4]. The significance of multiple scattering and its strong dependence on the model, i.e. the bond angles which are functions of the bond length, is explored in detail in [16].

Formally, backscattering amplitudes and phase shifts for multiple scattering in equation (2.5) are treated like single scattering $F_i(k,R)$ and $\phi_i(k,R)$, again, retaining the original simple expression. The computational problem, however, until relatively recently made it hard to utilize the theories that were in-place to include the multiple scattering effect: the number of multiple scattering paths grows exponentially with the increase of the atomic cluster size. Rehr et al. [15] developed a robust method for calculating any multiple scattering accurately and fast, while eliminating insignificant multiple scattering contributions based on the amplitude rejection. In this thesis, the multiple scattering paths were included in the fitting where it was reasonable.

Polarization of the incident photons plays a crucial role in surface EXAFS. It allows EXAFS to have a directional selectivity due to dipole-like distribution of the outgoing photoelectron wave [15, 17]. Atoms that are located at the direction perpendicular to the x-ray electric field vector contribute very little to the EXAFS spectrum (see Fig. 2.4). Therefore, by using polarization either in-plane or out-of-plane of the sample's surface, it is possible to collect data from atoms located at different positions with respect to the absorber, getting an insight into possible structural anisotropies.

Historically, polarization dependence was treated as a reduction factor for the coordination number N in equation (2.5): $N_{eff} = 3N\cos^2\theta$, where θ is the angle between the

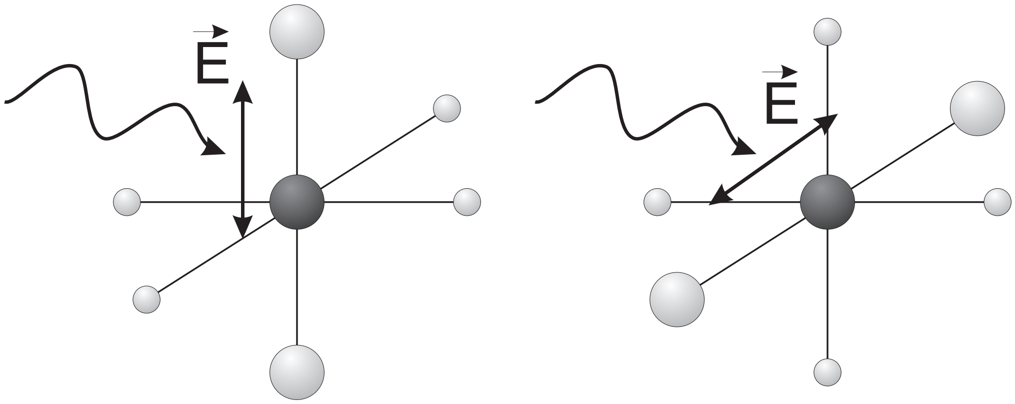

Figure 2.4: Effects of polarization of the incident x-ray, showing different contributions from different atoms.

electric field vector and the directional vector from the absorber to the scatter. While this accounts for the effect of polarization for single scattering paths, for multiple scattering paths this approach is not suitable. The formalism proposed by Rehr et al. [15] allows one to include polarization dependence in the theoretically calculated backscattering amplitudes and phase shifts in a straightforward manner.

In this thesis the curved-wave multiple scattering polarization-dependent approach is used to find the theoretical scattering amplitudes and phase shifts for the least-square-fitting of experimental results.

2.3 Data Analysis

After the absorption spectra (fluorescence and total electron yield in this thesis) have been acquired they are manually inspected for possible Bragg peaks and other artifacts (commonly known as “glitches”). Glitches are removed by fitting a low order polynomial to the region of the spectrum containing such features. The degree of the polynomial is chosen based on visual comparison between the dataset in question and a dataset that was collected under different angle with respect to the incident x-ray beam and, therefore, has the crystal glitch shifted to another energy. After the deglitching process is done, datasets are put on the same energy grid, using the dataset containing the most data points as a reference and then averaged to improve signal-to-noise ratio. Once a satisfying averaged dataset is obtained, it is converted into k-space from the original energy space. At this point, the edge energy,

E_0, is determined as the energy of the first inflection point which corresponds to the first maximum in derivative of the data. It is important to obtain E_0 in a consistent way to preserve the reproducibility of the final result.

In order to obtain the EXAFS interference function $\chi(k)$, the smooth atomic absorption background has to be removed from the spectrum according to the equation (2.4) First, a straight line is fitted to the pre-edge region and the pre-edge background is removed from the data. Following that, the data is normalized on a per atom basis by dividing it by the edge-jump which is proportional to the number of absorbers and the absorption cross-section. The final step is to remove the post-edge background. Several background removal schemes, utilizing different types of combination of polynomials, can be used to achieve this goal [18, 19, 20]. While it is a relatively easy task to remove background at energies far above the absorption edge, the near-edge region poses difficulty due to the sharp increase in the atomic absorption at the edge. A good background removal scheme must ensure that the Fourier Transform (FT) of $\chi(k)$ does not contain unphysical low-R components, except for possible leakage from the first shell.

In this thesis, the AUTOBK [21] software package was chosen since it meets all these requirements. It uses fourth-order basis splines (B-splines) with knots equally spaced in k-space to minimize the leakage of the background into the first shell. The stiffness of the spline is controlled by the number of knots. At each knot, the spline is allowed one degree of freedom. At a knot, the value of two adjacent polynomials and their first two derivatives are required to be continuous. Therefore, it leaves a free variable which can be interpreted in different ways (e.g. the value that the spline must have at the knot, or the discontinuity in the third derivative at the knot). The maximum number of splines is given by the number of independent points in the low-R region. From information theory the number of independent points for $0 \leq R \leq R_{bkg}$ is given by [22]:

$$N_{bkg} = 1 + \frac{\Delta k R_{bkg}}{\pi}, \tag{2.6}$$

where $\Delta k = k_{max} - k_{min}$ is the range of available data.

From a practical point of view, R_{bkg} would typically be half-way between the origin and the first shell radial distance. Fourth-order B-splines ensure that no more than one full oscillation of the spline can occur between knots, so that the highest measurable frequency (the Nyquist critical frequency) that can be removed from the background is R_{bkg}.

Fig. 2.5 shows two data sets (fluorescence and total electron yield) for 24 monolayers of

Fe (out-of-plane polarization) with the X-ray electric vector perpendicular to the surface, with the angle of incidence of the X-ray beam relative to the surface less than the critical angle, φ_C. Fig. 2.6 shows the XAFS interference function $\chi(k)$ obtained using AUTOBK background removal. AUTOBK is able to remove these differences without altering the actual XAFS data, as can be seen from the comparison of the two $\chi(k)$ - they are almost indistinguishable.

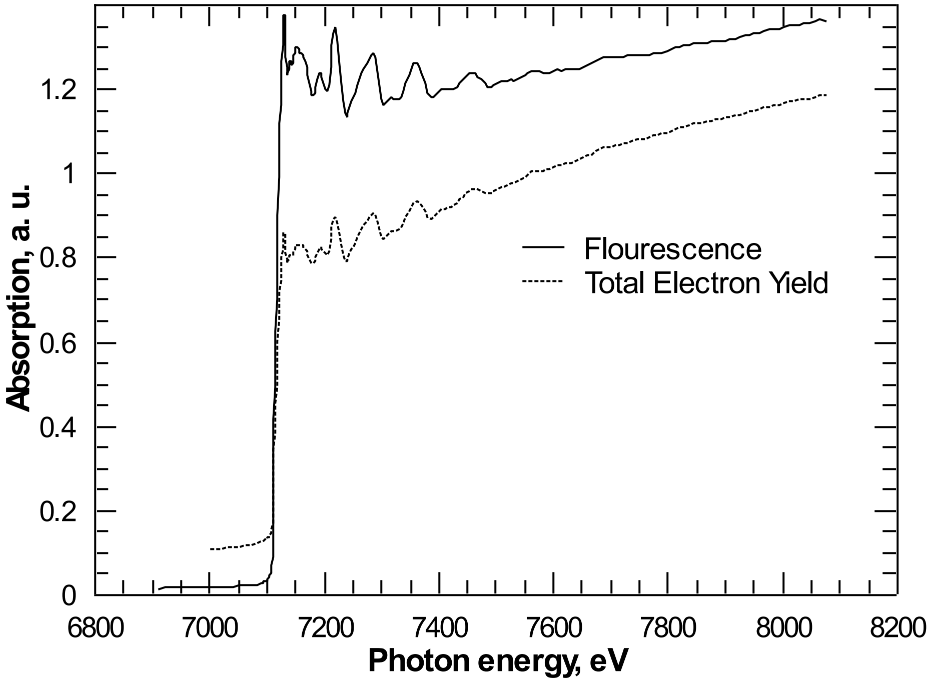

Figure 2.5: Fluorescence and Total Electron Yield data for 24 monolayers of Fe taken with out-of-plane polarization in the total reflection mode.

It is convenient to separate the frequencies contributing to the EXAFS interference function by taking the Fourier Transform of $\chi(k)$. Since $\chi(k)$ cannot be measured over an infinite k-space range, it is necessary to use an apodization window function, $w(k)$, to minimize transform artifacts. The window functions in this thesis were chosen to be the 10 % Gaussian window [22]:

$$w_{Gaussian}(k) = e^{\left(\frac{2(k-k_{mid})}{\Delta k}\right)^2 ln(0.1)}, \tag{2.7}$$

and the 10 % Hanning window

$$w_{Hanning}(k) = 0.1 + 0.9\cos\left(\frac{2\pi(k-k_{mid})}{\Delta k}\right), \tag{2.8}$$

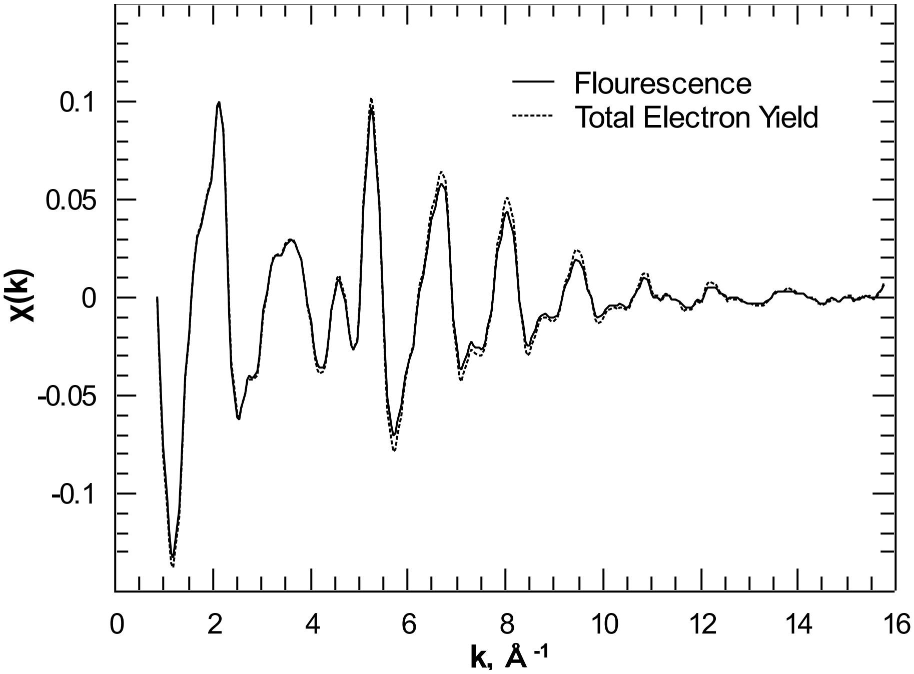

Figure 2.6: $\chi(k)$ for the same two datasets as in Fig. 2.5. Background was removed with AUTOBK using the same setting for each dataset.

where $k_{mid} = (k_{max} - k_{min})/2$ is the middle point of the k-range of the data.

The functional form of the FT is given by

$$FT(k^n\chi(k)) = \frac{1}{2\pi}\int_{k_{min}}^{k_{max}} w(k)k^n\chi(k)e^{2ikR_i}dk, \tag{2.9}$$

where k^n is a k-weighting used to emphasize a particular region of the spectrum.

After the suitable $FT(\chi(k))$ is obtained, the theoretical backscattering amplitudes and phase shifts are used in non-linear least-squares curve fitting. Additional parameters in equation (2.5), such as the electron mean free path $\lambda(k)$ were also obtained theoretically, using FEFF7. There are several software packages specifically designed for the curve fitting of EXAFS data. In this thesis, WinXAS [23] and IFEFFIT [24] packages were used. The variety of distinguishable features in these software packages makes it useful to employ both of them for certain tasks. For example, WinXAS offers a simple graphic interface for fast data analysis, while IFEFFIT allows simultaneous fitting of several datasets which is extremely valuable for setting up correlations between parameters of fits for two different polarizations.

The fitting can be performed both in k-space and in R-space. In this thesis, the second method was mostly used, while the fitting in k-space was utilized as a secondary verification of the goodness of the fit. Both data and the model were transformed into R-space using the same Fourier Transformation parameters, including transformation window, so any transformation artifacts would be present in both the data and the model. The fitting procedure simultaneously fits both real and imaginary parts of FT $[Re(FT(k^n\chi_{data}(k)))$ to $Re(FT(k^n\chi_{model}(k)))$ and $Im(FT(k^n\chi_{data}(k)))$ to $Im(FT(k^n\chi_{model}(k)))]$ while attempting to minimize the residual sum of squares, χ^2:

$$\chi^2 = \frac{n_{free}}{n_{free}-1}\frac{1}{2N_R}\sum_{1}^{N_R}[Re(FT_{data}) - Re(FT_{model})]^2 + [Im(FT_{data}) - Im(FT_{model})]^2, \tag{2.10}$$

where N_R is the number of points available in R-space. n_{free} is the number of independent parameters that can be varied for a given interval in k- and R-spaces:

$$n_{free} = 1 + \frac{2\Delta k\Delta R}{\pi}\frac{\frac{k_{max}}{\Delta k}}{[\frac{k_{max}}{\Delta k}]}, \tag{2.11}$$

where ΔR is the R-space interval used for fitting, and the square brackets in the denominator define the largest integer not exceeding the term in the brackets. The detailed description of data analysis for specific datasets, including determination of the error bars, is described in Chapter 4.

2.4 The Glancing-Incidence Technique

In the glancing incidence geometry, the x-ray photons are incident on a sample at very shallow angles. This significantly reduces the electric field penetration depth, allowing for probing of the sample surface. In this thesis, most of the measurements were performed at angles of incidence below the critical angle of total external reflection, φ_C. A theoretical framework, based on Parratt's original work [25], describing electric field amplitudes in a layered sample in such a geometry was developed by D. Jiang [17, 26] and is reviewed in Appendix A.

In the glancing-incident geometry, the measured absorption coefficient depends on the X-ray incident angle due to the angular dependence of the sample field distribution. The measured fluorescence signal can be expressed as a function of the incident X-ray photon energy with wavelength λ and the glancing-incident angle φ [27]:

$$I_f(\lambda,\varphi) \propto \int_0^\infty \sum_j \eta^j(z)\mu_\rho^j(z)\rho(z) \left\| E^{total}(\lambda,\varphi,z) \right\|^2 dz \tag{2.12}$$

where η is the fluorescence yield (the probability that a core-hole will result in a fluorescence event; for K-shell vacancies it increases with the absorber atomic number Z with $\eta \approx 0.5$ for $Z \approx 30$), μ_ρ is the mass absorption coefficient and ρ is the mass density. In equation (2.12) the summation is over the different absorption edges while the layer index is omitted for clarity. The total electric field amplitude, E^{total}, for layer m is given by

$$E^{total}(\lambda,\varphi,z) = E_m(d_{m-1})e^{-i\frac{\pi}{\lambda}f_m(z-d_{m-1})} + E_m^R(d_m)e^{-i\frac{\pi}{\lambda}f_m(d_m-z)} \tag{2.13}$$

where E_m and E_m^R (see appendix A for derivation) are refracted and reflected beam amplitudes in the m^{th} layer, respectively.

Equation (2.12) for the layered sample for K-edge absorption can be written as follows:

$$I_f(\lambda,\varphi) = \tau I_0(\mu_m^K F_m^K + \sum_{i\neq m}\sum_j \mu_i^j F_i^j + \sum_{non-K} \mu_m^{non-K} F_m^K) \tag{2.14}$$

where m is the m^{th} layer, τ is the ratio of the response functions of the detectors for I_0 and I_f, I_0 is the intensity of the incident X-ray photons, $\mu_i^j = \rho_i \mu_{\rho_i}^j$ is the j^{th} edge linear absorption coefficient of the i^{th} layer at the energy of the incident X-ray photons. The F_i^j factor is given by

$$F_i^j = \frac{\Omega}{4\pi}\eta_i^j \int_{d_{i-1}}^{d_j} \left\| E_i^{total}(\lambda,\varphi,z) \right\|^2 / I_0 dz \tag{2.15}$$

where Ω is the solid angle seen by the detector.

In the equation (2.14) the second and third terms in the brackets constitute the background function: contributions of the layers other than the layer containing the atomic elements of interest and the contribution of all other absorption edges of the sample layer other than the layer containing the K-edge of the atomic element of interest, respectively. This background function is a monotonic function of the X-ray photon energy in the EXAFS region, but has a pronounced peak in the XANES region of the spectrum due to anomalous dispersion in the F_i^j factor.

The fluorescence absorption coefficient as a function of the incident X-ray photon energy E in the glancing-incident geometry is:

$$\mu_{Experimental}^K = \frac{I_f(E)}{\tau I_0(E)} - \mu_{Background}(E) \equiv \mu^K(E)F^K(E) \tag{2.16}$$

where layer index is omitted for clarity and $\mu^{Background}$ denotes the aforementioned background function contribution. Since the energy of the fluorescent photon is constant, the only energy dependence of τ is that of the detector registering I_0. For transmission ionization chambers, this effect is relatively small and can be removed.

Both the left and right hand sides of the equation (2.16) can be rewritten by decoupling each term into two components: a smooth monotonic background (atomic absorption) and an oscillatory portion (XAFS). Below is the new form where a straight line denotes monotonic function and a wavy line - the oscillatory portion:

$$\overline{\mu}^K_{Experimental}(E) + \widetilde{\mu}_{Experimental}(E) = (\overline{\mu}^K(E) + \widetilde{\mu}(E))(\overline{F}^K(E) + \widetilde{F}(E)) \tag{2.17}$$

After normalization to the edge jump and ignoring higher order oscillatory terms we get the XAFS function:

$$\chi_{Experimental}(E) \equiv \frac{\widetilde{\mu}_{Experimental}(E)}{\overline{\mu}^K_{Experimental}(E_0)} = \frac{\overline{F}^K(E)\widetilde{\mu}(E) + \overline{\mu}^K(E)\widetilde{F}(E)}{\overline{\mu}^K(E_0)\overline{F}^K(E_0)} \tag{2.18}$$

After rearranging:

$$\chi_{Experimental}(E) = \frac{\overline{\mu}^K(E)\overline{F}^K(E)}{\overline{\mu}^K(E_0)\overline{F}^K(E_0)}(\chi(E) + \frac{\widetilde{F}(E)}{\overline{F}^K(E)}) \tag{2.19}$$

where E_0 is the edge energy and $\chi(E)$ is the theoretical XAFS function given by equation (2.5).

The $\frac{\overline{\mu}^K(E)}{\overline{\mu}^K(E_0)}$ factor is a smooth monotonic function of energy which is not unique to glancing-incident geometry and also appears in transmission data. It can be cancelled out by using either a reference compound or tabulated values of atomic absorption coefficient as a function of energy.

The other scaling factor, $\frac{\overline{F}^K(E)}{\overline{F}^K(E_0)}$, is not necessarily a monotonic function and its energy dependence is mostly influenced by the angle of incidence, φ, and weakly by the thickness of the sample layer. As the angle of incidence decreases below the critical angle φ_C this factor becomes a linear function with a positive slope to a very good approximation. Moreover, the slope becomes smaller together with the angle of incidence. Consequently, to reduce this factor as much as possible it is desirable to go to angles below φ_C. In this thesis, the angle of incidence was chosen to be $\approx 2/3\varphi_C$.

Close to the absorption edge, up to about 20 eV above the E_0, the F_i^j factor does not exhibit monotonic functional behaviour with respect to energy. Due to anomalous dispersion it has a pronounced peak in the background function. The contribution to the peak comes from the layered structure of the sample due to the electric field distribution in the layers that are not sampled (do not contain the targeted edge of the X-ray absorbing atomic species) reactively responding to the resonance occurring in f' and f'' of the sampled layer absorber near the absorption edge. To minimize this effect it is necessary to filter out the contribution from non-sampled layers. This is done by installing appropriate transmission filters (such as aluminium foil) in front of a fluorescence ionization chamber. Ideally, the filter needs to block fluorescence from the non-sampled layers and allow the fluorescence from the sampled layer to pass to the detector. Alternatively, a detector with an energy discrimination (such as a Ge solid state detector) can be used.

In films where the angle of incidence is greater than φ_C it is customary in extracting the interference function, $\chi(k)$, from the data to subtract the background from the measured $\mu(E)$, normalize to a per atom basis by dividing by the jump in the absorption coefficient at the edge energy, E_0, and replace the background $\mu_0(E)$ by the McMaster values scaled by the $\mu_0(E_0)$ [17]:

$$\chi_{Experimental}(E) = (\mu(E) - \mu_0(E)) \frac{1}{edge\,jump} \left(\frac{\mu_0(E_0)}{\mu_0(E)} \right)_{McMaster} \tag{2.20}$$

The corrections for anomalous dispersion effects can be complex and unreliable. The formalism developed by Jiang and Crozier shows that for ultrathin films measured at angles less than φ_C fortuitously the anomalous dispersion effects are almost cancelled by the McMaster correction. $\chi(k)$ then can be obtained without applying the McMaster correction:

$$\chi_{Experimental}(E) = (\mu(E) - \mu_0(E)) \frac{1}{edge\,jump} \tag{2.21}$$

Chapter 3

Experimental Techniques

The experiment was performed *in-situ* at the Sector 20 Insertion Device (20-ID) of the Pacific Northwest Consortium Collaboration Access Team (PNC-CAT) at the Advanced Photon Source (APS) Synchrotron Radiation (SR) facility using the custom-built Molecular Beam Epitaxy One (MBE-1) system. The benefit of studying surfaces, films and interfaces *in-situ* is that one can study fresh, clean surfaces, surface dosing, low coverage films, films without influence of capping layer and the formation of interfaces between films or film and substrate. The high brilliance X-ray delivered by the undulator allows one to achieve a high signal-to-noise ratio even for sub-monolayer thick films. In the MBE-1 system both sample growth and the XAFS measurements on samples are done within one experimental chamber - the main chamber. Below is given an overview of the system, sample preparation and data acquisition.

3.1 Overview

3.1.1 Molecular Beam Epitaxy

The MBE-1 system was developed to perform *in-situ* X-ray investigations of epitaxially-grown thin films using the techniques of Surface XAFS, X-ray Standing Wave and small angle Reflectivity under Ultra High Vacuum (UHV) conditions [1]. It is primarily intended to be used for deposition of thin metal films on semiconductor or metal substrates. A schematic of the MBE-1 main chamber identifying the ports and their application is shown in Fig. 3.1. The direction of the photon beam is out of the page on the left view and into the page on the right view.

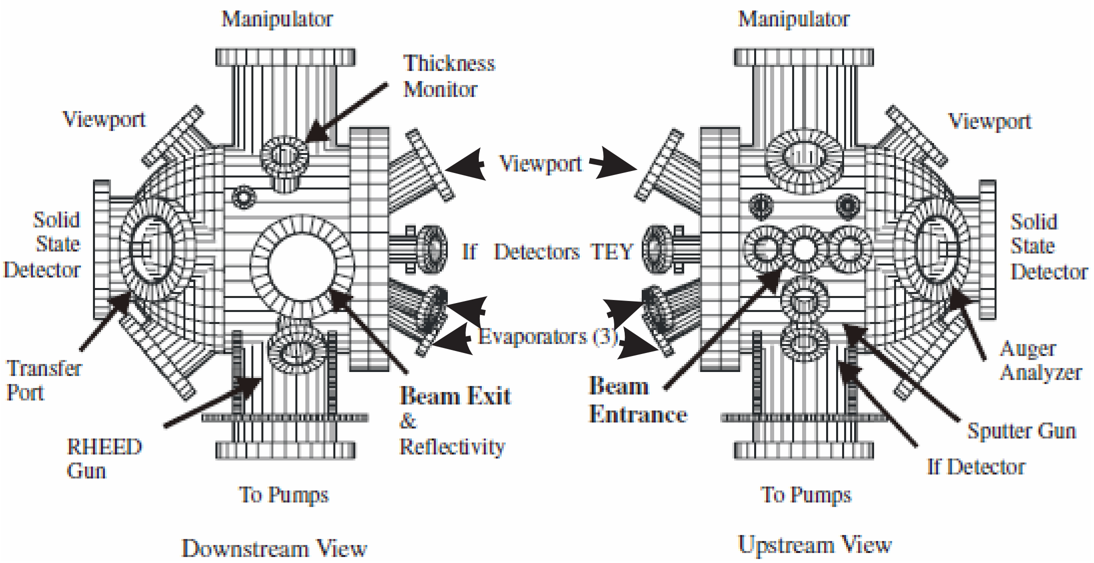

Figure 3.1: Schematic drawing of the MBE-1 chamber identifying ports assigned to major components of the system. Views are as on 20-ID with beam entering from right (upstream) and exiting left (downstream).

One of the main features of the system is its sample positioner. It is a custom-built manipulator based on the GB-16 goniometer from Thermionics Northwest which provides translations along three directions and three rotations: ±180° polar and azimuth and ±80° flip. The minimum stepping sizes are as follows: for the translations 0.635 mm; for polar angle 0.25°, for azimuth angle 0.1762° and for flip angle 0.2083°. While order of rotation should be observed to avoid damaging the manipulator's electrical wiring, such manoeuvrability allows one to easily bring a sample into any desired position using computer-controlled motors. The temperature of the sample holder can be controlled with indirect cooling via a copper braid down to -100 °C and continuous heating to 800 °C with possibility of flash heating up to 1200 °C. While an internal thermocouple provides reading of the manipulator temperature itself, an external one can be brought in direct contact with the sample surface to give precise temperature of the sample. Docking a sample (mounted on a sample holder) with the manipulator is done using a load arm that permits transferring samples in and out of the main chamber. Outside the main chamber the samples are loaded into a load-lock and can be stored on a carousel, up to four samples at a time. This allows for fast sample interchanging during the experiment: several samples can be grown in a row and stored in

UHV conditions on the carousel for later XAFS study.

The MBE-1 main chamber vacuum system features three pumps: a scrollpump-backed turbopump (360 L/s), an ion pump (240 L/s) and a titanium sublimation pump. The base operating pressure in the system is better than 2×10^{-10} Torr after bakeout and pressures less than 5×10^{-11} Torr have been reached. Small gate valves separate the main chamber from the carousel and carousel from the load-lock entry system. The carousel has an ion pump (30 L/s) and is evacuated with a scroll-pump-backed load-lock turbopump (250 L/s), to a pressure better than 5×10^{-10} Torr. Several pressure gauges are installed to monitor the main chamber pressure. A mass-spectrometer at the bottom of the main chamber provides information about gases present in the main chamber giving an idea about possible contamination.

The system is equipped with three Omicron EFM-3 electron beam evaporators designed for thin film growth and molecular beam epitaxy. These evaporators can produce sub-monolayer and multilayer systems operating at evaporation rates from 0.1 monolayer per minute to over 1000 monolayers per second. Water-cooling of evaporators ensures low background pressure (typically in the 10^{-10} Torr range) during evaporation allowing the growth of ultra-pure films. The well-defined evaporant beam allows an uniform deposition on the sample over an area approximately 1 cm^2. During evaporation a part of the evaporant beam is ionised and when these ions hit the substrate, they may create defects in the substrate surface and deposit energy. To avoid this the EFM-3 are equipped with an ion suppressor which repels the ions back into the evaporator.

In this thesis, the substrate state prior to and during epitaxial growth was monitored by Reflection High Energy Electron Diffraction (RHEED). For that purpose the MBE-1 system has a Kimball Physics EMG-14 RHEED gun installed. On the diameterly opposite side of the main chamber, a Charge-Coupled Device (CCD) camera is fitted onto the viewport and the image monitored on a computer screen using custom image analyzing software. For non-epitaxial growth, a crystal thickness monitor (Leybold-Inficon XTM/2) is also available. However, due to the collimated nature of the material flux from the EFM-3 evaporators, one must calibrate the flux using the thickness monitor in place of the sample and then deposit the film.

An Ar^+ sputter gun (PHI 04-161) is used for sample surface sputtering. During sputtering the main chamber is back-filled with ultra-pure argon gas, further purified using a NuPure getter system. The gun produces a beam of energetic inert gas ions for sputter etching solid surfaces. Ions are created within the ionization chamber by accelerating electrons from a hot tungsten filament into the anode region using a bias of 180 V. The ions are drawn out through the open end of the gun chamber and focused by a lens system at the sample surface. The energy of ions incident on the sample surface is equal to positive potential applied to the anode (the sample is grounded). The removal of contaminants from the surface of the sample is verified by Auger spectroscopy using a single-pass analyzer (TFA-200, RBD Enterprises).

The surface XAFS data is collected simultaneously using two custom fluorescence ionization chambers and a Total Electron Yield (TEY) detector, or a solid state detector (Princeton Gamma Technologies 13-element Ge detector). The Be windows of different thicknesses are used for passage of photons into the main chamber as well as out of it. The entrance window and fluorescence ionization chamber windows have a thickness of 125 μm while for the 13-element solid state detector its window is 250 μm. A large (95 mm diameter, 375 μm thickness) Be exit window allows reflectance to be measured with another custom-built wide angle transmission ionization chamber. The working gas in fluorescence ionization chambers is argon and helium in transmission ionization chambers.

The entire system is assembled on a custom table with vertical and horizontal travel and tilt capability for manually positioning in the X-ray beam with or without a toroidal mirror in use.

3.2 Sample Preparation

For all of the samples in this thesis the substrates were epiready n-type GaAs(001) single crystal wafers (American Xtal Technology). The substrates were cleaved and mounted on sample holders in a clean room. Cleaving of GaAs is done relatively easily along (110) and $(1\bar{1}0)$ crystallographic axes by scribing the back of the wafer along the desired edge of the future substrate with a sharp instrument, and then applying gentle pressure in this place until the wafer breaks. If done correctly, the wafer breaks forming a stripe. These stripes were further cleaved to obtain a rectangular substrate of a desired size: approximately 1 cm×1.5 cm. This substrate was then mounted on a thin molybdenum disk located on the front surface of a hollow cylindrical sample holder using two metal clips that firmly hold the substrate in place. In the later design, the clips were replaced with a single tungsten wire to hold the sample to avoid incurring stress on and bending of the substrate. The molybdenum is used to ensure an uniform heating of the substrate during substrate preparation. The back side of the sample holder is used to mount it on the manipulator inside the main experimental chamber. Usually, several substrates were cleaved and mounted on sample holders to be stored in the carousel of the MBE-1 system.

After the main chamber underwent a bakeout for several days at temperatures ≈ 125 °C (depending on the specific component of the MBE-1 and its backout specifications.) and had cooled down to the room temperature (RT), the substrates were then transferred into the experimental hutch where the MBE-1 system is located. There, they were one by one loaded into the load-lock and transferred using the load arm onto the carousel. After de-pressurizing the carousel to a pressure less than 3×10^{-9} Torr, the gate valve into the main chamber was opened and one of the substrates on its holder was mounted onto the manipulator. While being a straight forward procedure of aligning and docking the sample holder with the manipulator, it requires certain practice - the load arm is about two meters long and has to align with the manipulator within millimeters. After that, the substrate was given a 1 hour thermal desorption at approximately 600 °C.

Once a substrate cooled down to RT, it was sputtered with 500 eV Ar^{+} at an angle of 75° with respect to the surface normal for 3 hours at an argon pressure of 2×10^{-5} Torr and at room temperature. This was done to remove oxide formed during etching of surface contaminants by the manufacturer. During the sputtering the substrates were continuously rotated about their normal as this proved to help the achievement of a better 4×6 reconstruction later on [2, 3]. For a number of substrates the absence of surface contamination was verified by visually inspecting Auger spectroscopy scans.

A substrate was then gradually annealed while its surface was monitored by RHEED until the Ga-terminated 4×6 surface reconstruction was achieved (see figures 3.2 and 3.2). The image was formed on a scintillator viewport coating, captured by a CCD camera and viewed in a live mode. The RHEED gun utilizes a 10 keV electron beam which is directed at the sample surface at small incident angles ranging from 0° to 5°. Electrons scattered through a small angle probe 1-2 top atomic layers of the substrate, and as a consequence RHEED patterns are sensitive to the structural changes at the surface. Considering elastic scattering of the high energy electrons from the surface atoms, in a kinematic approximation RHEED patterns can be viewed as diffraction from a two-dimensional atomic sheet. Fig. 3.4 shows the Ewald sphere construction for such a diffraction picture [4].

After substrates cooled down to RT, deposition of the iron films began (the deposition of

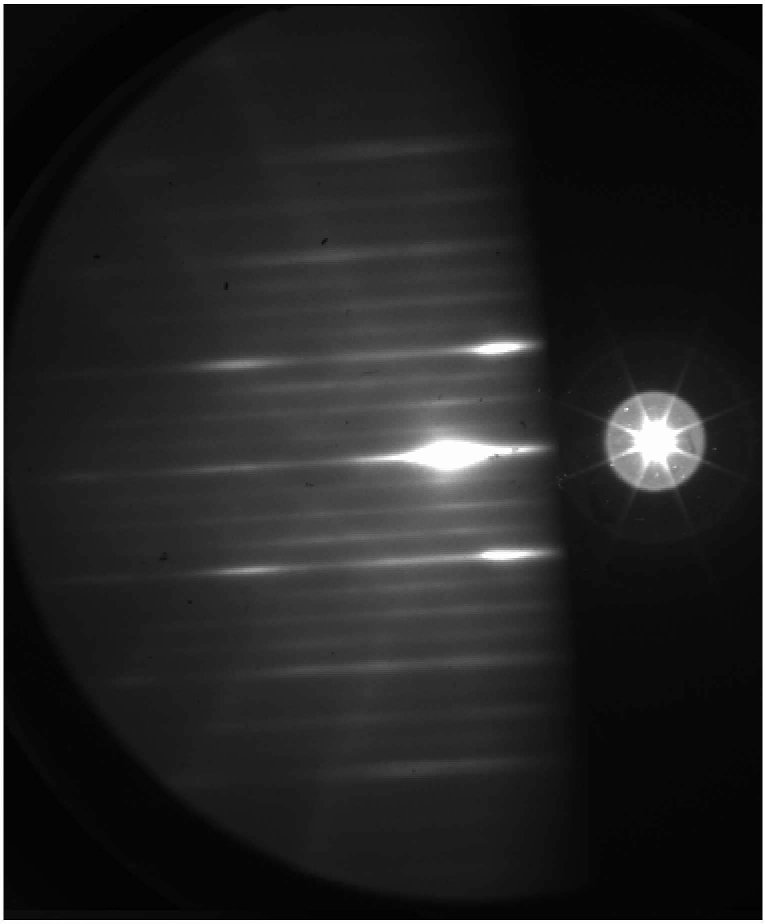

Figure 3.2: Ga-terminated ×4 surface reconstruction RHEED pattern.

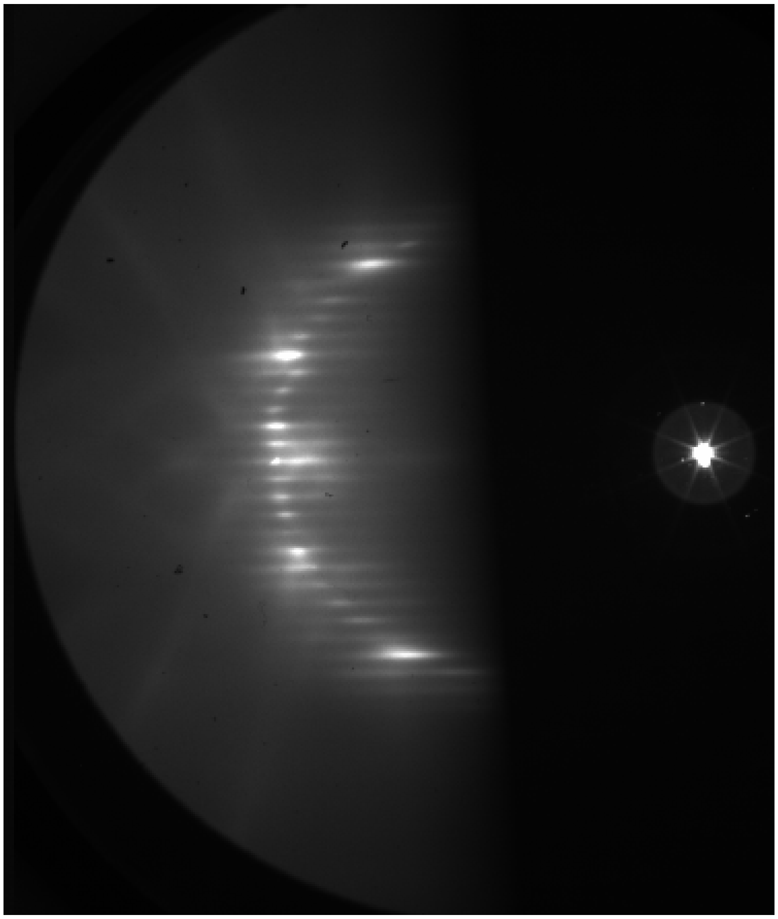

Figure 3.3: Ga-terminated ×6 surface reconstruction RHEED pattern.

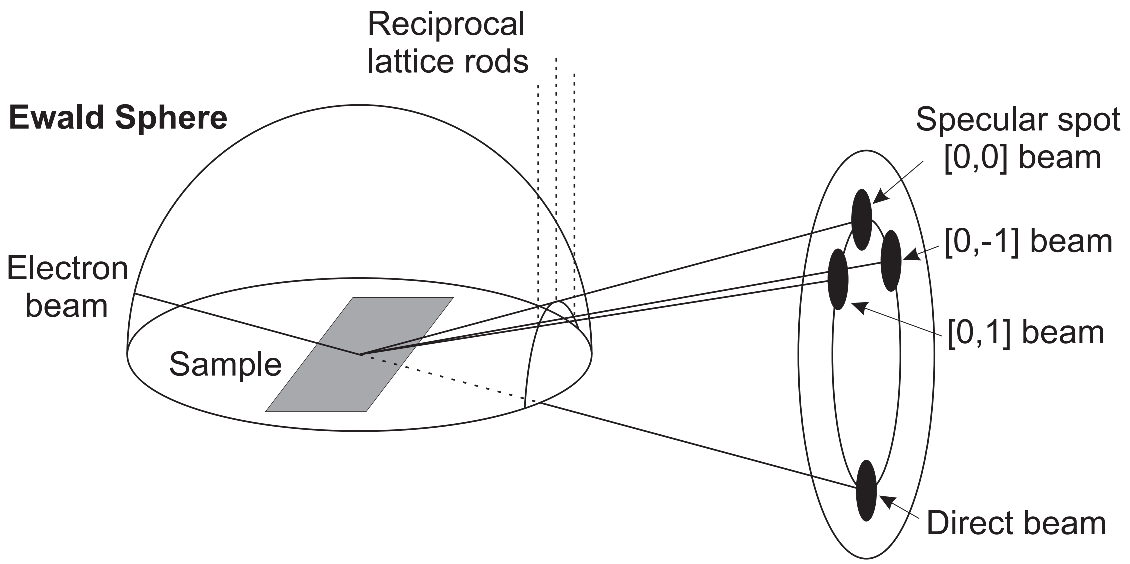

Figure 3.4: Ewald sphere for two-dimensional diffraction.

palladium layers is similar in all aspects, except for the thicknesses). For evaporation pure (99.99 %) metal rods/wires placed into evaporator crucibles were used (Fe, Pd and Au). The deposition rates were the order of 0.5-1 monolayer per minute with $I^{Fe}_{emission} \approx 60$ nA, $I^{Fe}_{flux} \approx 30$ nA and $I^{Pd}_{emission} \approx 20$ nA, $I^{Pd}_{flux} \approx 25$ nA. The evaporator operational voltage was 800 V. The sources were heated until a stable previously calibrated atomic flux was established. Atoms forming the atomic beam from the evaporator moving on a ballistic trajectory were deposited onto the substrate. Once again, RHEED was used to determine the number of deposited monolayers. The image captured by the CCD camera was analyzed for fluctuations in intensity of the specular electron beam in the anti-Bragg configuration (see Fig. 3.5). These fluctuations arise from the evolution of the atomic step distribution on the sample surface. During the epitaxial growth on an ideal surface, the deposited atoms nucleate into islands on the sample surface. These islands grow and eventually coalesce to form a new surface before the nucleation of the next layer begins. This is layer by layer growth mode or so-called Frank-van der Merwe growth [5, 6, 3]. Because RHEED is sensitive to step distribution such growth will produce a diffraction pattern that will have oscillating intensity between flat and stepped surfaces. This enables very accurate determination of deposited film thickness. It is important to mention that before deposition of Pd films on top of Fe films, the former were sputtered for 1 hour and annealed for approximately another hour until a clean specular spot can be observed again. This was done to remove sub-monolayers of As that are known to float on top of iron during Fe deposition [7].

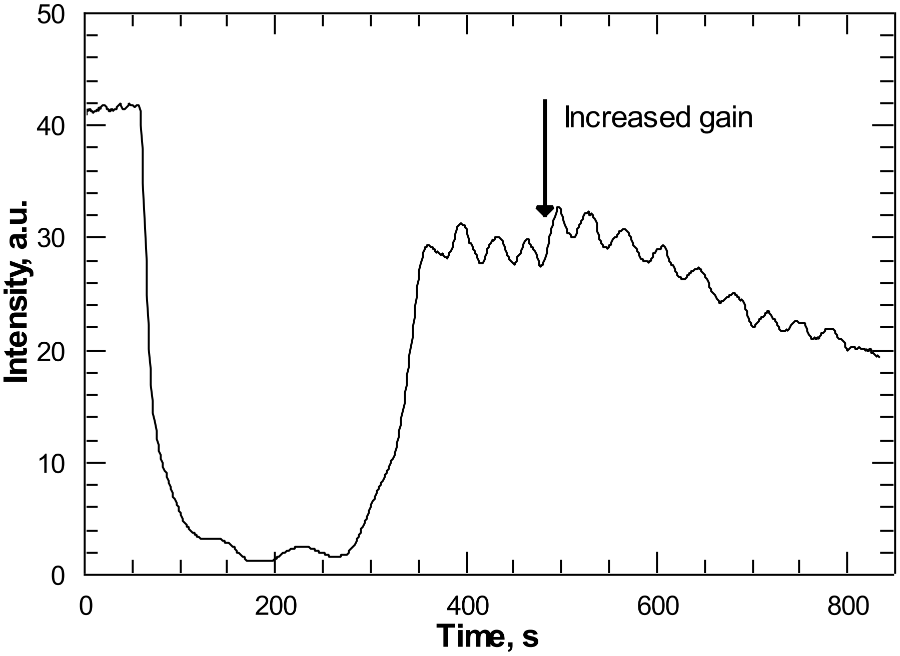

Figure 3.5: RHEED specular intensity oscillation corresponding to 17 monolayers of Fe deposited on GaAs substrate. Notice, the gain was manually increased around 480 seconds.

In the end, several samples were prepared with final thicknesses: 1 ML Pd / 9 ML Fe / GaAs(001), 1 ML Pd / 26 ML Fe / GaAs(001), Au / 10 ML Fe / 7 ML Pd / 38.5 ML Fe / GaAs(001). The layer thicknesses are defined to within an error of ±0.05-0.06 monolayers. However, the XAFS measurements were taken in the intermediate stages of the growth. The sample identification is left until later when the data analysis is discussed.

3.3 Synchrotron Radiation

When charged particles undergo acceleration they produce electromagnetic (EM) radiation. This radiation is called Synchrotron Radiation (SR) when such particles are accelerated radially - acceleration is perpendicular to the particles velocity [8]. While for non-relativistic particles the SR spatial distribution is similar to a dipole radiation, for particles travelling near the speed of light the emission pattern is sharply collimated along the velocity vector of the particles tangential to their trajectory (see Fig. 3.6). The half-angle of the radiation in the laboratory frame is $\Delta\theta \approx \frac{1}{\gamma} = \frac{1}{\sqrt{1-\frac{v^2}{c^2}}}$, where v is the speed of electrons in the storage ring.

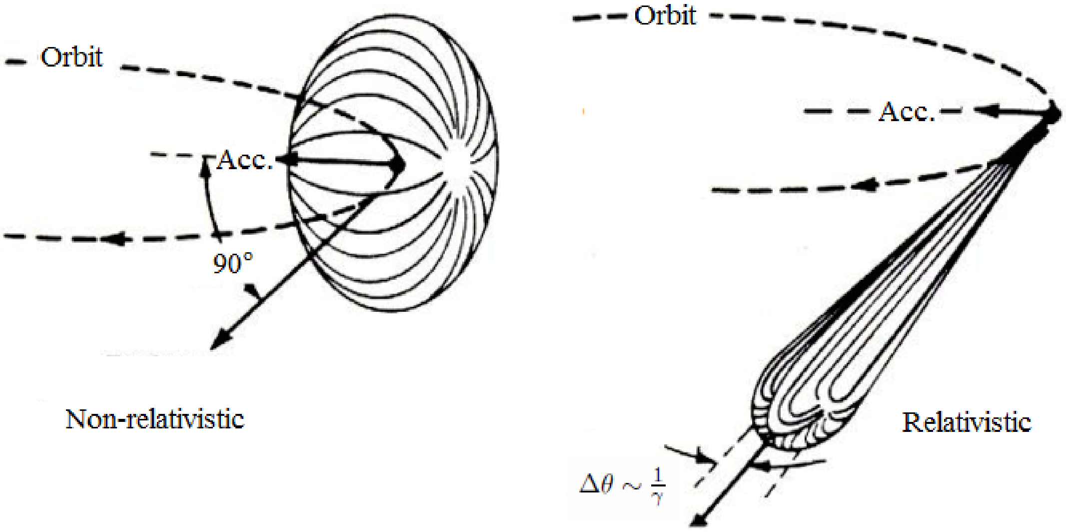

Figure 3.6: Synchrotron Radiation patterns for a non-relativistic and a relativistic charged particle moving in a circular motion [9].

While in synchrotrons the relativistic charged particles (usually, electrons or positrons) move generally in circular orbit of a large radius, in the working region the trajectory is curved using special devices such as bending magnets, wigglers or undulators to achieve higher acceleration of the particles.

In this thesis, SR was generated by undulator A which has 144 pairs of magnets installed in alternating order of polarity (see Fig. A.1) [10]. In the simplest picture the path of electrons travelling in the gap between two magnetic poles is curved due to Loretz force. Due to the presence of the force on the moving electron, it emits radiation. However, the actual picture is much more complicated and is described briefly in the Appendix B of this thesis. The resulting radiation possesses several important features of consequence to the glancing incident surface XAFS:

1. A broad photon energy spectrum providing the ability to excite deep atomic shells in different atomic species.
2. High photon flux providing the ability to perform rapid experiments or use low number of absorbers.

3. High photon beam brilliance providing the ability to illuminate low coverage, small sample regions with high signal.
4. High photon beam stability providing the ability to have constant photon flux during the experiment duration.
5. Linear polarization of the photons providing the ability to utilize natural linear polarizations without need for special equipment.

In addition, although not used in this experiment, the pulsed time structure of the photon beam gives possibilities for time-related experiments on the 100 picosecond time scale.

Figure 3.7 shows a schematic view of the experimental beamline setup downstream from the undulator [11]. The most important component is a fixed exit double crystal silicon monochromator cooled by liquid nitrogen. Si(111) and Si(311) reflective planes can be used to access 4.3-27 keV and 8-50 keV energy ranges, respectively. The Si(311) crystals are mounted besides the Si(111) crystals in the same chamber and interchanged conveniently by displacing the chamber transversely to the beam. The photon flux is of the order of 1×10^{13} photons per second in an unfocused mode with beam size of the order of 1 mm × 3 mm in the B-hutch. The energy resolution is 1.4×10^{-4} with Si(111) crystals at 10 keV. Kirkpatrick-Baez focusing mirrors can be used to focus the beam to 5 μm × 5μm and 1 μm × 1 μm with photon fluxes at 10 keV of 1×10^{12} and 1×10^{11}, respectively. The beam size can be reduced by the slits installed upstream of the experimental hutch as well as slits inside the hutch. Helium filled transmission ionization chambers are installed upstream (Fig. 3.8) from the hutch and within the hutch upstream from the experimental chamber. Since the air absorbs X-ray very effectively, inside the hutch the delivery line filled with Helium along the photon beam path was installed.

3.4 Data Acquisition

The XAFS measurements were carried out at Fe and Pd K-edges at 7.112 keV and 24.350 keV photon energies [12], respectively, using Si(111) crystals. The monochromator was calibrated by setting the energies at which the Fe and Pd K-edges were observed to correspond to tabulated values. The calibration was done on Fe and Pd foils in transmission mode.

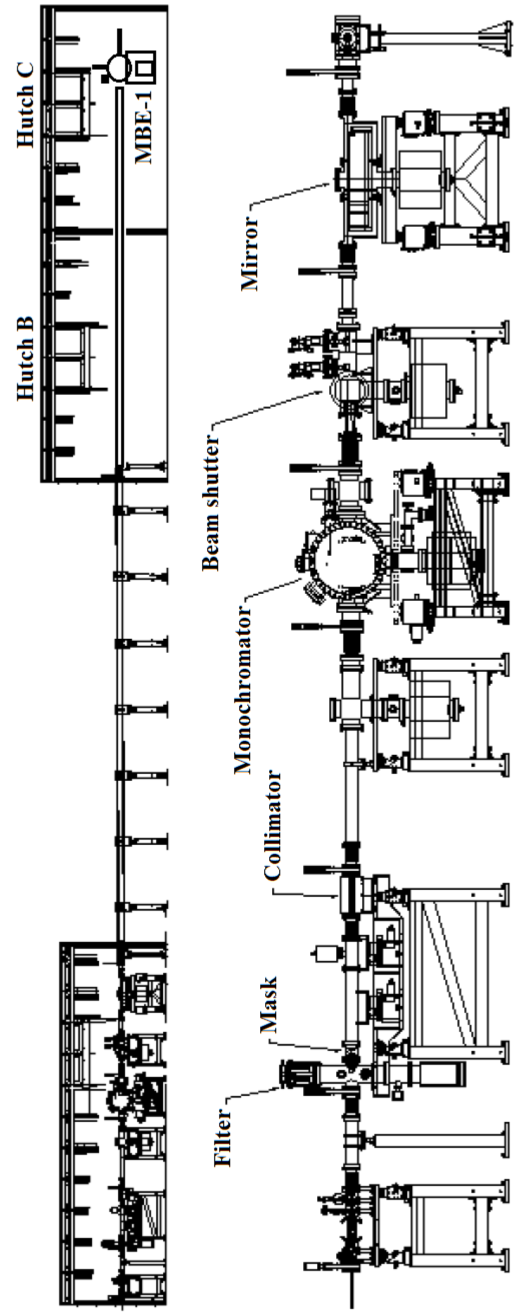

Figure 3.7: Schematic view of the experimental beamline [11]. The lower panel indicates the beam processing components in the First Optical Enclosure (FOE). The X-ray beam travels from the undulator and enters the FOE from the left. In the upper panel, which has a reduced scale, the beam exits the FOE and travels in UHV vacuum to Hutch B. The distance from the centre of undulator A to the entrance to Hutch B is 50.10 m and to the end of Hutch C is 65 m. The MBE system is located at 63.5 m from the undulator.

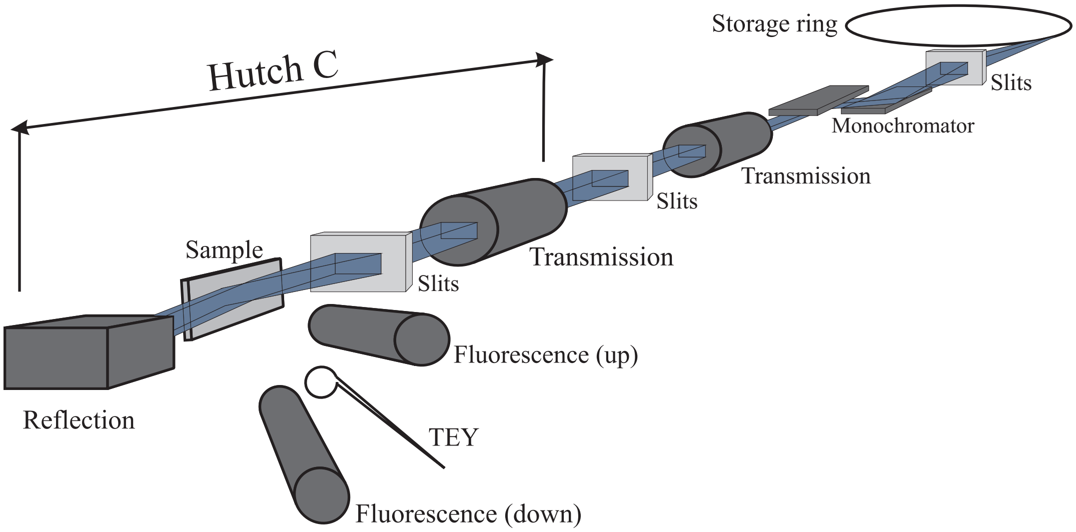

Figure 3.8: Schematic view of glancing-incidence XAFS experiment. The out-of-plane polarization configuration is shown.

Figure 3.8 shows a schematic view of the glancing-incidence XAFS experiment. Since SR produced by the undulator is naturally linearly polarized in the plane of the storage ring, the desired polarization, $E_\perp$ or $E_\parallel$, of the incident electric field vector with respect to the sample surface is achieved by bringing the sample into the photon beam with the sample surface normal either perpendicular or parallel to the storage ring plane, respectively.

Once the approximate position of the sample is established fine tuning of the experiment is performed. First of all, the profile of the photon beam is scanned by manipulating two sets of slits while monitoring the signal from the upstream transmission ionization chamber, and its central, most intense portion is selected. Secondly, the sample is brought into the beam and its position is adjusted in such a way that its surface normal is perpendicular to the direction of photon propagation. This is done by adjusting the sample's polar and azimuthal angles, and transverse and vertical positions with respect to the photon beam, while monitoring intensity of the beam leaving the main chamber either visually using a fluorescence screen and a CCD camera or using signal collected by a wide-angle ionization chamber. In the end, the sample is moved into the photon beam so it blocks half of the beam profile. Next, a reflectivity scan as a function of angle of incidence is performed (see Fig. 3.9). The final angle of incidence is set to $\frac{2}{3}\phi_C$, where $\phi_C = \sqrt{2\delta}$ is the critical angle for the sample as indicated on the plot. This allows one to minimize the effect of anomalous dispersion effects [13, 14] discussed in Chapter 2.

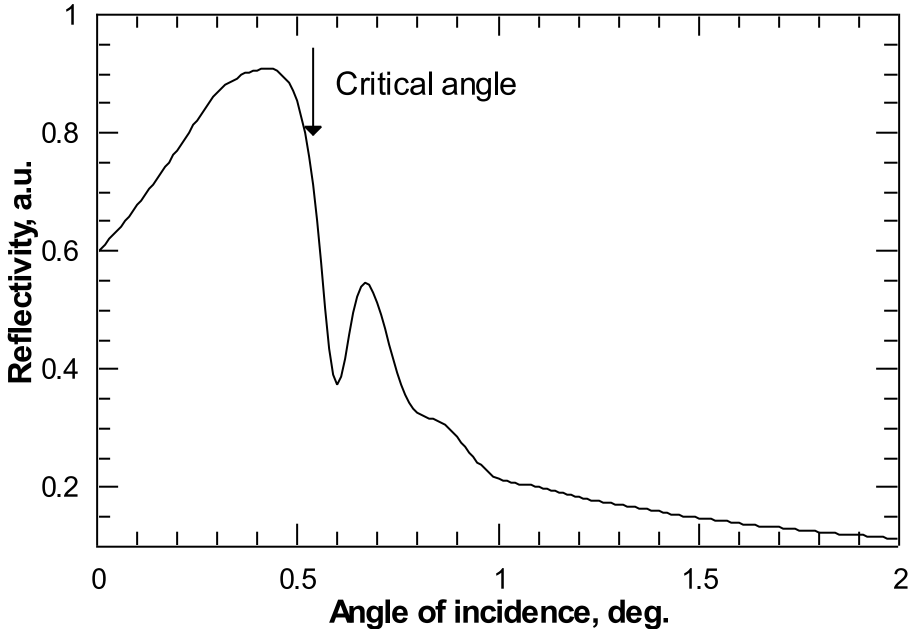

Figure 3.9: A X-ray reflectivity scan showing the determination of the critical angle. The critical angle is located around 2/3 of the maximum reflectivity (≈0.55 degrees). Notice the oscillations past the critical angle are due to the layered structure of the sample. The initial increase in Reflectivity is due to the finite size of the sample.

The data were collected using two argon filled fluorescence ionization chambers and the TEY detector or the 13-element solid state detector for small sample coverages. The fluorescence ionization chambers had aluminium foil filters installed in front of them to reduce effect of anomalous dispersion occurring in multilayered systems [14]. The signal from the detectors was normalized to the signal from the transmission ionization chamber installed in front of the main chamber. This is done to reduce effects of photon beam intensity fluctuations during a XAFS energy scan.

Several quick XAFS scans were done to ensure there is no Bragg peak occurring in the fluorescence spectrum. The Bragg peaks originate from reflection from crystal planes in the sample upon satisfying Bragg's diffraction conditions and the reflected beam entering into the solid angle containing aperture of the fluorescence ionization chamber. Since energy is varying during the scan, one or even several of such peaks can occur in the XAFS region of the spectrum making XAFS data analysis impossible. Figure 3.10 illustrates the problem.

There are several approaches used to eliminate the problem in the described experiment. First, azimuthal rotation (rotation around sample's normal) shifts the energy position of the Bragg peak and it can be moved outside the XAFS energy region. For narrow Bragg peaks consisting of just a few data points it is possible to remove them manually in subsequent data analysis. In this case, a second series of several scans is done at different sample azimuth angles. This shifts the Bragg peak location and exposes the underlying XAFS structure which later is used to eliminate the Bragg peak in the main series of scans. Finally, if the Bragg peak cannot be eliminated from one of the ionization chambers, signal from the second ionization chamber and/or TEY is used to analyse the XAFS data.

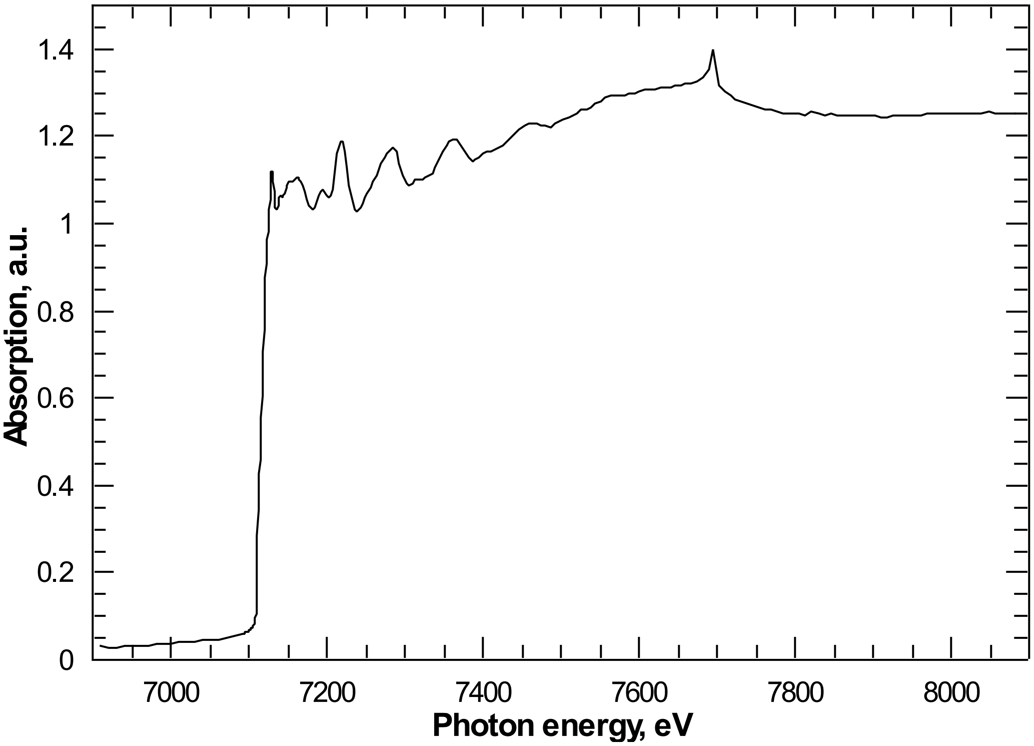

Figure 3.10: A fluorescence scan showing a wide Bragg peak centered around 7700 eV.

Once all of the alignments are done, the data collection begins. The typical scan can be broken into three main regions (see Fig 2.3): pre-edge ([≈-200 eV, -50 eV] with respect to E_0 - absorption edge energy), the absorption edge and XANES regions ([-50 eV, 50 eV] relative to E_0) and XAFS ([50 eV, ≈800 eV] with respect to E_0, depending on the quality of the data). These regions are usually scanned with different monochromator stepping and integration time per point to conserve time. The pre-edge region, being less interesting is done with large steps (10 eV) and small integration time, the XANES region, which may contain transitions to empty states as well as structure originating from multiple scattering pathways in the local three-dimensional arrangement of atoms, is done with small steps (0.3 eV for Fe and 0.75 eV for Pd) and large integration time, and the XAFS region is done with non-linear steps to have equally spaced points in k-space ($\approx$0.75 Å^{-1}) with large integration time since the XAFS signal decays as a function of energy. The number of scans is determined by inspection of the average data and crude XAFS analysis is performed during the data acquisition. Mostly, the number of scans influences the maximum k-range of meaningful data available for later analysis. Here, the trade-off is made between time spent on collecting data for one sample and maximum k-range.

Chapter 4

Data Analysis

In this chapter, the detailed flow of data analysis is given with specific examples using actual data. First, preliminary data processing is discussed, followed by the background removal scheme and Fourier Transform analysis. The models used in the theoretical calculations used in the fitting and the fitting itself are discussed at the end.

4.1 Preliminary Analysis

All of the collected datasets were inspected visually. Usually, already during the data acquisition it was decided signal from which detector will be used in the data analysis: one of the fluorescence ionization chambers or the TEY. It was enforced using the sample's azimuthal angle adjustments that the data from this selected detector did not contain any wide Bragg peaks or glitches that could potentially shadow the XAFS features. Data from the remaining two detectors were used in the early stages of analysis as visual reference for the Bragg peaks and glitch positions.

Any apparent glitches and Bragg peaks were removed by fitting a low-degree polynomial to the dataset region containing these features. This was done with the help of the WinXAS software package [1]. The degree of the polynomial was chosen for each glitch individually depending on the location of the glitch with respect to the apparent XAFS features. For glitches located on top of pronounced XAFS feature, the degree, usually, was higher in order to get a good localized fit to the XAFS. Typically, the degree of polynomial was ranging from 2 and up to 5. The fit was done to all the points in the selected region, excluding specified data points representing the glitch. During the data acquisition it was ensured that no glitch was wide enough to hide an XAFS feature in all the data channels (two fluorescence and the TEY). Typically, the glitches were not wider than 3-4 data points. Figure 4.1 shows the original dataset and the deglitched dataset for 16 monolayer thick Fe sample K-edge in $E_{||}$ mode. Two glitches, each 3 data points wide, were removed using 3rd degree polynomials. Figure 4.2 illustrates the process in more detail for the two indicated glitches.

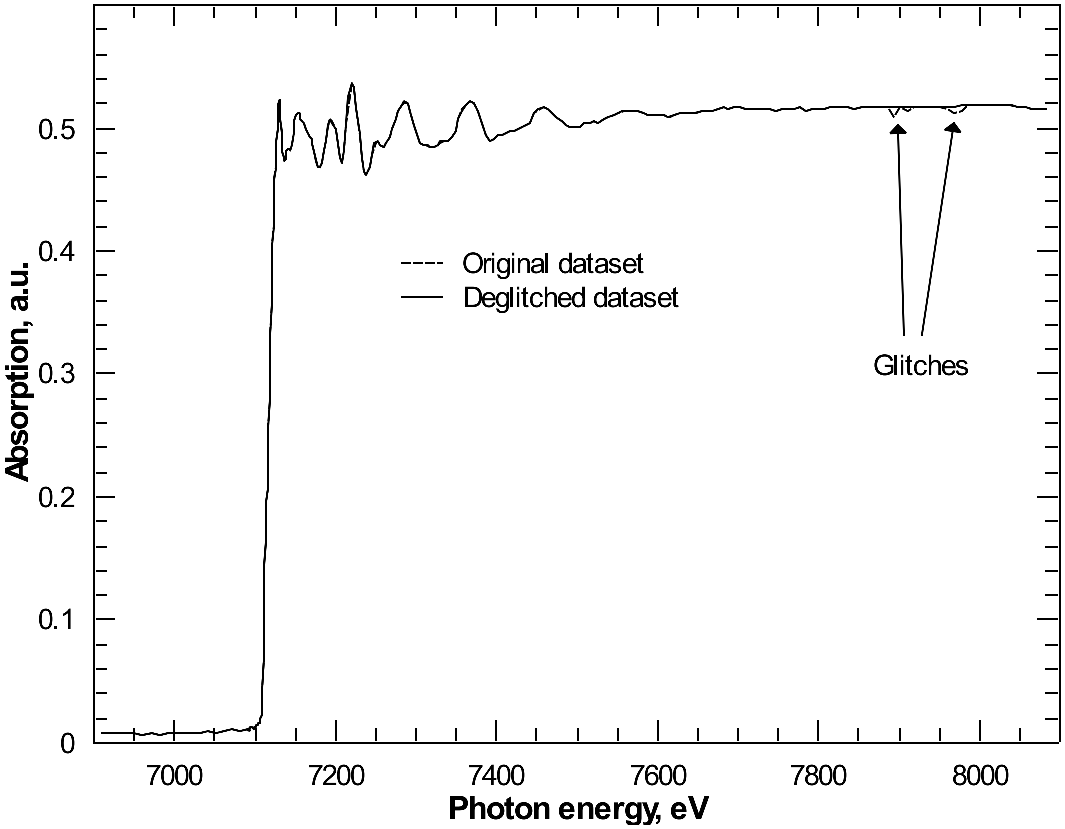

Figure 4.1: 16 ML Fe, $E_{||}$ dataset before and after deglitching. The two indicated glitches are each 3 data points wide.

After the glitches were removed, all datasets were “sieved”: put on the same energy grid. The dataset collected with the smallest monochromator energy step was used as a reference dataset for the sieving process. Inserting an artificial data point between two real data points was done based on a simple 1st degree polynomial fit and was automated using custom software. The reference dataset had at least as many data points as the sieved dataset. Typically, sieving resulted in a small energy shift for each data point for each dataset (see Fig. 4.2).

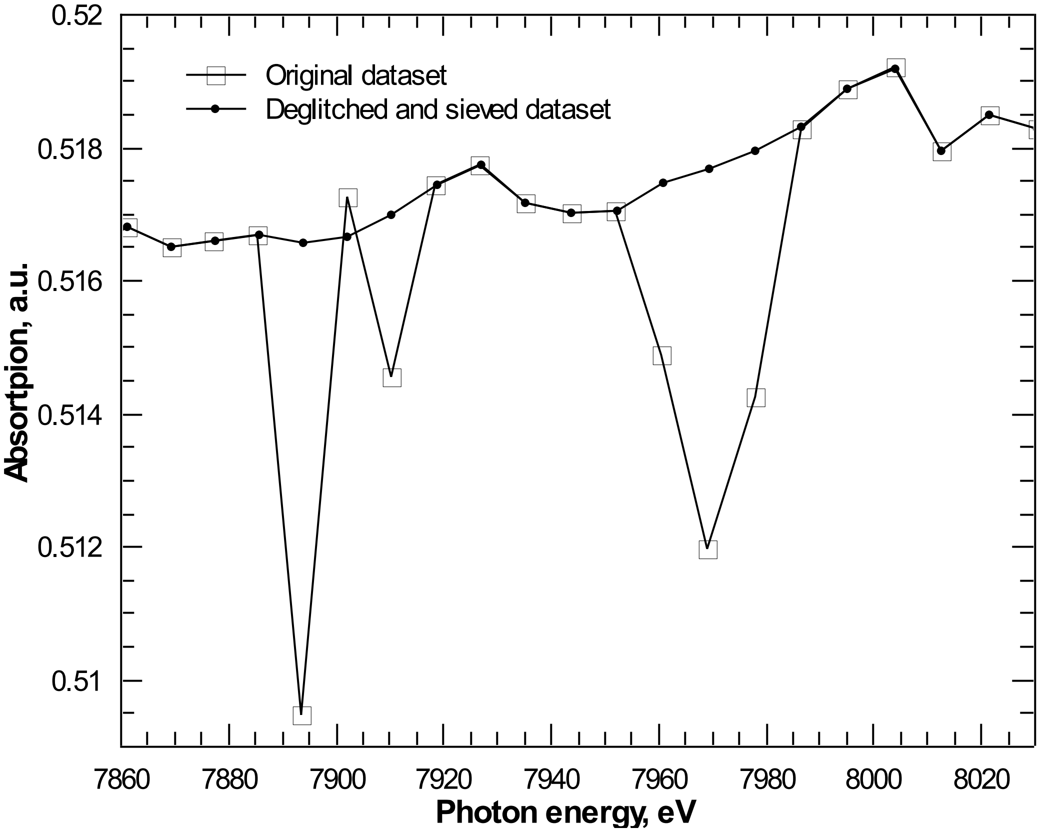

Figure 4.2: 16 ML Fe, $E_{||}$ dataset glitch region before and after deglitching and sieving. Both glitches are 3 data points wide and were removed using 3rd degree polynomials.

In the next stage, the processed datasets were averaged to increase signal-to-noise ratio. This is a straightforward, self-explanatory operation. The resulting averaged dataset was now ready for the XAFS analysis.

4.2 XAFS Analysis

4.2.1 Background Removal and Fourier Transform

An important step in the XAFS analysis was removal of the smooth atomic absorption background from the averaged dataset. For that, firstly, the edge energy, E_0, had to be determined. The edge energy is commonly defined as the position of the first inflection point in the data in the edge region. At the inflection point the first derivative of the data has a maximum and, consequently, the second derivative is equal to zero. Figure 4.3 shows the data for 24 monolayers Fe in $E_\perp$ mode along with its first and second derivatives. It is clear that due to the discrete nature of the data, the position of the actual maximum in the first derivative is different from the one observed. In principle, the top part of the peak in the first derivative should be fitted to a bell-curve function. The maximum of the fit then corresponds to the position of the actual inflection point. In practice, however, given the large number of the datasets being processed and due to the simplicity of the overall shape of the first derivative the actual fitting was avoided and the selection of the E_0 value was done manually by visual inspection.

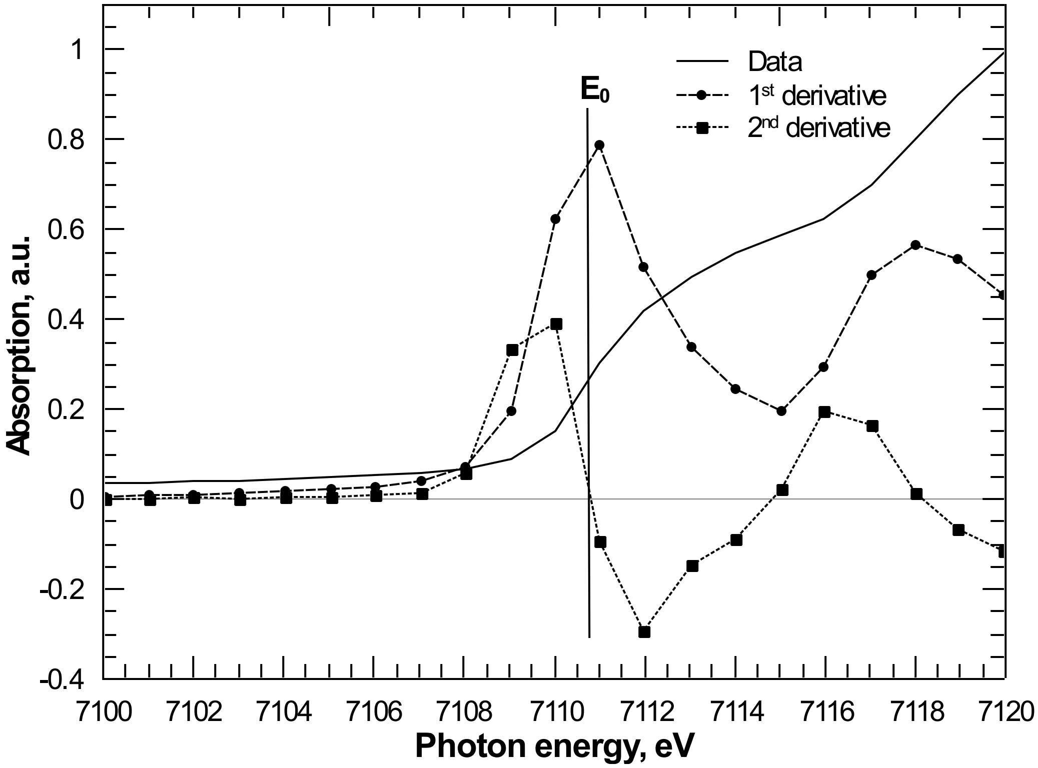

Figure 4.3: 24 ML Fe, $E_\perp$ averaged data along with its first and second derivatives. E_0 position is indicated.

After the E_0 was determined, the actual background removal procedure was done using the AUTOBK software package [2]. It utilizes the fourth-order basis splines (B-splines) with knots equally spaced in k-space to minimize the leakage of the background into the first shell [3]. The fourth-order (cubic) B-spline is a sequence of cubic polynomials connected at the knots between them. The choice of cubic polynomials is governed by the condition that the spline will not have more than one oscillation between the knots, making R_{bkgd} the highest measurable R.

At each knot, the spline is allowed one degree of freedom: the value of the polynomial and its first two derivatives are required to be continuous, while one variable is left free. The free variable can be interpreted either as the value that the spline must assume at the knot, or the discontinuity in the third derivative at the knot. That means that the spline is not required to pass through the actual data at the knots.

The main idea of the AUTOBK was described briefly in Chapter 2 of this thesis. It is based on the idea that the real and imaginary part of the Fourier Transform (FT) of the $\chi(k)$, $FT(R)$, should be minimized in the low-R region below a certain distance, R_{bkgd}. R_{bkgd} should be sufficiently high to remove a smooth atomic background and sufficiently low in order not to remove any XAFS oscillations from the data. In practice, it is achieved by generating several background functions (and XAFS interference functions $\chi(k)$) for different physically meaningful values of R_{bkgd} and comparing the resulting FT. Figures 4.4, 4.5 and 4.6 illustrate this approach for different values of R_{bkgd}.

Figure 4.4 shows $E_{\|}$ Pd K-edge data for 7 monolayers Pd grown on 38.5 monolayers of Fe along with several background functions created with AUTOBK using different values of R_{bkgd} indicated in the figure. First of all, there is a sharp δ-function-like peak in the $R_{bkgd} = 2.39$ Å background function right at the edge energy E_0 (2350.58 eV in this case). This an artifact which occurs sometimes at the ends of the data range because the spline is not forced to go though the actual data points at the knots as discussed above. For the knots in the middle of the spline it is an advantage to allow a more accurate approximation of the smooth background function. The artifact does not occur there, because on the both sides of the knot the cubic polynomials are fitted to the actual data. But at the end knots there is only one polynomial: the spline does not extend outside the data range. As we see, this might result in the abrupt deviations of the background function from the actual data in these points. Usually, however, these artifacts near E_0 do not pose a problem for the analysis of the $\chi(k)$: they lie at E_0 ($k = 0$) and die out very quickly, well within the XANES region of XAFS, and do not affect the EXAFS region (see Fig. 4.5). For the same reason there are discrepancies between the background functions $R_{bkgd} = 0.49$ Å and $R_{bkgd} = 2.39$ Å at the high energy end of the data. This, however, does create a problem, since it happens within the EXAFS region. It means that effectively the high k-end of the $\chi(k)$ will have to be discarded, lowering resolution in the R-space, and is highly undesirable.

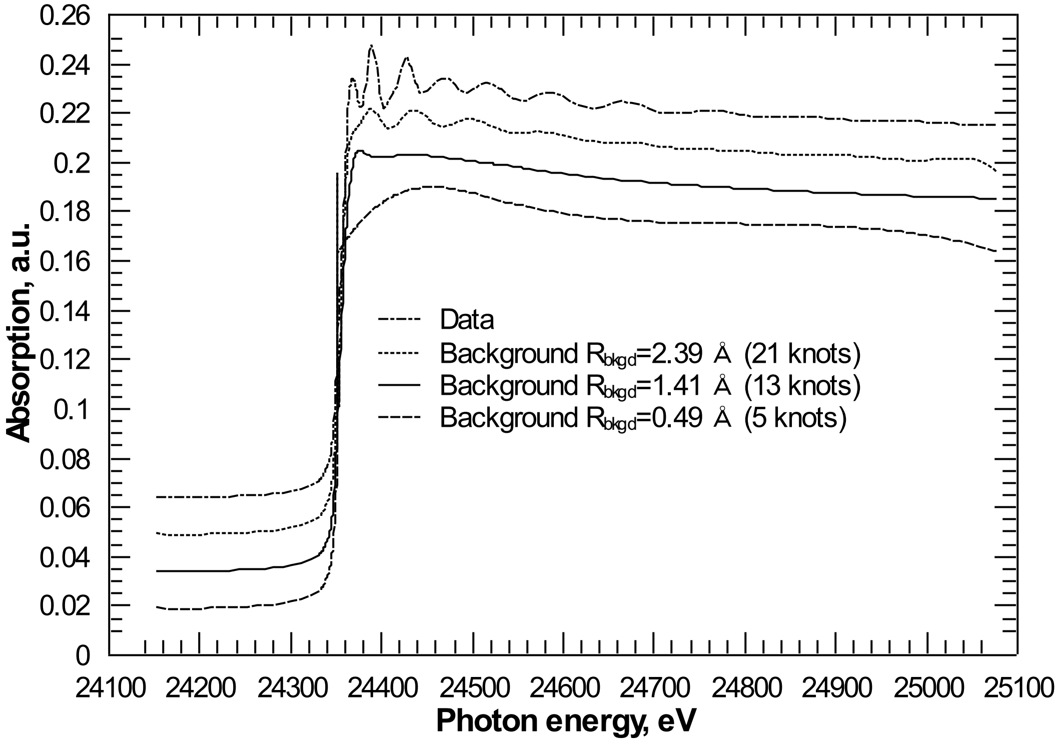

Figure 4.4: 38.5 ML Fe/7 ML Pd, $E_{||}$ data along with three background functions for different R_{bkgd} as indicated. The plots are offset for clarity.

Finally, the $R_{bkgd} = 2.39$ Å background function clearly follows low frequency EXAFS oscillations, while the $R_{bkgd} = 0.49$ Å background function has a slow varying component that does not follow the data (both in the approximate photon energy range $[E_0, \approx E_0 + 200$ eV$] \equiv [24350.8$ eV$, \approx 24550.8$ eV$]$). This is a clear indication that in the first case the spline is not stiff enough and R_{bkgd} should be decreased, while in the second case the spline is overly stiff and R_{bkgd} should be increased.

Figure 4.5 shows three $\chi(k)$ obtained by subtracting the three background functions from the data. The minimum k-value shown is the value used in subsequent Fourier Transform. Notice, that there is virtually no effect in the $\chi(k)$ for $R_{bkgd} = 2.39$ Å from the E_0 glitch in the background function in the low-k region. Overall, while there are some amplitude variations, it is not apparent which background removal was the most successful, except for the low frequency oscillation in $\chi(k)$ for $R_{bkgd} = 0.49$ Å noticeable in 5-12 Å^{-1} k-range. However, the high-k regions for both $R_{bkgd} = 0.49$ Å and $R_{bkgd} = 2.39$ Å $\chi(k)$ exhibit undesirable background removal artifacts due to the end data points, effectively limiting the k-range of the meaningful data.

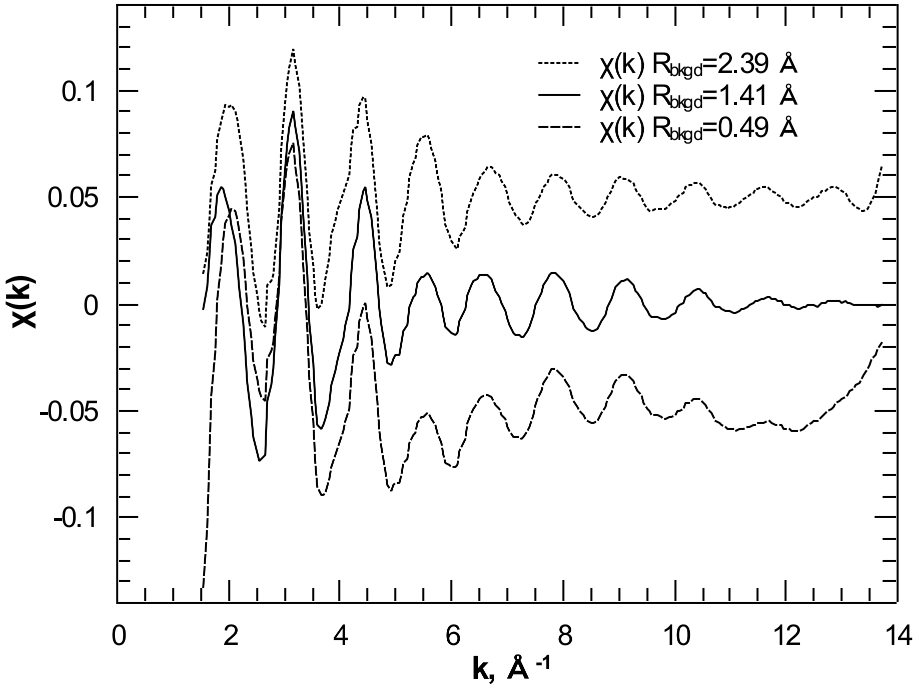

Figure 4.5: 38.5 ML Fe/7 ML Pd, $E_{\|}$ $\chi(k)$ for three background functions for different R_{bkgd} as indicated. The plots are offset for clarity.

Figure 4.6 shows the $\|FT(R)\|$ for all the three $\chi(k)$. The Fourier Transform was done using a 20% Gaussian window over the k-range shown in the figure 4.5 with k-weight of 1.

For the XAFS interference function, $\chi(k)$, which is, essentially, a sum of sine functions complexly modulated in amplitude and phase, the FT served as a frequency filter. However, since our data has a finite k-range ([1.55 Å, 13.75 Å] in shown case), these sine functions are discrete: they are a product between infinite sine functions and a step function equal $\begin{cases} 1 & k_{min} \leq k \leq k_{max} \\ 0 & \text{otherwise} \end{cases}$. As a result, the FT will exhibit a series of equally spaced satellite peaks of decreasing amplitude on both sides of the main peak corresponding to the main frequency. More specifically, the FT of such product is the sinc $x = \frac{\sin x}{x}$ function. Overlapping of these satellite peaks with real peaks at the other frequencies leads to the effect of spectral leakage - major distortion in the XAFS signal in the R-space. To minimize the amplitude of the satellite peaks, the $\chi(k)$ is usually multiplied by a window function that has an amplitude damping effect towards the end points of the data. The 20 % Gaussian window used in this thesis reduces amplitude at the end points by 80 %. The k-weighting of the data was done to increase the amplitude of the data features in the high-k part which is subject to several damping factors as can be seen from the EXAFS equation 2.5 in Chapter 2. The k-range is chosen in such a way that the value of the signal is equal to 0 in the end points to avoid occurrence of additional artifacts in the FT due to the step.

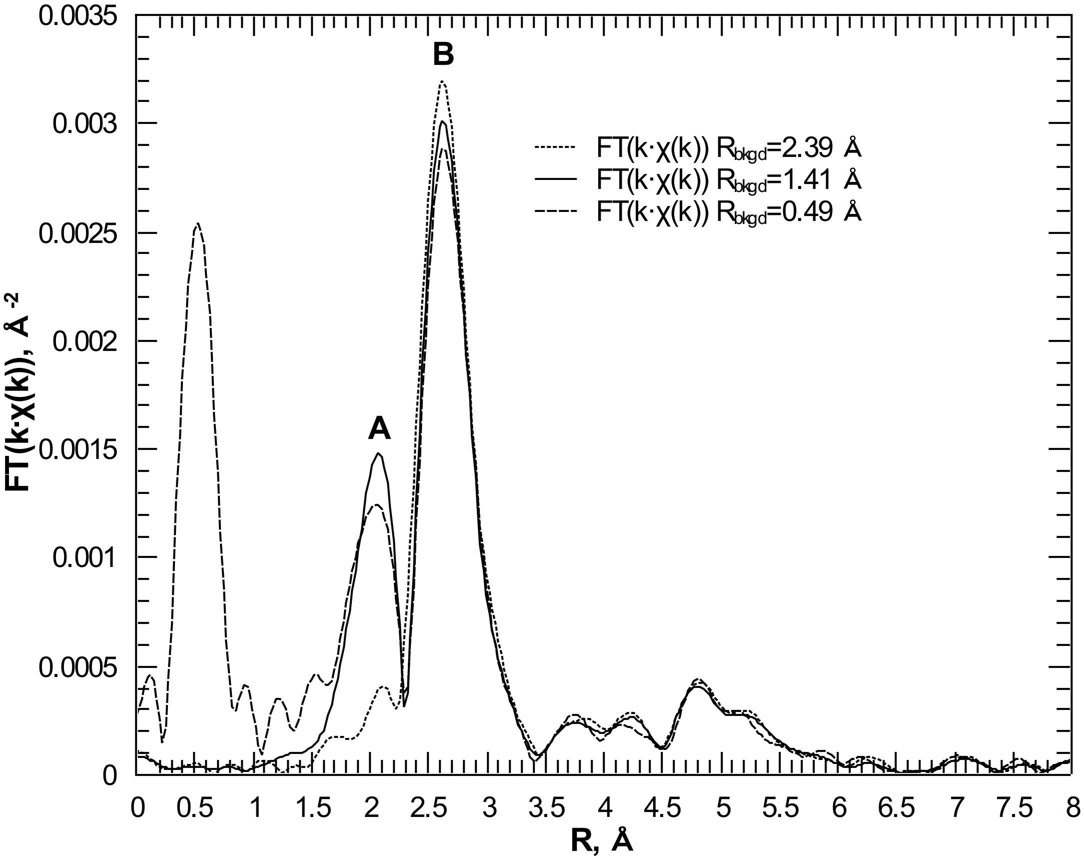

Figure 4.6: 38.5 ML Fe/7 ML Pd, $E_{\|}$ $\|FT(k \cdot \chi(k))\|$ for three background functions for different R_{bkgd} as indicated.

In Figure 4.6 all peculiarities of the different background functions become apparent. The high-R region above the peak B looks very similar for all three $FT(k \cdot \chi(k))$. This is expected, since high R correspond to higher frequencies in k-space (scatters at large distance from the absorber). Evidently, the oscillations observed in the background function for $R_{bkgd} = 2.39$ Å (Fig. 4.4) do not contain any of those high frequencies.

The low-R region for $\|FT(k \cdot \chi(k)\|$ for $R_{bkgd} = 0.49$ Å contains an expected peak corresponding to the low frequency oscillations noticed in Figure 4.5. It is a non-physical artificial feature coming from the slow-varying smooth atomic background, since there can be no backscatter at such small distances for this sample. The other two $\|FT(k \cdot \chi(k)\|$ are essentially identical in this region.

The most pronounced difference occurs under the two central peaks labelled A and B. the k-dependence of the Pd backscattering amplitude (see Appendix C for details) produces a double-peaked feature in the FT such as the two peaks seen. In addition, contribution from the Fe scatterers can also fall under these peaks, mostly under the peak A. Consequently, both peaks have physical meaning and should be present in the FT. While they are both present in $\|FT(k \cdot \chi(k)\|$ for $R_{bkgd} = 0.49$ Å and $R_{bkgd} = 1.41$ Å, peak A is absent in the curve for the $R_{bkgd} = 2.39$ Å.

A conclusion can be made that the background function for $R_{bkgd} = 1.41$ Å is the most reasonable out of all the three presented. It does not contain the unphysical low-R contribution that is present in $R_{bkgd} = 0.49$ Å function. It also retains both physically meaningful peaks A and B unlike the $R_{bkgd} = 2.39$ Å background function.

Figure 4.7 and 4.8 show the obtained $\chi(k)$ for specified thicknesses of the Fe films, up to 30 monolayers, without Pd on top [4].

For the thinnest sample, both polarizations reveal little beyond what appears to be a single frequency in $\chi(k)$. As the thickness increases, additional structure appears that corresponds to the growth of the higher shells. Differences exist between the in-plane and out-of-plane that persist for all of the data. This contrast is most apparent in the interference functions in the range 2.3-7 Å^{-1}.

The in-plane data for thicker samples strongly resemble the reference foil. The out-of-plane data strongly differs from the foil and in-plane $\chi(k)$ in two main regions: in the reduced feature near 4.6 Å^{-1} and in the absence of a feature near 6 Å^{-1}. This is a strong indication that a structural distortion - the distortion to a body-centred tetragonal structure (bct) - is present.

Figure 4.9 shows the $\chi(k)$ for the thickest Fe measured - 38.5 monolayers [5]. On this sample, the measurements on the Fe K-edge were done before and after deposition of Pd. The measurements after the deposition of Pd were performed with angle of incidence twice that of the critical angle. This was to enable the X-ray to penetrate the overlayer of deposited Pd and probe the underlying Fe.

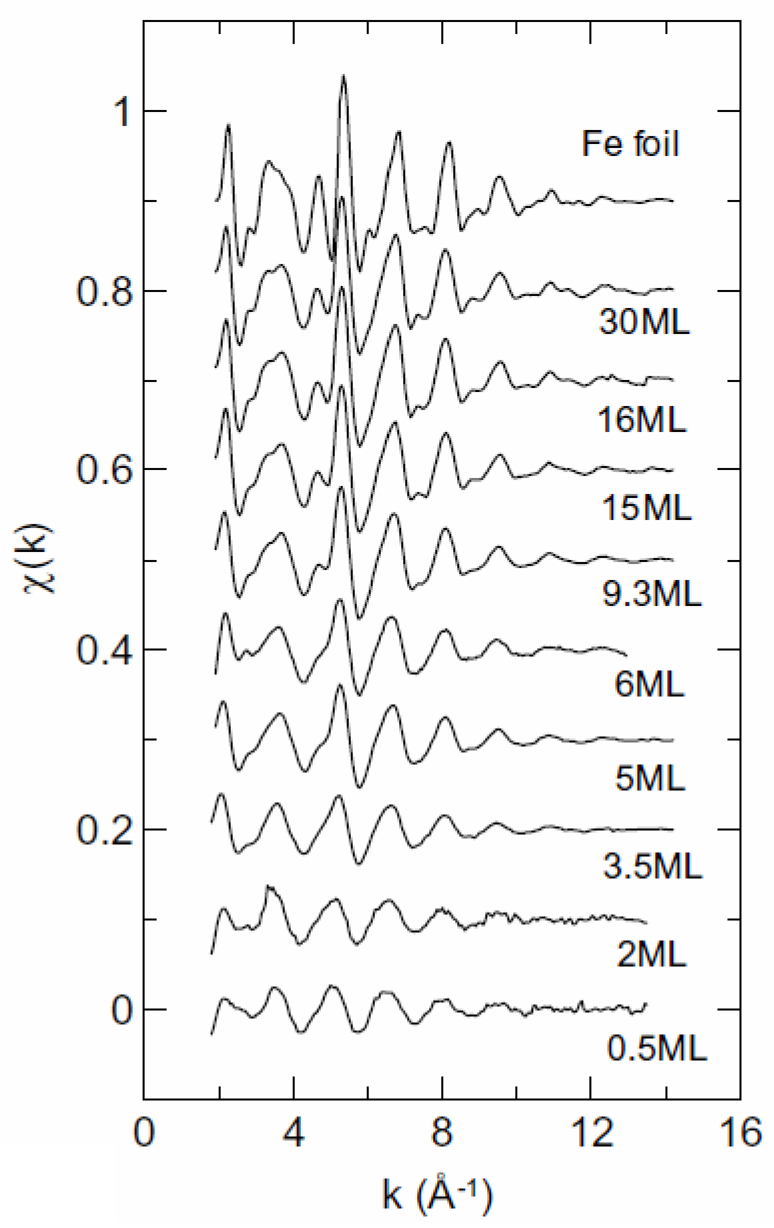

Figure 4.7: The Fe K-edge EXAFS interference functions, $\chi(k)$, with X-ray polarization out-of-plane ($E_{\perp}$) 0.5-30 monolayers thick Fe.

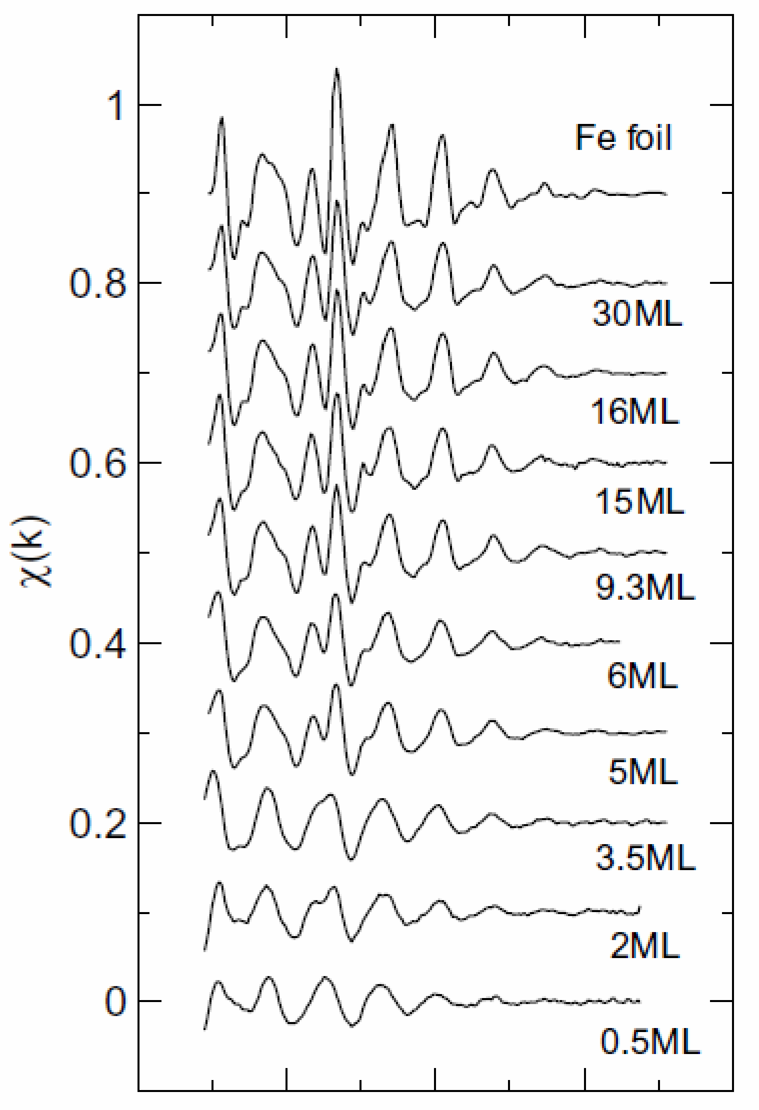

Figure 4.8: The Fe K-edge EXAFS interference functions, $\chi(k)$, with X-ray polarization in-plane ($E_{\parallel}$) 0.5-30 monolayers thick Fe.

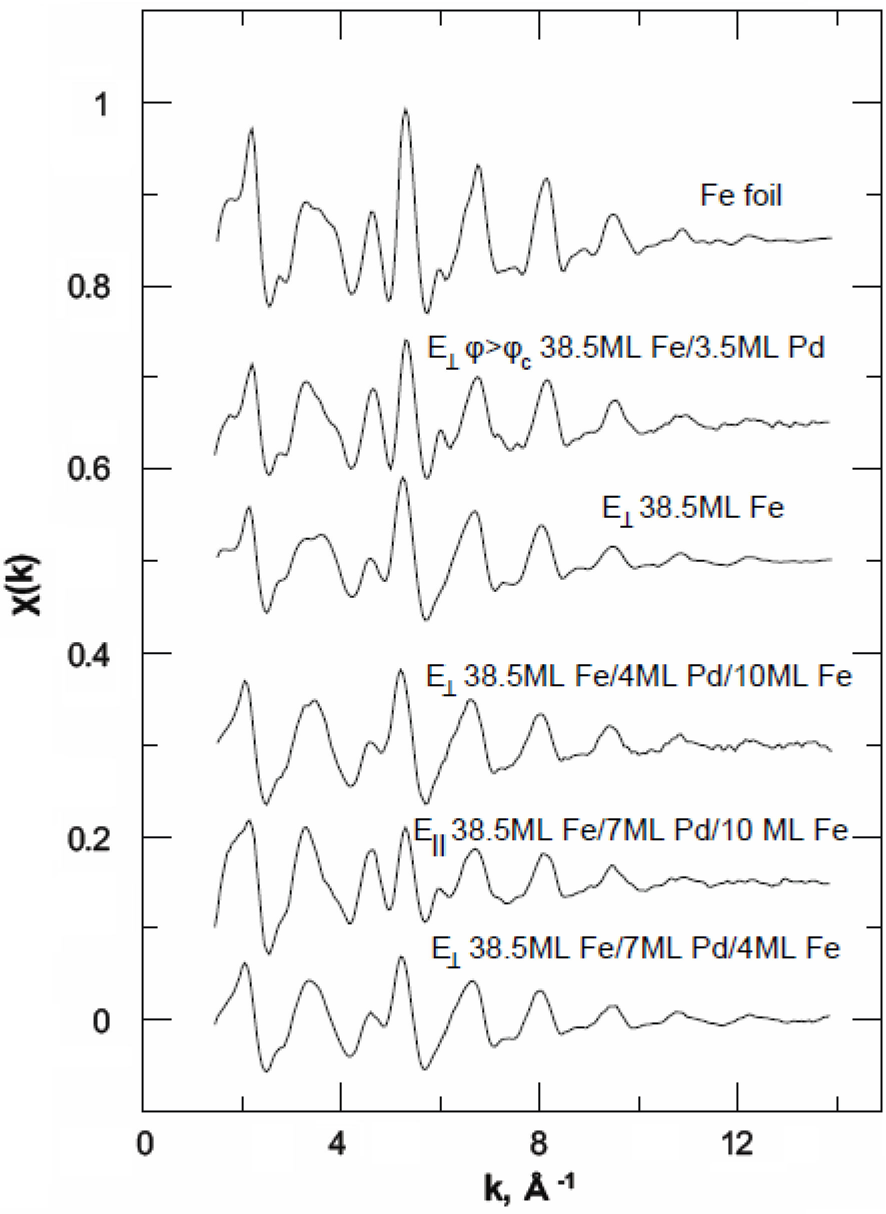

Figure 4.9: The Fe K-edge EXAFS interference functions, $\chi(k)$, with X-ray polarization in-plane and out-of-plane for Pd and Fe films of different thickness. The angle of incidence on the films is $2/3\varphi_C$, except for the upper $\chi(k)$ where it is $2\varphi_C$.

The characteristic differences between the $\chi(k)$ of iron foil over the range 3 to 7 Å^{-1} and $E_\perp$ of the 38.5 monolayer sample indicate that the latter has a bct structure. When 3.5 monolayers of Pd were deposited and the structure of the iron probed by XAFS measurements at $2\varphi_C$, the similarity of in-plane data to iron foil indicates that the overlayer of Pd has not significantly changed the bct structure of the underlying 38.5 monolayers Fe. When 10 monolayers Fe were deposited on 7 monolayers of Pd, the out-of-plane $\chi(k)$ is similar to the out-of-plane $\chi(k)$ for the bct 38.5 monolayers Fe. However, for the initial 4 monolayers Fe grown on Pd, inspection of the $\chi(k)$ for the in-plane and out-of-plane indicates differences over the 3 to 4 Å^{-1} range.

Figure 4.10 shows the Pd K-edge $\chi(k)$ for Pd grown on top of 38.5 monolayers samples [5].

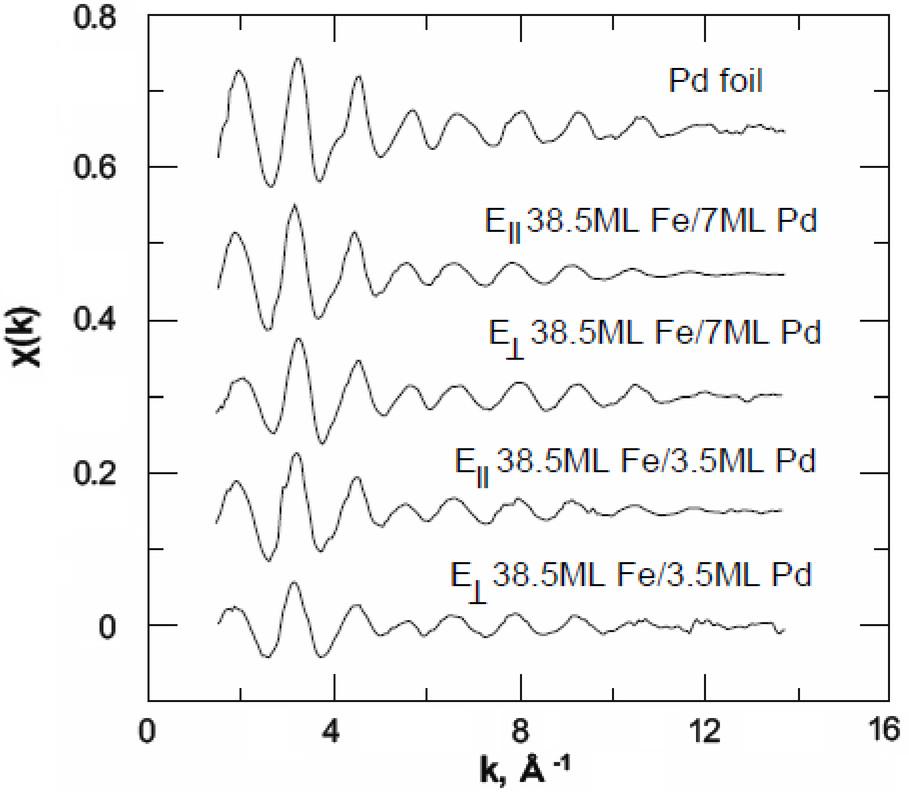

Figure 4.10: The Pd K-edge $\chi(k)$ for the X-ray polarization in-plane and out-of-plane for Pd films of different thickness.

Relative to Pd foil, at high k, the $\chi(k)$ of the films have decreased amplitudes and appear to contain only a single frequency. There are differences over the range 3 to 5 Å^{-1}. The change of slope at 4 Å^{-1} is less pronounced for in-plane polarization in the 7 monolayers data than in the Pd foil. The $\chi(k)$ for in-plane polarization for 7 monolayers has a change of slope at 3 Å^{-1} not observed in the foil. The out-of-plane $\chi(k)$ is different from the in-plane over the range 3 to 5 Å^{-1}, for example, the first and the second minima differ in depth. In the 3.5 monolayers data the $\chi(k)$ for out-of-plane polarization is similar to that for 7 monolayers, however, notice the fourth peak amplitude is bigger for the thicker Pd

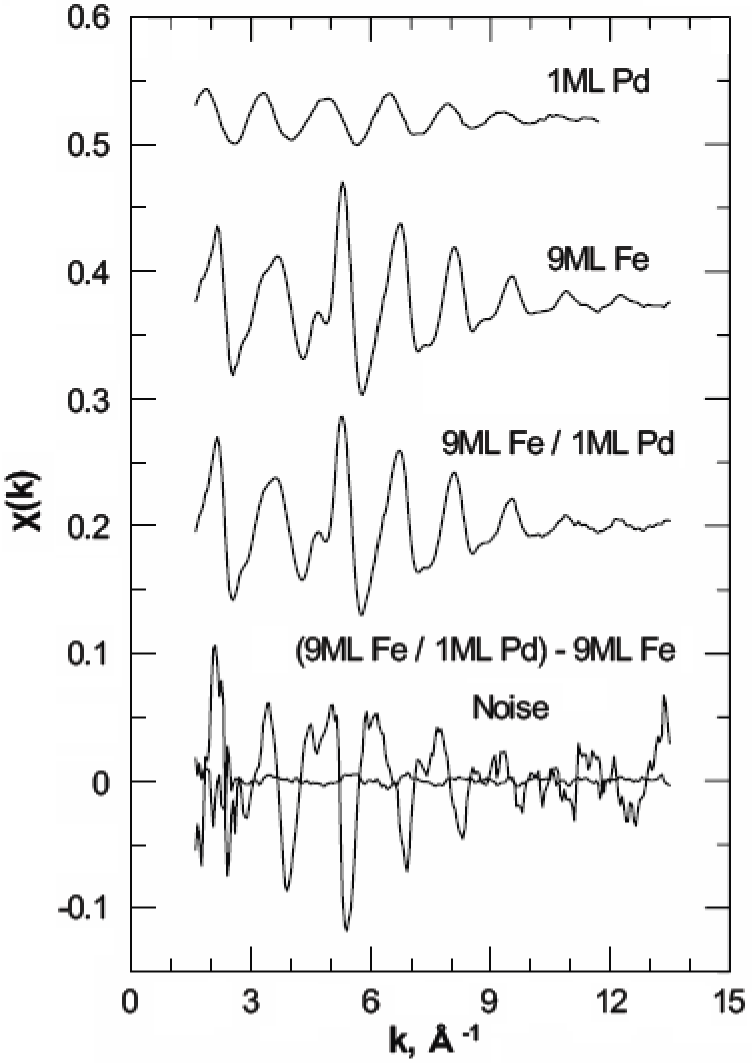

Figure 4.11: The Fe and Pd K-edge $\chi(k)$ for the X-ray polarization out-of-plane for 1 monolayer Pd grown on top of 9 monolayers Fe, the difference (×10) between two Fe spectra, and the noise level (×10).

sample. There are also subtle differences between in-plane and out-of-plane $\chi(k)$ in the 3.5 monolayers data.

Finally, figure 4.11 shows Fe and Pd K-edge out-of-plane polarization $\chi(k)$ for a 1 monolayer of Pd grown on 9 monolayers of Fe [6]. Unlike the 38.5 monolayers sample, Fe was not sputtered and annealed before Pd growth. The difference between the two Fe $\chi(k)$ is shown together with the noise level included for comparison (both are multiplied tenfold). The main contribution to the difference $\chi(k)$ is caused by the dissimilarities "seen" by Fe atoms in the top few layers. This asserts that glancing incident XAFS is sufficiently surface sensitive to investigate small changes in the interfacial region. The difference $\chi(k)$ helped establish a suitable model for curve fitting. Additionally, simultaneous fits to the Pd data and the difference $\chi(k)$ were used to verify the quality of the subsequent fits.

4.2.2 Fitting of the Data

After the background removal and the Fourier Transform were performed the fitting was done in R-space simultaneously on $E_\perp$ and $E_\parallel$ data. Simultaneity of the fitting is essential since data for each polarization includes the EXAFS information from the same scatterers as well as information unique to a given polarization. For example, the first nearest neighbour in body-centered cubic (bulk Fe) or face-centered cubic (bulk Pd) crystal structures is the same for both polarizations: in both cases there are atoms located in the corners of the unit cell. The angle between the polarization vectors and the radius vector from the absorber to these atoms is $\approx 45°$, meaning they will contribute to the EXAFS signal in both $E_\perp$ and $E_\parallel$ data. In the fit, the fitting parameters to such scatterers were correlated to be the same in both fits.

The non-linear least-squares minimization of the real and imaginary parts of FT of the model EXAFS equation 4.1 to the FT of the data was done using WinXAS and IFEFFIT (Athena) software packages [7, 1, 8].

$$\chi(k) = \sum_i \frac{N_i}{kR_i^2} S_0^2 F_i(k) e^{-2R_i/\lambda_i(k)} e^{-2k^2\sigma_i^2} \sin(2kR_i + 2\delta(k) + \phi_i(k)). \tag{4.1}$$

The fitting parameters were coordination numbers N_i, amplitude reduction factor S_0^2, distances to the scatterers from the absorber R_i and the mean square relative displacement, σ_i^2, in the EXAFS Debye-Waller factor $e^{-2k^2\sigma_i^2}$. An additional fitting parameter, ΔE_0, was introduced to compensate for the small possible phase-shift caused by differences between the Fermi level calculated in the model and the zero of the k-space scale. The backscattering amplitude $F(k)$, electron free path $\lambda(k)$ and phase shifts were calculated theoretically using FEFF7 software package [9]. The radial and polarization dependence of the backscattering amplitude were also directly included in the calculations (see Appendix C).

The Fourier Transforms for the Fe films of different thicknesses shown in Figures 4.7 and 4.8 are shown in Figures 4.12 and 4.14, respectively. Overall, the resemblance to bcc iron is quite strong in that there are three main peaks of note in the transform. For bcc Fe, the first peak, near 2.2 Å contains both the nearest neighbour (corner atoms (1)) and next-nearest neighbour (lattice constant away, atom (2)) (see Figure 4.13(a)). The second

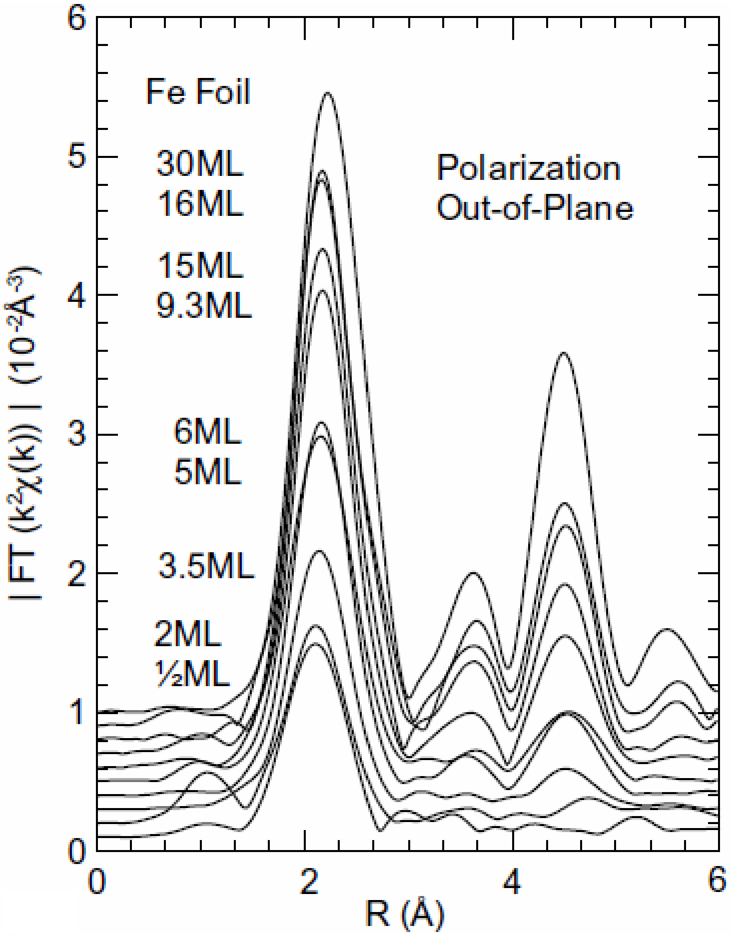

Figure 4.12: Magnitude of the Fourier Transforms of the out-of-plane $\chi(k)$ for Fe films 0.5-30 monolayers thick. The inclusion of the EXAFS phase shift causes the peaks in the Fourier Transform to appear at radial distances shorter than the actual bond lengths.

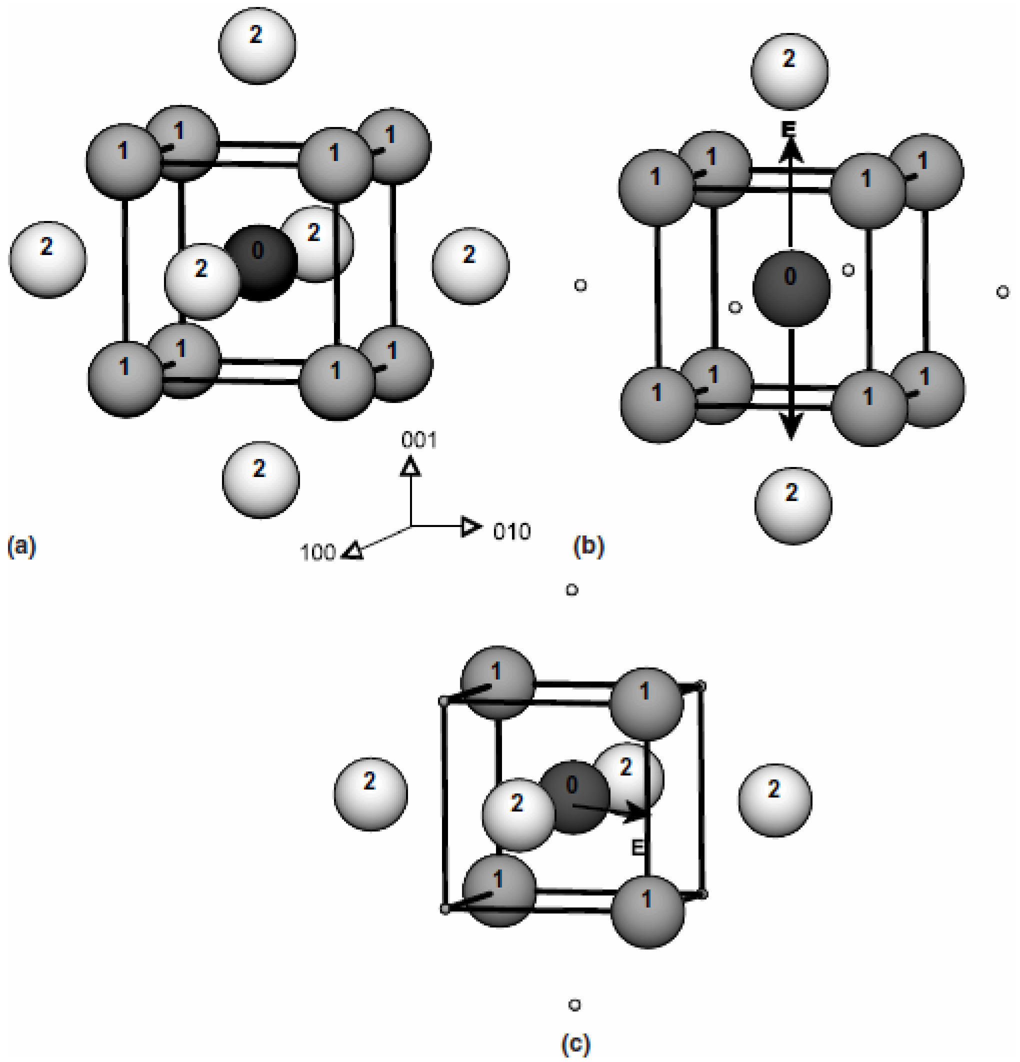

Figure 4.13: The body-centered-cubic structure is shown from an XAFS perspective with central atom 0 absorbing the X-ray and first nearneighbours, 1, and second near-neighbours, 2, scattering the emitted photoelectron in the case of: (a) unpolarized X-rays, (b) X-rays polarized with the electric field vector, E, along the *c*-axis, and (c) X-rays polarized in the (001) plane with electric field vector along the $\langle 110 \rangle$ direction.

(middle) peak is dominated by backscattering along the face diagonal (corner to corner atoms), but also contains some multiple three-leg scattering that tails into the first peak. The multiple-scattering paths are triangular paths that involve the emitted photoelectron either: (a) travelling from an absorbing atom (0) in the body-centered position to an atom (1) at the corner of the unit cell then to another corner atom (1) along a cell edge before returning to the absorber (0); or (b) travelling from absorber atom (0) to a corner atom (1) then to a closest atom (2) that is lattice distance away from the absorber and then back to the absorber atom (0). The third peak, near 4.5 Å is dominated by backscattering and focused multiple scattering along the body diagonal of the unit cell. From an absorbing atom (1) along the body diagonal: (a) to the backscattering atom (1) in another corner and back

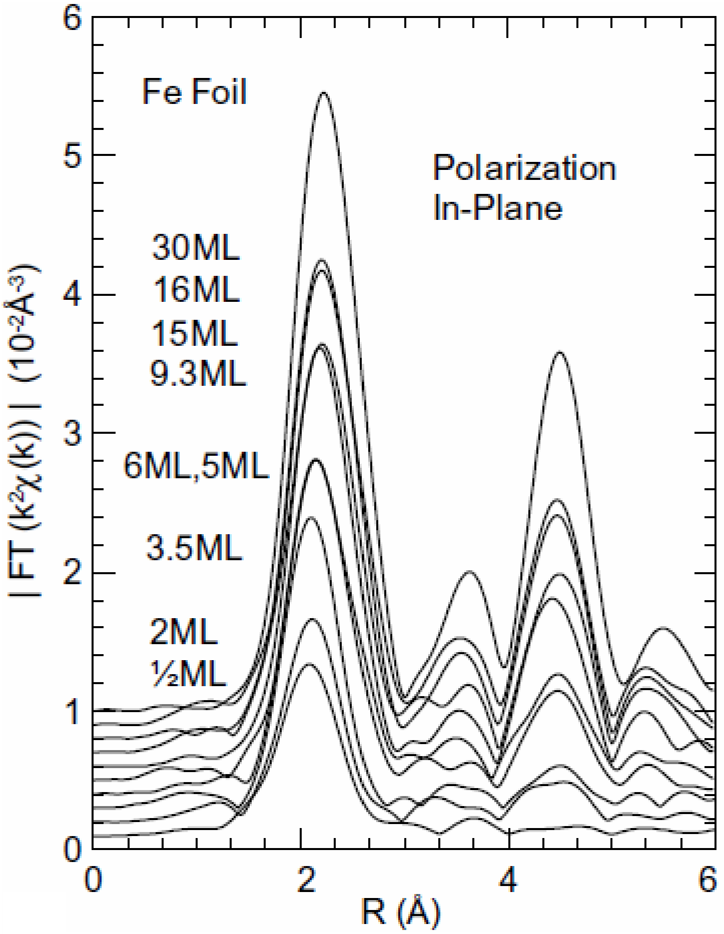

Figure 4.14: Magnitude of the Fourier Transforms of the in-plane $\chi(k)$ for Fe films 0.5-30 monolayers thick.

to the absorber (1); (b) to the forward scatterer (0) then continuing to the backscattering atom (1) and back to the absorber (1); (c) to the backscattering atom (1) in another corner then back to the forward scattering atom (0) and, finally, back to the absorber (1). Vestiges of this peak remain even down to 3.5 monolayers, even though few unit cells are present for the out-of-plane polarization.

The absorption of the linearly polarized X-rays causes the ejected photoelectrons to have a dipole-like distribution with high probability of the photoelectron being emitted along the direction of polarization and negligible probability perpendicular to the polarization. Figure 4.13 illustrates the implications of such polarization dependence on the backscattering from nearby atoms, which affects the XAFS oscillations in the absorption spectrum, for a body-centered-cubic-related structure. An absorbing atom, 0, has eight nearest neighbours, 1, and six second-nearest neighbours, 2 (Fig. 4.13(a)). For X-rays incident along the $\langle 001 \rangle$ direction (perpendicular to the substrate), atoms 1 in the first shell all contribute, but only the atoms 2 located directly above and below the absorber 0 at the c-lattice constant contribute to the second shell (Fig. 4.13(b)). For polarization along $\langle 110 \rangle$ ((Fig. 4.13(c))), only half the atoms labelled 1 contribute to the first shell and the 4 atoms labelled 2 in the (001) plane contribute to the second shell. We have applied this method to the iron films being studied in order to extract details on the nearest-neighbours and the second nearest-neighbours, information which contains the lattice constants and permits an examination of the distortion from body-centered cubic.

Figure 4.15 shows the magnitudes of the Fourier Transforms for Pd films of different thicknesses grown on 38.5 monolayer Fe. The splitting of the main peak into A and B is produced by the k-dependence of the Pd backscattering amplitude, $F(k)$, when convolved with the nearest neighbour distribution function. Inspection of the figure reveals the peak ratio B/A decreases as the thickness of the film decreases. This is caused by backscattering from the underlying Fe, some of which has alloyed with Pd. Figure 4.16 shows the magnitude of the Fourier Transform for 9 monolayers Fe before and after deposition of 1 monolayer Pd, together with the Fourier Transform of 1 monolayer Pd.

The models of the thin films for the theoretical calculations were generated using ATOMS software package [10]. It takes a user-defined unit cell and crystal symmetry rules and generates a cluster of atoms, specifying their atomic coordinates with respect to the center of the cluster. The size of the cluster is controlled by the specified maximum radius. Typically, clusters of approximately 300 atoms were used. Several samples can be distinguished: thin

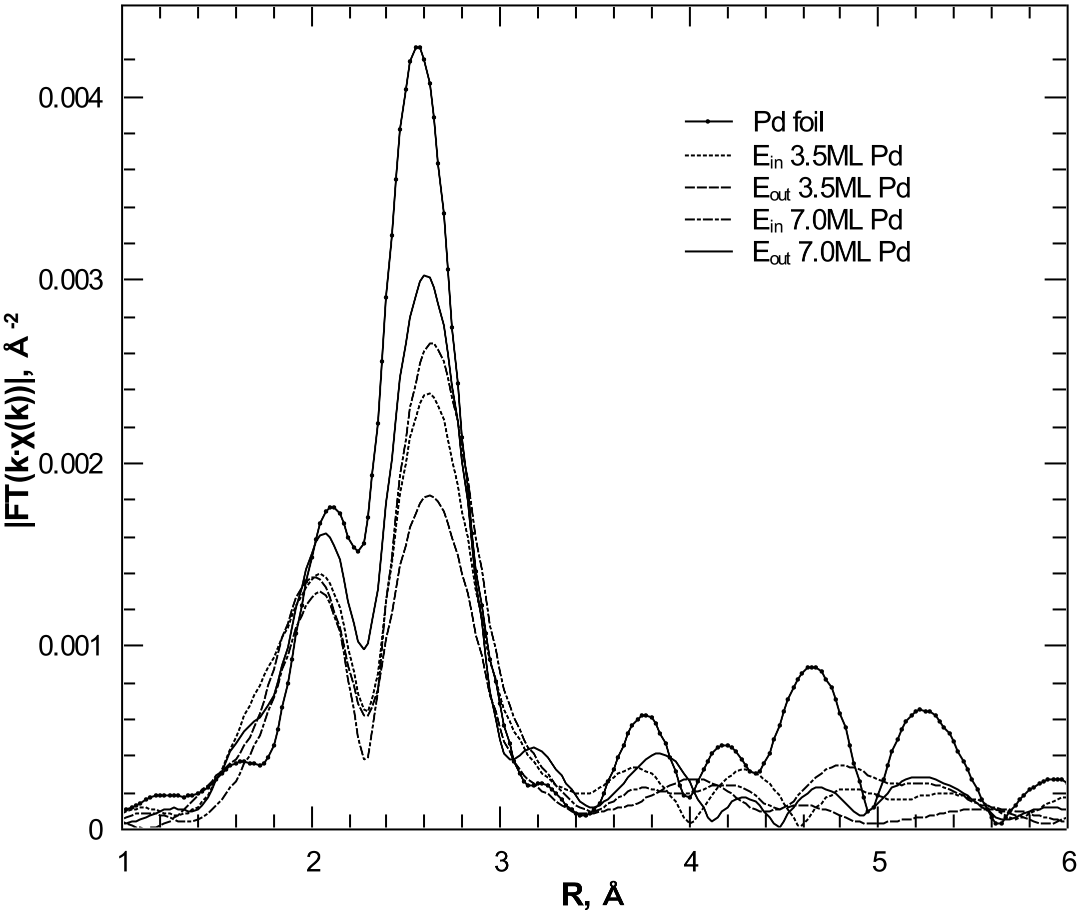

Figure 4.15: Magnitude of the Fourier Transforms of the in-plane and out-of-plane $\chi(k)$ for Pd films 3.5 and 7 monolayers thick.

Fe on top of GaAs, thick Fe, Pd on buffer Fe, and Fe on Pd buffer. For each of the samples, except for the thick Fe, several theoretical models were generated with varying degree of alloying between the layers.

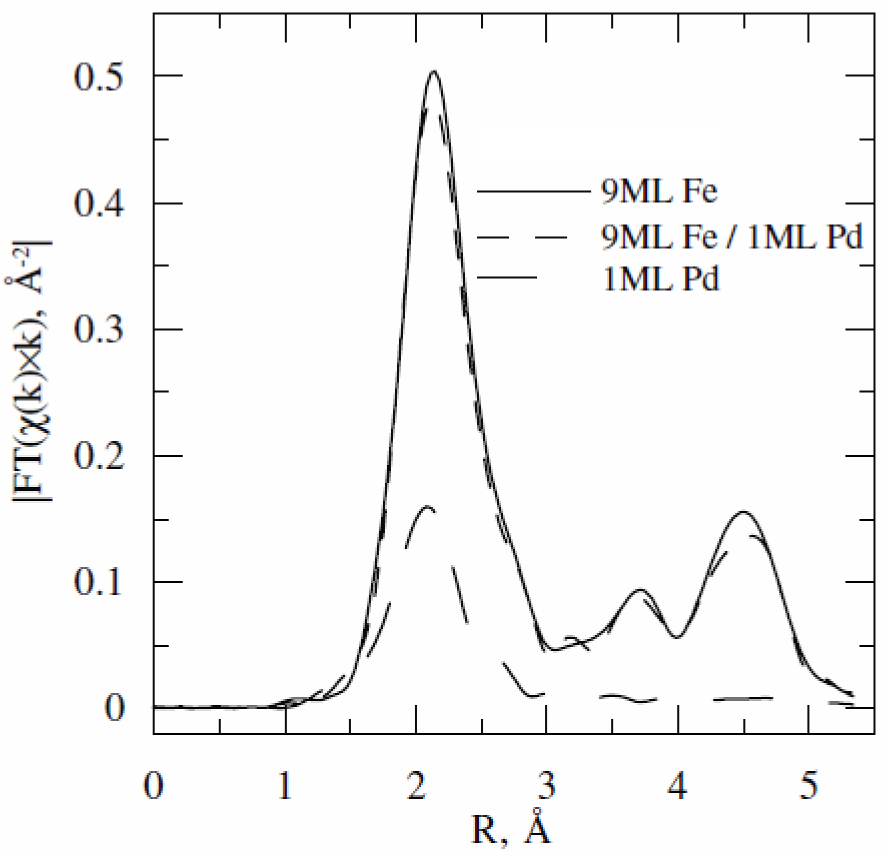

Figure 4.16: Magnitude of the Fourier Transforms of the out-of-plane $\chi(k)$ for 9 monolayers Fe before and after deposition of 1 monolayer Pd (Fe K-edge data), and 1 monolayer Pd (Pd K-edge data).

For the thin Fe with thicknesses between 0.5 and 9.3 monolayers, the idealized structural model for fitting was that of a thin Fe film with infinite smooth sheets capped above by an overlayer of arsenic and below by an underlayer of gallium. Several models with different amounts of alloying were used: 0 %, 12.5 %, 25 % and 50 % where the percentage indicates the number of non-Fe atoms in the first nearest-neighbour shell. Since the models would result in equal amounts of Ga and As in the average iron environment and because from an EXAFS viewpoint the backscattering amplitudes, $F(k)$, of Ga and As are almost indistinguishable (see Appendix C), and in order to simplify the alloy calculation, germanium was used to represent both gallium and arsenic. A similar model that includes the As overlayer was used for the sample of 1 monolayer Pd on top of 9 monolayers of Fe.

For the thick Fe with thicknesses between 9.3 and up to 38.5 monolayers a model of pure Fe on GaAs substrate was used without the capping As overlayer. On one hand this overlayer could not be detected in thicker samples, and on the other, for very thick samples the Fe buffer was sputtered and annealed at the medium thicknesses to remove it.

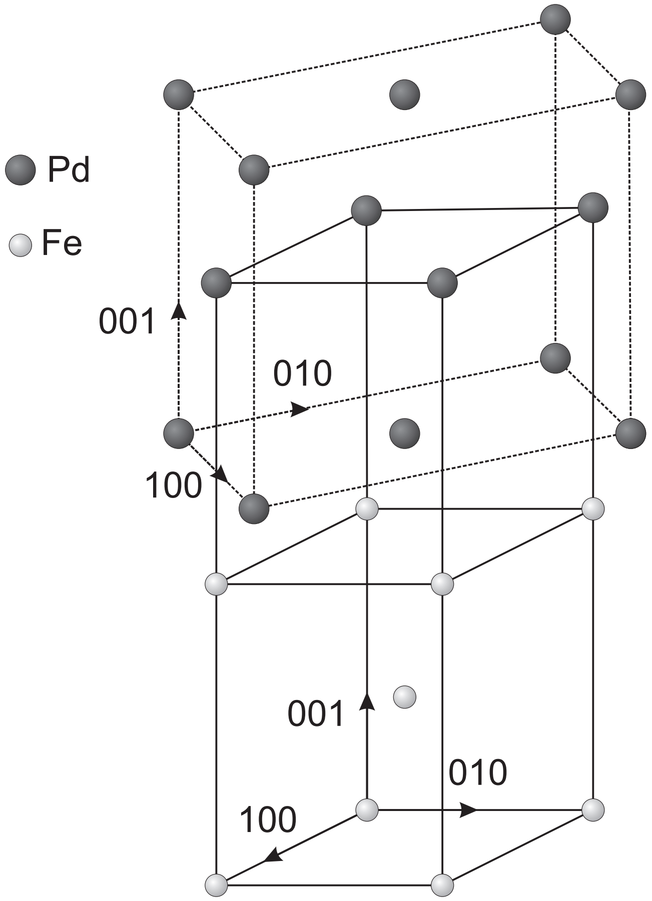

Figure 4.17: Fe (bct) and Pd (fct) unit cells. The bct representation of the fct Pd unit cell is shown. The fct Pd unit cell is rotated 45° along ⟨001⟩ direction.

To model Pd on Fe, several models with different thickness of alloying were used. The atomic species of the Fe was introduced into the first, second and third layers of the Pd overlayer at concentrations decreasing with the number of layers: 50 %, 25 % and 12.5 % Fe, respectively. The model assumed that in the growth of Pd on body-centered tetragonal Fe, the Pd fcc lattice can be considered as a bct structure with in-plane lattice parameter being smaller than the underlying Fe in-plane lattice (Figure 4.17). The Pd fcc lattice rotates 45° with respect to the Fe bct lattice and expands in-plane in an attempt to match Fe. This causes contraction in the out-of-plane direction at the same time. A similar model was used to simulate growth of Fe on Pd.

When fitting the XAFS data one faces the difficulty of having to deal with correlations between the coordination number N_i and the amplitude reduction factor S_0^2 in the amplitude multiplier. To break these correlations, one of these parameters has to be fixed: either N_i based on the assumed model, or S_0^2 based on the value obtained from the reference. Polycrystalline Fe and Pd foils were used as references in this thesis. The k-ranges for the FT for the foils were set to be equal to the k-ranges of the data. In fitting of the Fe data the first approach was chosen, when N_i was fixed according to the model and S_0^2 allowed to be varied. For the Pd data, on the other hand, the S_0^2 was fixed to the value of the Pd foil and the coordination number was allowed to be varied.

After the fits for the foils were obtained, the fitting of the data was done. Initially, just the first peak of the FT was fit for both $E_\perp$ and $E_\|$ data. After the fit became stable, the fitting range was extended gradually to higher R-values while higher coordination shells were being introduced into the fit. The fitting parameters of the lower coordination shells were monitored not to change significantly, while a small change that was attributed to the overlapping of the two shells was accepted.

Figure 4.18 shows the magnitude of the Fourier Transform of in-plane $\chi(k)$ for 3.5 monolayer Pd grown on 38.5 monolayer Fe together with the fit and contributions from Fe and Pd scatterers under the peaks A and B. The imaginary parts of the Fourier Transform for Pd-Fe and Pd-Pd are almost in-phase under peak A but become out-of-phase under peak B. This interference makes the fit sensitive to the Pd-Fe interface. The overall fit was obtained using one Pd-Fe distance and three Pd-Pd distances up to 4.7 Å.

Figure 4.19 shows the fitting of 1 monolayer Pd grown on 9 monolayer of Fe in out-of-plane polarization. Due to the Fe surface roughness and presence of As at the surface, Pd does not form a perfect layer. This is evident from the presence of the Pd-Pd path under the fit - perfect 1 monolayer out-of-plane data would not contain this path, since all Pd atoms would be in-plane. Arsenic atoms from the Fe/GaAs interface tend to float to the top during growth of Fe and Pd [11]. From the fit it is clear that such a small amount of As can be detected because the backscattering amplitude of As differs from both Fe and Pd. There is a complex interplay between the Pd-Fe, Pd-As and Pd-Pd contributions to the main peak. While the Pd-Fe and Pd-Pd imaginary parts of the Fourier Transforms are in phase below 2 Å, they are out of phase just below 2.5 Å.

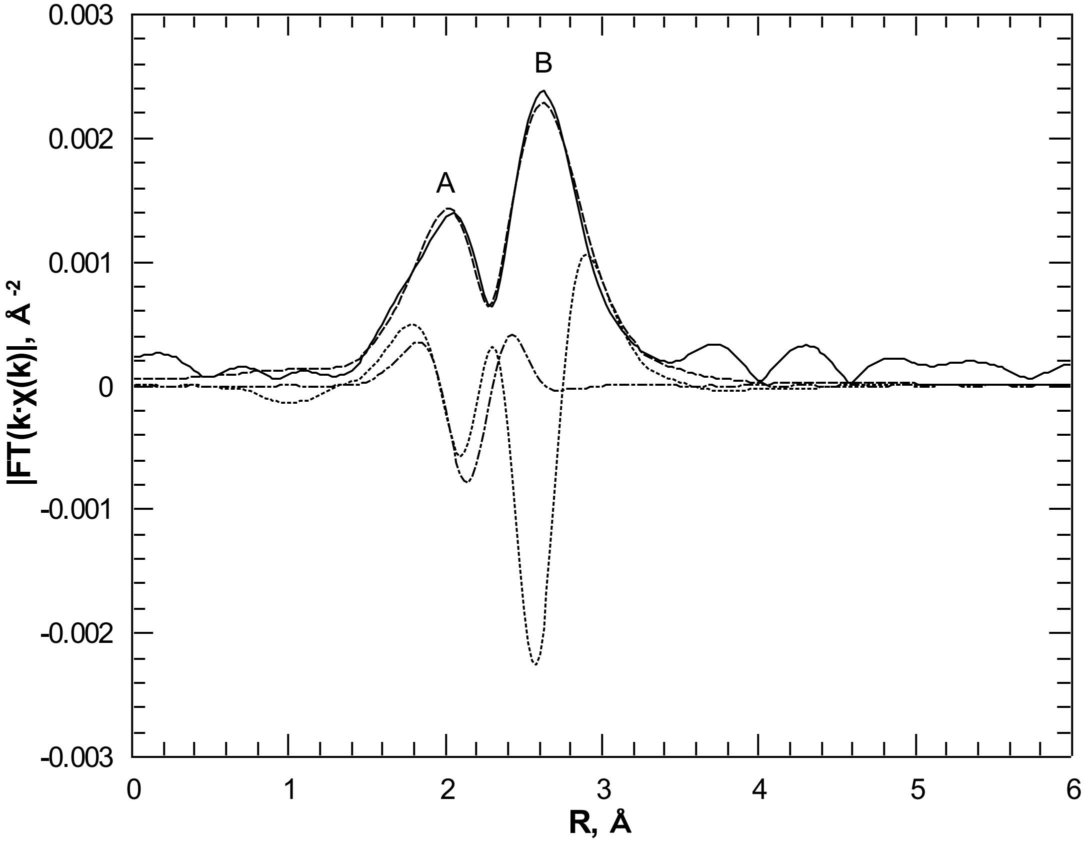

Figure 4.18: The contribution of Fe and Pd to the transform of 3.5 monolayers Pd in the in-plane configuration. The solid line is the magnitude of the FT of the data. The dashed and dotted lines are the imaginary parts of the Pd-Fe and Pd-Pd contributions to the fit of the data, respectively. The broken line indicates the magnitude of the fit including the nearest neighbour Pd-Fe distance and three Pd-Pd distances out to 4.7 Å.

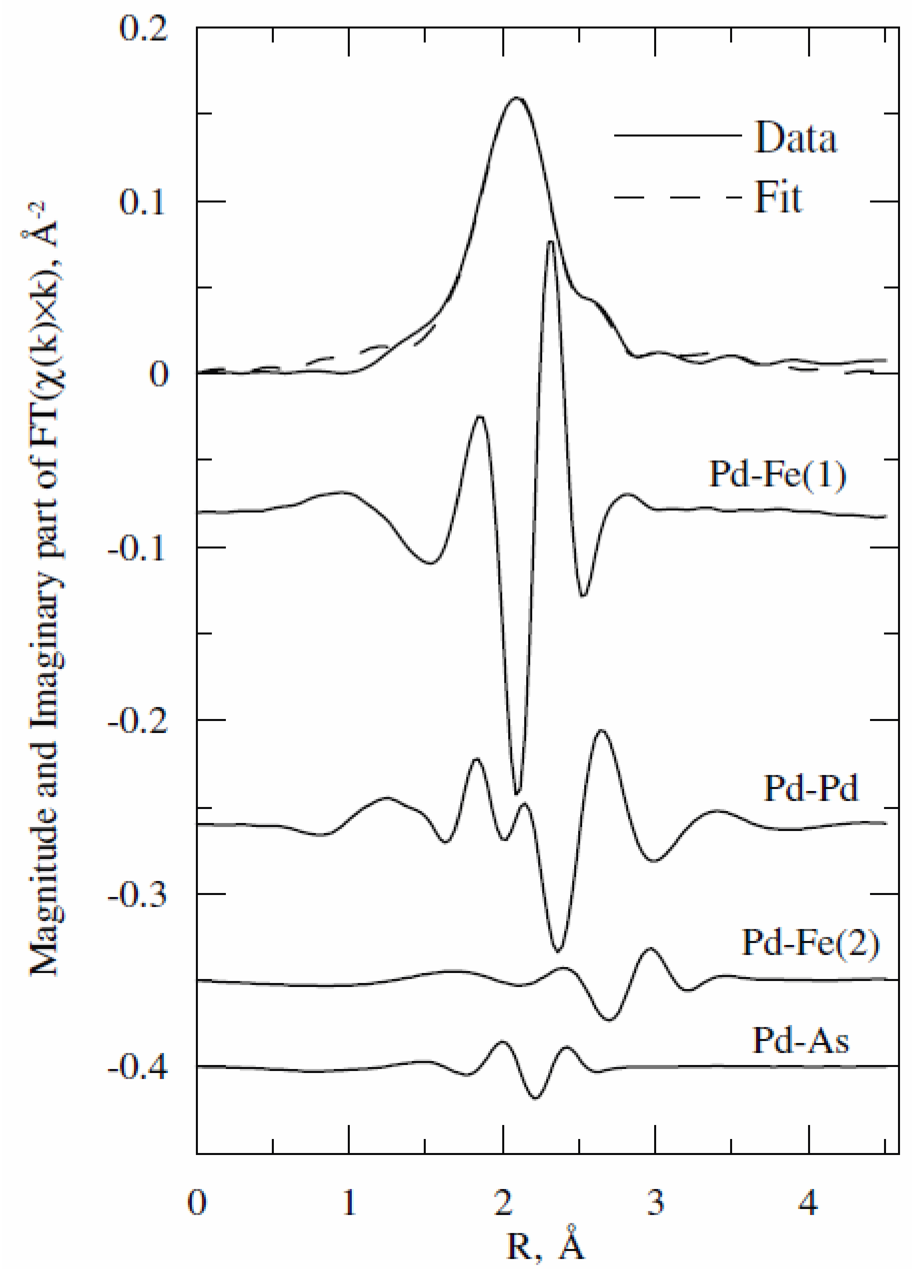

Figure 4.19: The top curve is the Pd K-edge fit for 1 monolayer Pd grown on 9 monolayers Fe in the out-of-plane configuration. Imaginary parts of contributing bonds are offset for clarity below.

Chapter 5

Results

A total of 14 iron films of different thicknesses were grown on GaAs(001)-(4×6) and analysed in several independent experiments. The thicknesses studied were: 0.5, 2, 3.5, 5, 6, 9, 9.3, 14, 15, 16, 24, 26, 30 and 38.5 monolayers. Several palladium films were grown on different iron buffers: 1 monolayer on 9 monolayer untreated iron (the iron film was not sputtered and annealed before palladium deposition); 1 monolayer on 26 monolayers iron. Also, a sample with 3.5 and 7 monolayers (3.5+3.5 monolayers) of palladium were deposited on 38.5 monolayers iron. Two Fe films were grown on the 7 monolayer palladium sample: 4 and 10 monolayers (4+6 monolayers). The results of the analysis are summarized below.

5.1 Fe on GaAs(001)-(4×6)

In this section structural results obtained from polarization-dependent XAFS measurements are presented for Fe epitaxially grown on GaAs(001)-4×6 reconstructed surface. The thicknesses of the films were systematically increased from 0.5 monolayers to 38.5 monolayers.

For iron films, from out-of-plane measurements, the c-axis distance is extracted, while from in-plane, the average a-axis value is obtained. In constructing a structural model to fit the Fe K-edge EXAFS data from thin films it is necessary to include contributions from both Ga and As in the substrate. Since it is known that up to one monolayer of As diffuses from the substrate and segregates to the free Fe surface [1], the model must also include an overlayer of As. In first principle calculations of Fe on GaAs(001) it has been shown if kinetically possible, Fe will substitute for Ga independent of Ga-Ga or As-As terminations at the surface [2]. In fitting Fe K-edge EXAFS data, there is insufficient difference in their scattering amplitudes and phase shifts to distinguish Ga from As. Indeed it is a challenge, in small to moderate concentration, to distinguish either species from Fe. However, for lower coverage films, the presence of these substrate atoms must be considered when fitting.

The idealized structural model for fitting is that of a thin Fe film with infinite smooth sheets capped above by an overlayer of arsenic and below by an underlayer of gallium. Coordination numbers for the first and second nearest-neighbour shells (containing both film and substrate atoms) of the average iron atom were calculated as appropriate to each finite film thickness [3]. Since the model would result in equal amounts of Ga and As in the average iron environment, and in order to simplify the alloy calculation, germanium was used to represent both gallium and arsenic as justified in Appendix C. This, with the exception of the Ge approximation, is similar to the theoretical treatment given in [2], where Ga-diffusion and As-capping were considered. With increasing film thickness, the influence of the substrate atoms decreases. For 9 monolayers and thicker, the influence of the Ga and As atoms became insignificant - fitting with a pure-Fe model gave comparable results. Deviations from the ideal model with infinite smooth sheets are likely to manifest in the form of finite sheets and surface roughness. If less than 1 monolayer of arsenic migrates to the surface, then the capped model overestimates the concentration of As atoms in the EXAFS shells. The physical manifestation of all three of these deviations from the model would be reductions in co-ordination. In the fitting it was decided to use the model and the film thickness to fix the coordination numbers. S_0^2 was then treated as a scaling parameter which would be reduced, instead of N, if the film size, roughness or arsenic overlayers were not as assumed in the model.

Fit results are summarized in figures 5.1 and 5.2. Parameters allowed to vary during the fits were: S_0^2; distances, R_i; mean-square relative displacements, σ_i^2 ; and ΔE_0 to compensate for differences between the Fermi level calculated in the model and the zero of the k-space scale. The distances and mean-square relative displacements were constrained to be the same for both the iron and impurity atoms. No difficulties were encountered in fitting that would have mandated a splitting of these two parameters into separate, independent values. Coordination numbers N_i were fixed according to the capped-film model for all but the thinnest film, and varied with the nominal film thickness.

In all of the iron samples the edge energy, E_0, was consistent with the value obtained from the iron foil fit. There was no chemical shift observed between the films and the iron foil, and the iron foil ΔE_0 was used in the fitting of single-scattering paths in the iron films. For

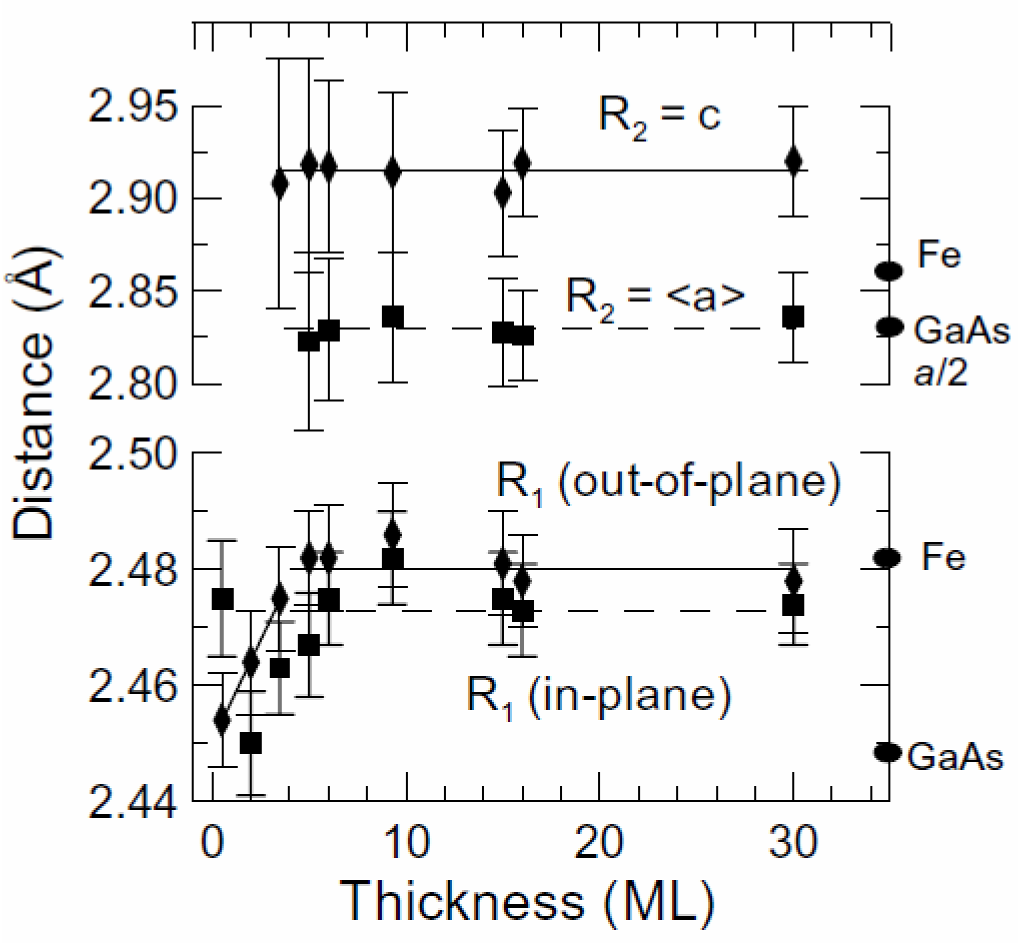

Figure 5.1: Fit results for first (R_1) and second (R_2) nearest neighbour distances for Fe films. Solid lines indicate trends for out-of-plane results while dashed lines are for in-plane fit results. For in-plane R_1 values, the dashed line represents the average excluding the 9.3 monolayers data which was taken with a different substrate orientation (010) than the other thicknesses (110). Bulk iron and gallium arsenide values for first and second near neighbour distances are also given for comparison.

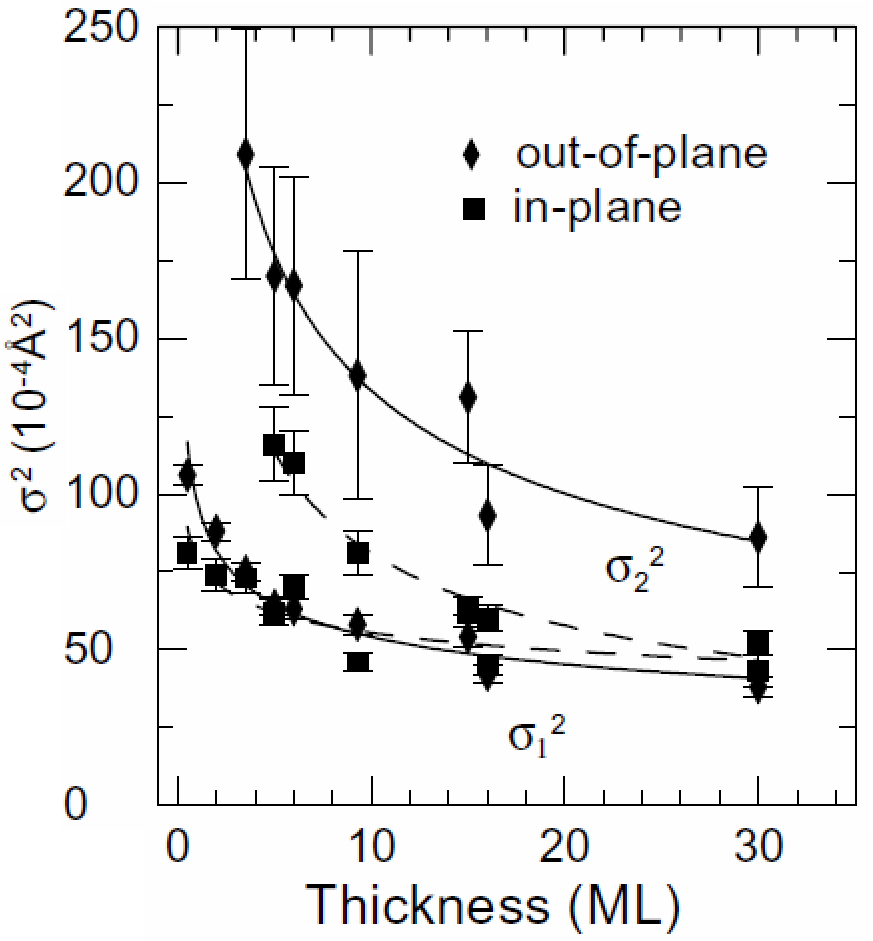

Figure 5.2: Fit results for first (σ_1^2) and second (σ_1^2) nearest neighbour mean-square-relative-displacements for Fe films.

Table 5.1: Theoretical coordination numbers for bcc infinite iron films of specified thicknesses. The N_1^{in} and N_2^{in} were calculated for polarization vector along the $\langle 110 \rangle$ direction.

ML	N_1^{in}	N_1^{out}	N_2^{in}	N_2^{out}
0.5	-	-	2.00	-
2	2.00	4.00	4.00	-
3.5	2.85	5.71	4.00	0.86
5	3.20	6.40	4.00	1.20
6	3.33	6.67	4.00	1.33
9	3.56	7.11	4.00	1.56
9.3	3.58	7.17	4.00	1.57
14	3.71	7.43	4.00	1.71
15	3.73	7.47	4.00	1.73
16	3.75	7.50	4.00	1.75
24	3.83	7.67	4.00	1.83
26	3.85	7.69	4.00	1.85
30	3.87	7.73	4.00	1.87
38.5	3.90	7.79	4.00	1.90
Bulk	4.00	8.00	4.00	2.00

the multiple-scattering paths the ΔE_0 were not fixed in order to allow for compensation in discrepancies in bond angles between the theoretical model and the actual values. However, the values did not deviate significantly from the iron foil fit values. For the palladium films a similar procedure was used, with the exception that for the Pd-Fe and Fe-Pd bonds the ΔE_0 was allowed to change to account for the additional phase shift arising from possible error in theoretical calculations of the muffin-tin potential in the boundary region. The ΔE_0 values obtained from the fit were comparable to the values obtained from the fits to the iron and palladium foil , and did not indicate an additional phase shift significant enough to affect the determination of the bond lengths.

The error bars were determined as follows. Once the best fit was obtained, all the fitting parameters were fixed, except for the one of interest. This parameter was varied from its best fit value until the χ^2 was twice that of the best fit value. The difference between the best fit value of the fitting parameter and its $2\chi^2$ value was taken as an error.

Table 5.1 provides the theoretical coordination numbers calculated for the perfectly flat infinite iron films of measured thicknesses for $E_{\|}$ and $E_{\perp}$ polarizations. The S_0^2 values remained in the range of 0.6-0.7 for the films 5 monolayers and thicker, reduced relative to 0.75(2) obtained for the foil, but still indicating large film areas consistent with layer growth.

For the 3.5 monolayers and 2 monolayers samples, S_0^2 decreased to 0.51(2) and 0.48(2), respectively, which can be attributed to finite island size effects on co-ordination. This reduction can be used to give a rough estimate of our island size. First-shell coordination numbers scale as ((thickness - 1)/thickness in monolayers) for an uncapped infinite sheet. A similar scaling behaviour can be applied for the in-plane dimensions. Since S_0^2 and N_1 are directly correlated, by considering the square root of the ratio of the S_0^2 values for thin (0.5) and thicker films (0.65 on average), and already considering finite out-of-plane thickness when fitting, we obtain a rough estimate of 4 unit cells on a side, or approximately 120 Å^2 island area. This is a lower limit that assumes square islands and does not consider anisotropy in island shape, nor roughness.

For the 0.5 and 2 monolayers films, no second nearest neighbour could be extracted from the data. This resulted in a strong dependency on model and on relative amounts of Fe and Ge: the Ge level is comparable to iron at 2 monolayers, and exceeds the Fe content at 0.5 monolayers. For 2 monolayers, a reasonable fit could still be obtained with the capped film model albeit with average nearest neighbour coordination number reduced to 2/3 the bulk value, based on the reduction in S_0^2. For 0.5 monolayers, S_0^2 was fixed at 0.65 (transferred from the thicker films) and the relative amounts of Fe and substrate atoms allowed to vary. Doing so for the out-of-plane orientation favoured the substrate atoms roughly 6 to 1.5 over the Fe, with summed coordination of ≈ 7.5 atoms in the first shell. Fitting with no Fe in the shell gave similar results for R_1 and σ_1^2, but with $N_1 \approx 8$. The in-plane 0.5 monolayers data could not be fit with only substrate atoms in the shell. Allowing the amounts of Fe and substrate atoms to vary resulted in only Fe, with $N_1 \approx 8$ atoms. While the absence of substrate atoms in this shell is puzzling, two possible explanations exist as to why this may be so: (1) the reconstructed surface [4] possesses channels that would permit linear arrangements of iron atoms at low coverage along the $\langle 110 \rangle$ and $\langle \bar{1}10 \rangle$ directions; and (2) the slice projections along $\langle 1\bar{1}0 \rangle$ calculated in [2] indicate iron as the nearest in-plane neighbour with the nearest substrate atom neighbours being two atoms oriented orthogonal to the iron neighbour (and hence would have a negligible contribution to an in-plane-polarized XAFS measurement). However, this does not resolve why ≈ 8 nearest neighbours were observed for the out-of-plane results.

For 5 monolayers and thicker samples, up to 38.5 monolayers, in both polarizations, both first and second nearest neighbour distances show little variation. The R-values plotted in figure 5.1 have had offset corrections of $\approx +0.01$ Å applied, based on fits to the iron foil

Table 5.2: Fit results for $E_{\parallel}$ and $E_{\perp}$ Fe K-edge for selected thicknesses. The layer thicknesses are defined to within an error of ±0.05-0.06 monolayers. Notice that for samples with 9, 24 and 38.5 monolayers no in-plane measurements were done.

ML	R_1^{in}, Å	$\sigma^2_{1,in}$, Å^2	R_1^{out}, Å	$\sigma^2_{1,out}$, Å^2	R_2^{in}, Å	$\sigma^2_{2,in}$, Å^2	R_2^{out}, Å	$\sigma^2_{2,out}$, Å^2	S_0^2
0.5	2.475(9)	0.0080(4)	2.454(9)	0.0105(3)	-	-	-	-	.65(2)
2	2.450(9)	0.0074(4)	2.463(8)	0.0087(3)	-	-	-	-	.48(2)
3.5	2.462(7)	0.0073(4)	2.475(7)	0.0075(3)	-	-	-	-	.51(2)
5	2.467(9)	0.0063(3)	2.482(5)	0.0065(3)	2.824(50)	0.0117(12)	2.917(70)	0.0170(30)	.63(2)
6	2.475(7)	0.0071(3)	2.482(6)	0.0064(2)	2.839(35)	0.0112(12)	2.916(40)	0.0167(30)	.61(2)
9	-	-	2.479(8)	0.0057(2)	-	-	2.908(15)	0.0117(23)	.63(2)
9.3	2.482(5)	0.0046(2)	2.485(6)	0.0056(2)	2.834(30)	0.0080(6)	2.915(40)	0.0133(38)	.65(2)
14	2.474(8)	0.0055(2)	2.480(5)	0.0052(2)	2.826(9)	0.0067(3)	2.917(13)	0.0116(17)	.65(2)
15	2.475(5)	0.0063(2)	2.481(7)	0.0052(2)	2.828(30)	0.0066(5)	2.900(35)	0.0128(22)	.66(2)
16	2.473(5)	0.0060(2)	2.478(6)	0.0044(2)	2.825(25)	0.0061(3)	2.920(35)	0.0090(14)	.64(2)
24	-	-	2.481(4)	0.0049(3)	-	-	2.989(18)	0.0081(9)	.69(2)
26	2.472(4)	0.0048(2)	2.481(5)	0.0046(2)	2.831(9)	0.0061(3)	2.904(16)	0.0089(10)	.67(2)
30	2.472(4)	0.0045(3)	2.478(6)	0.0039(2)	2.838(25)	0.0051(2)	2.921(35)	0.0086(15)	.68(2)
38.5	-	-	2.483(4)	0.0058(2)	-	-	2.901(16)	0.0076(9)	.67(2)

standard. The nearest neighbour distances obtained from out-of-plane measurements for 5 monolayers and higher, $R_1^{out} = 2.481(4)$ Å, are comparable to that for bcc iron (2.4824 Å). The in-plane nearest neighbour results for films measured along $\langle 110 \rangle$ (i.e. not the 9.3 monolayer data which was measured along $\langle 010 \rangle$) are consistently lower than the out-of-plane results by 0.008 Å on average ($R_1^{in} = 2.473(4)$ Å - within error individually, but noticeably lower for the average). Both the c-axis and average a-axis deviate from bcc Fe, as noted for films near 10 monolayers [5], and are indicative of the distortion to a body-centered tetragonal structure (or pseudotetragonal for measurements along $\langle 010 \rangle$ since only an average in-plane lattice constant is determined).

In considering films from 5 monolayers to 38.5 monolayers, the average out-of-plane lattice constant, c_{film}, was found to be 2.915(17) Å, and the average in-plane value, a_{film}, to be 2.830(14) Å. The in-plane value is in good agreement with lattice-matching to the GaAs substrate ($a/2 = 2.827$ Å). This results in a mean value for the c/a ratio of 1.030(8) with a $\Delta c = c_{film} - c_{foil}$ of 0.049(17) Å and $\Delta a = a_{film} - a_{foil}$ of -0.037(14) Å. Macroscopic elasticity theory [5, 6, 7, 8] relates the in-plane and out-of-plane stresses: $\frac{\Delta c}{\Delta a} = -\frac{2c_{12}}{c_{11}}$, and, using the known elastic constants c_{ij} for iron [9, 10], this ratio should be -1.212. The average results for the films give -1.3(7), in good agreement, even with the large error. The absence of a thickness dependence to the distortion for films thicker than 4 monolayers also allays previous concerns [5] regarding perpendicular magnetic anisotropy measurements [1], where a thickness dependence to the strain would have necessitated a reinterpretation of the results.

The first principles calculation of Mirbt et al [1] for 5 monolayers with a 1 monolayer arsenic cap yielded a theoretical c/a ratio of 1.03 in agreement with the experimental result. In addition they predicted a distortion in-plane to give a contraction along $\langle 110 \rangle$ of 1.83 % and an expansion along $\langle \bar{1}10 \rangle$ of 0.51 %. This predicted in-plane distortion would cause a splitting of the eight nearest-neighbour distances (Figure 4.13(a)) into four atoms at 2.445 Å (i.e. the atoms indicated in (Figure 4.13(c))) and four at 2.483 Å, with an average of 2.464 Å for the eight atoms. With the X-ray polarization perpendicular to the plane of the substrate, contributions from all eight atoms are present and the average distance is extracted. With the polarization in the plane along $\langle 110 \rangle$, the examined four nearest neighbour atoms are predicted to be contracted. A contraction along $\langle \bar{1}10 \rangle$ is observed in our work for our 5 monolayers sample: $R_1^{in} = 2.467(9)$ Å and $R_1^{out} = 2.482(8)$ Å, with R_1^{out} representing still the average over all eight nearest neighbours. The spatial resolution of EXAFS [11] is limited by the finite range of data by the relation $\Delta k \Delta R = \pi/2$. With a k-space range, $\Delta k \leq 12$ Å^{-1}, the minimum resolvable separation of two bond lengths is 0.13 Å. Both in-plane and out-of-plane experimental values are approximately 0.02 Å larger that their corresponding theoretical values, but do follow the theoretical trend. This may be an artifact of fitting since the differences for the 6 monolayers sample are less noticeable. Additional XAFS measurements with the X-ray polarization vector in the surface along $\langle\bar{1}10\rangle$ are necessary to confirm the in-plane distortion in this system at low coverage, complimenting work done on thicker films prepared on the As-rich 2×4 GaAs surface [12] in exploring uniaxial magnetic anisotropy in the Fe/GaAs system. Such study was later conducted by Gordon and Crozier [13] and the in-plane distortion was, in fact, confirmed.

For thicknesses below 5 monolayers, in the regime of island growth, a decrease in nearest-neighbour distance is observed for out-of-plane measurements, almost linearly with decreasing thickness (Figure 5.1). At 0.5 monolayers, the distance approaches that for the Ga-As bond length in the substrate (2.448 Å). If the Fe were occupying tetrahedral vacancies in the upper surface of the GaAs substrate, one could expect this distance, but with coordination number of 4, not 7.5-8 as noted in fitting the out-of-plane data. The in-plane result suggests only Fe atoms present as nearest neighbours in-plane, but with a larger distance, at 2.475(9) Å, than out-of-plane. The Fe cannot, therefore, be merely substituting into the lattice, nor nucleating a bcc-like phase.

These results indicate a reaction with the Ga-rich surface to form a separate phase at the surface. A separate phase forming at the surface has been suggested by the first principles calculations of Mirbt et al [2]. In their work, for a 1 monolayer film, the nearest-neighbour interactions for an out-of-plane polarization would contain only contributions from the substrate, with the Fe-As and Fe-Ga distances calculated to be 2.32 Å and 2.51 Å, respectively. Our measured value of the average, at 2.454(8) Å, is about 0.04 Å larger than calculation suggests (perhaps due to the use of the Ga-rich 4×6 reconstructed surface), but is comparable. The nearest neighbour in-plane [2] is exclusively iron and estimated to be approximately 10 % further away than the Fe-Ga distance (i.e. about 2.75 Å) which is considerably larger than what is observed for the 0.5 monolayers sample in this work. The polarization dependence (substrate atoms out-of-plane, iron in-plane), however, is consistent. This may not reflect the true nature of the interface for a thicker film since the cessation of growth at such a low coverage, potentially before stable islands have formed, may lead to increased surface reaction.

The mean-square-relative-displacements increase with decreasing thickness, consistent with an increasing ratio of surface to interior atoms (fewer atoms bound inside the film) and may also reflect the increasing influence of substrate atoms within the iron film. Values for the second shell atoms in the out-of-plane polarization plotted in figure 5.2 are considerably larger than the nearest-neighbour, in-plane or foil values. This may be due to increased disorder or (surface) roughness in the out-of-plane direction. It may also be due to the strained nature of the film itself. For both polarizations, the nearest-neighbour interactions are largely in-plane, since the nearest-neighbour in a bcc or bct structure is located approximately 36° above the plane (the angle between the $\langle 111 \rangle$ and $\langle 110 \rangle$ directions). Next-nearest neighbour interactions for in-plane are also (entirely) in-plane, but, for the out-of-plane measurements, the next-nearest neighbour is 90° above the plane entirely out of plane. The out-of-plane direction is the direction of response to the in-plane stress. It is not unreasonable to expect a larger dynamic contribution to the mean-square-relative-displacement in this case, but a temperature-dependent study would be required to confirm this.

5.2 Pd on Fe

5.2.1 Models

Bulk palladium has a fcc structure with $a_{fcc} = 3.89$ Å. The shortest radial distance between two atoms in such a structure is half-way along the face diagonal and is equal to $\frac{1}{\sqrt{2}} a_{fcc} = 2.75$ Å. The nearest neighbour coordination number for this bond for the bulk palladium is 12: 4 face-centered atoms in (100), (010) and (001) planes. This distance is 2.91 % shorter than the in-plane lattice parameter for bct iron, which is known to be 2.83 Å from the iron analysis described earlier. A starting assumption can be made that palladium during its growth on bct iron will change from fcc to face-centered tetragonal via expansion of this bond in the (001) plane and, consequently (assuming constant unit cell volume model), contraction out-of-plane (in both (100) and (010) planes) to match the underlying iron film.

Since palladium is grown on bct iron, it is convenient to think about the fcc structure of palladium as a bct structure with $a_{bct} = \frac{1}{\sqrt{2}} a_{fcc} = 2.75$ Å and $c_{bct} = a_{fcc} = 3.89$ Å. In this representation, the $\langle 001 \rangle$ direction of both the original fcc and bct structures is the same, while the bct unit cell is rotated 45° around the $\langle 001 \rangle$ direction with respect to the fcc unit cell: the $\langle 110 \rangle$ direction of the fcc is the $\langle 100 \rangle$ direction of the bct and the $\langle \bar{1}10 \rangle$ is $\langle 010 \rangle$

(see Figure 4.13). This bct representation allows one to apply the same formalism as in the description of the iron bct structure, reversing to the natural palladium fcc structure after the analysis is done. In the discussion below, the subscript when referring to bct palladium representation lattice parameter is dropped for clarity.

In such a bct structural representation of palladium, as with iron, the $E_{\perp}$ data for the first radial distance, R_1^{out}, contains contributions from the atoms in (110) and ($\bar{1}$10) planes, a total of 8 for the bulk palladium. The second radial distance, R_2^{out}, is the c-axis distance and has a coordination number of 2. These distances differ significantly (in the ideal model, assuming a perfect fit to iron in-plane and constant unit cell volume model $R_1^{out} = 2.72$ Å and $R_2^{out} \equiv c = 3.68$ Å) and do not pose a problem in fitting. The $E_{\parallel}$ data with polarization along $\langle 110 \rangle$ direction, however, has 4 atoms in ($\bar{1}$10) plane at ideal distance $R_1^{in} = R_1^{out}$ and 4 atoms in (001) plane at ideal a-axis distance $R_2^{in} = 2.83$ Å (the 4 atoms in (110) plane at the ideal distance R_1^{in} are at 90° with respect to the polarization vector and, consequently, do no contribute to the signal). Even if palladium matches underlying iron ideally, $\Delta R = R_2^{in} - R_1^{in}$ is equal to 0.11 Å, and, given the k-range of the data of about 12 Å^{-1}, is beyond the EXAFS spatial resolution. Moreover, it is possible that palladium does not match the underlying iron ideally by not expanding as much as needed, and ΔR is even less. As a result, the atoms at R_1^{in} and R_2^{in} have to be treated as atoms at some average distance.

5.2.2 Fitting

The 1 monolayer of palladium grown on 9 monolayers of untreated iron was different from other samples and was modelled differently. This is because the iron film was not sputtered and annealed before the palladium deposition. The resulting iron film had increased surface roughness compared to the treated samples. The radial distances are in agreement with a bct structure of Fe grown on GaAs-(4×6). However, for an ideal perfectly flat 9 monolayers of Fe the theoretical first nearest neighbour coordination number N_1 is 7.11. Experimentally it was determined to be $N_1 = 6.7(1.0)$ after correction for S_0^2 listed in table 5.2. The second nearest neighbour $N_2 = 1.56$ theoretically versus 1.5(2) experimentally. From these values Fe surface roughness can be estimated to be ≈ 2 monolayers. In addition, the arsenic that is known to float on top of the film during iron growth was not removed by the sputtering. Although, no As could be detected in fitting the Fe data itself, in modelling the palladium environment it was necessary to introduce As atoms since they were in immediate proximity to the palladium at comparable concentrations.

In modelling of the palladium grown on the treated iron films (1 monolayer on 26 monolayers iron, and 3.5+3.5 monolayer on 38.5 monolayers iron) smooth iron surface and layer-by-layer palladium growth were assumed as a model for obtaining theoretical backscattering amplitudes and phase shifts. Below, for shortness the samples are referred to as 1Pd/9Fe, 1Pd/26Fe, 3.5Pd/38.5Fe and 7Pd/38.5Fe.

Unlike for the iron films, for fitting the palladium the S_0^2 scaling factor was fixed to the value of 0.69(2) obtained for palladium foil and the coordination numbers were allowed to vary. The rest of the fitting parameters were the same as in fitting iron films: bond lengths R_i, mean square relative displacements σ_i^2 and ΔE_0. Consequently, the changes in coordination numbers manifested structural deviations from the assumed models, and combined with the bond lengths allowed to speculate with regard to the actual structure of the films.

Table 5.3 summarizes the fit results for the palladium films grown on iron. The R-values in table 5.3 have had offset corrections of $\approx +0.01$ Å applied, based on fits to the palladium foil standard. The first Pd-Fe radial distance, $R_{1,Pd-Fe}$, was observed in all of the fits, except for in-plane polarization for the 7Pd/38.5Fe sample, and is equal to 2.60(2) Å for all the samples within the experimental error. For the 1Pd/9Fe, 1Pd/26Fe and 3.5Pd/38.5Fe samples, the out-of-plane σ_{out}^2 for this bond is slightly larger than the in-plane σ_{in}^2 similar to the tendency exhibited by the mean square relative displacement for the iron films. For the 7Pd/38.5Fe sample, the σ_{out}^2 remains similar. This indicates that no structural disorder with respect to the Pd-Fe bond was induced by the deposition of the additional 3.5 monolayers of palladium. In addition, for the 1Pd/9Fe sample a Pd-As radial distance had to be included in the fit. It was found to be equal to 2.60(2) Å, same as the Pd-Fe distance which is reasonable, considering that Fe and As have similar atomic radii. The coordination number is relatively small: $N_{1,Pd-As}^{out}$=0.5(1), indicating at least 0.5 monolayers of As floated to the surface of Pd during the growth. There may be additional As present on those patches of the Fe surface not covered by Pd. However, As cannot be detected in the Fe K-edge fits for 9 monolayer thickness. The first Pd-Pd radial distance, $R_{1,Pd-Pd}$, extracted from the fits decreases slightly with sample thickness for out-of-plane polarization, while for in-plane polarization the trend is reversed. For the 3.5Pd/38.5Fe and 7Pd/38.5Fe samples the second Pd-Pd distances were also obtained.

It is important to acknowledge that out-of-plane polarization data for both 1Pd/9Fe and

Table 5.3: Fit results for $E_{\parallel}$ and $E_{\perp}$ Pd K-edge. The layer thicknesses are defined to within an error of ±0.05-0.06 monolayers.

ML	$N_{1,Fe}$	$R_{1,Fe}$, Å	$\sigma^2_{1,Fe}$, Å^2	$N_{1,Pd}$	$R_{1,Pd}$, Å	$\sigma^2_{1,Pd}$, Å^2	$N_{2,Pd}$	$R_{2,Pd}$, Å	$\sigma^2_{2,Pd}$, Å^2
1 Pd/9 Fe, $E_{\perp}$	2.33(.3)	2.602(20)	0.0058(3)	2.30(.3)	2.803(22)	0.0087(9)	-	-	-
1 Pd/26 Fe, $E_{\parallel}$	2.82(.3)	2.601(12)	0.0042(2)	1.21(.2)	2.768(15)	0.0088(7)	-	-	-
1 Pd/26 Fe, $E_{\perp}$	2.81(.3)	2.604(12)	0.0059(3)	.45(.06)	2.785(15)	0.0081(7)	-	-	-
3.5 Pd/38.5 Fe, $E_{\parallel}$	0.91(.1)	2.615(9)	0.0061(3)	5.91(.4)	2.779(16)	0.0104(16)	5.91(.5)	3.872(30)	0.0119(25)
3.5 Pd/38.5 Fe, $E_{\perp}$	1.74(.2)	2.617(10)	0.0071(3)	5.12(.4)	2.771(14)	0.0086(4)	0.82(.1)	3.813(32)	0.0117(28)
7 Pd/38.5 Fe, $E_{\parallel}$	-	-	-	7.04(.5)	2.798(16)	0.0076(3)	1.87(.2)	3.961(32)	0.0093(17)
7 Pd/38.5 Fe, $E_{\perp}$	0.94(.1)	2.612(9)	0.0069(2)	6.23(.5)	2.747(12)	0.0058(3)	1.31(.2)	3.737(31)	0.0076(16)

1Pd/26Fe samples have $R_{1,Pd-Pd}$ distance present. If the 1 monolayer of Pd were perfectly flat there would be no out-of-plane Pd-Pd distance. Its presence indicates formation of either islands or alloy at the Pd/Fe interface at low palladium coverages. The coordination numbers for first Pd-Fe and Pd-Pd bonds support this conclusion. For the palladium grown on the untreated iron film (1Pd/9Fe sample), $N^{out}_{1,Pd-Fe}$ is 2.28(3), while for the treated iron film (1Pd/26Fe) $N^{out}_{1,Pd-Fe}$ is 2.82(3). The Pd-Pd coordination numbers, $N^{out}_{1,Pd-Pd}$ differ dramatically: for the 1Pd/9Fe sample it is again 2.3(3), then for 1Pd/26Fe sample it is just 0.45(2). For an ideal 1 monolayer palladium grown on iron $N^{out}_{1,Pd-Fe}$ would be 4 and $N^{in}_{1,Pd-Fe}$ 2, while $N^{out}_{1,Pd-Pd}$ would be exactly 0. It allows to make a conclusion that palladium grown on untreated iron film has greater tendency to form islands and/or alloys at the surface of the iron. On the other hand, the palladium grown on the treated iron tends to be smoother and while it does form alloy with the underlying iron, it is limited to $\approx 0.5 - 1$ monolayer.

For the 7Pd/38.5Fe sample the first and the second Pd-Pd coordination numbers and respective radial distances indicate that relatively thick palladium tries to match the underlying iron film but does not do it completely, deviating from the ideal model described above. The R_2 distances for in-plane and out-of-plane data become a-distance and c-distance for the fct palladium (3.96(3) Å and 3.75(2) Å, respectively, versus ideal 4.00 Å and 3.67 Å). The ideal coordination number for the first and second shells in the given geometry are: $N^{out}_{1,Pd-Pd}$=6.86, $N^{in}_{1,Pd-Pd}$=7.43 and $N^{out}_{2,Pd-Pd}$=1.43, $N^{in}_{2,Pd-Pd}$=2.0. While the first Pd-Pd out-of-plane radial distance 2.76(2) Å is larger than ideal 2.72 Å, an important observation can be made. The out-of-plane polarization probes all (ideally, 8) corner atoms of the bct unit cell. The in-plane polarization probes 4 atoms located in the $(\bar{1}10)$ plane and 4 atoms located in the (001) plane. As stated earlier, the bond lengths for these two groups of 4 atoms probed by in-plane polarization are different: 2.72 Å and 2.83 Å. But they cannot be resolved with the given EXAFS resolution, and, consequently, the fit gives their averaged value 2.80(2) Å. This value is expected to be larger than the out-of-plane value of 2.76(2) Å. This also explains the relatively high coordination number for this bond which is higher than the theoretical value of 3.42 for just the $(\bar{1}10)$ plane itself for this thickness. The combined theoretical coordination numbers for the $(\bar{1}10)$ and the (001) planes yield 7.43. The observed lower value of 7.04 confirms that in our films there is a relatively small degree of intermixing at the palladium-iron interface.

The 3.5Pd/38.5Fe sample is somewhat a structural mid-point between 1 monolayer and

7 monolayers palladium samples. While the first Pd-Pd bond lengths are similar to that of 7Pd/38.5Fe sample, the second Pd-Pd distances are smaller in-plane and larger out-of plane. The coordination numbers are: $N^{out}_{1,Pd-Pd}$=3.5(4), $N^{in}_{1,Pd-Pd}$=5.9(9) and $N^{out}_{2,Pd-Pd}$=0.8(3). While the first Pd-Pd distance is comparable with the 7Pd/38.5Fe sample distance, the second Pd-Pd distance is shorter in-plane and longer out-of-plane. There could be a few possible explanations. First, is that palladium is transitioning from island to layer-by-layer growth mode with small amount of alloying of $\approx 0.5 - 1$ monolayer, similar to 1Pd/26Fe sample. Second, is that ≈ 1 monolayer of palladium is intermixed with the underlying iron, while the top 2 palladium layers grew layer-by-layer. The distances in this case would be averaged throughout the different growth layers and can result in different values comparing to 7Pd/38.5Fe monolayer sample which is averaged through out relatively thick palladium.

The overall picture of the palladium growth on the bct iron is as follows. During initial growth palladium alloys with underlying iron and the amount of alloying depends on iron surface preparation. For sputtered and annealed iron surface the amount of alloying is $\approx 0.5-1$ monolayer, while for untreated iron surface palladium is forming at least 2 monolayers of alloying and island formation. It is evident that for treated iron surface, somewhere between 1 and 3.5 monolayers palladium undergoes growth mode change and starts growing layer-by-layer. The exact thickness is hard to define from the available data. After that, to at least 7 monolayers, palladium grows layer-by-layer as the fct structure, attempting to match the underlying iron with lattice parameters $a = 3.96(3)$ Å and $c = 3.75(3)$. Therefore, palladium is expanded in-plane and contracted out-of-plane with $c/a = 0.946$.

It is worth mentioning that measurements taken at the Fe K-edge on the 3.5Pd/38.5Fe film with the angle of incidence above the critical angle revealed that iron did not change its bct structure after palladium deposition. This can serve as an additional hint that the amount of intermixing between Fe and Pd at the interface is small.

This overall picture seems to be consistent with some of the results on the Pd/Fe system available in the literature. For example, in the presented picture the Pd does not match Fe perfectly right at the interface, at very low coverages. Similar results were observed in [14] using Transmission Electron Microscopy (TEM): the relaxation of the Pd grown on bct Fe starts at very small coverages and is achieved via misfit dislocation. The averaged radial distances obtained using XAFS, given that they are somewhat relaxed comparing to ideal matching structure, can, in principle, be a result of such misfit dislocations. However, they cannot be observed directly with XAFS. Since in this study and in the one cited above the substrate preparation and MBE growth procedures were similar, misfit dislocations can be the case.

In another work, combining both first principle calculations and X-ray diffraction experiment, it was found that palladium grown on Fe(001) single crystal is expanded in-plane and contracted out-of-plane with $c/a = 0.89$ [15]. The result presented in this thesis is in general agreement with this conclusion, although the distortion observed was not as pronounced. It is also stated that Pd-Fe distances are, indeed, less than the Pd-Pd distances. This is in correspondence with the results given in this thesis for all thicknesses measured.

5.3 Fe on Pd

Modelling the iron on top of palladium included the results of the analysis of palladium film. The underlying palladium was assumed to be fct distorted with a-distance and c-distance given above. Table 5.4 shows the fit results.

Analysis of the upper 4 monolayers Fe, both $E_{\parallel}$ and $E_{\perp}$, revealed Pd to be present in greater amounts than the traces of Fe at the 38.5 monolayers Fe/Pd interface. Coordination numbers yield around 1.5-2.0 monolayers of Fe-Pd alloy consistent with [16]. Also, the 10 iron monolayers out-of-plane data shows traces of Pd, supporting a large intermixing model for the second Pd/Fe interface. The intermixing does not seem to exhibit any particular order which is similar to the result obtained for the lower Pd/Fe interface. It is interesting that the upper Fe-Pd distance is slightly but consistently larger then Pd-Fe distance obtained for Pd K-edge and also slightly increases with the thickness. It can be a result of an error in backscattering phase shift calculations for palladium. The fact that the palladium foil fit is generally worse than for the iron foil could be indirect supporting evidence to this statement.

The first and the second Fe-Fe distances for 4 and 10 monolayers show that iron has retained the bct structure with $a = 2.83(2)$ Å and $c = 2.92(3)$ Å which is very close to the Fe grown on GaAs(001)-(4×6) substrate directly. That means that Fe on the fct palladium can be grown as a bct structure at least to 10 monolayers thick, despite the intermixing at the boundary. R_2^{out} for 4 and 10 monolayers iron are slightly larger than for bottom iron grown on GaAs(001). This can be seen as supportive evidence of the larger amount of the iron-palladium intermixing at the boundary compared to the lower interface. Analysis of $E_{\perp}$ for 10 monolayers of Fe, is in agreement with the 4 monolayers data, showing the same

Table 5.4: Fit results for $E_{\parallel}$ and $E_{\perp}$ Fe K-edge. The layer thicknesses are defined to within an error of ±0.05-0.06 monolayers.

ML	$N_{1,Fe}$	$R_{1,Fe}$, Å	$\sigma^2_{1,Fe}$, Å^2	$N_{1,Pd}$	$R_{1,Pd}$, Å	$\sigma^2_{1,Pd}$, Å^2	$N_{2,Fe}$	$R_{2,Fe}$, Å	$\sigma^2_{2,Fe}$, Å^2
4 Fe/7 Pd, $E_{\perp}$	4.67(.3)	2.481(12)	0.0043(2)	2.38(.3)	2.691(16)	0.0079(10)	0.89(.1)	2.931(24)	0.0091(15)
4 Fe/7 Pd, $E_{\parallel}$	1.75(.2)	2.471(10)	0.0039(2)	2.62(.3)	2.700(15)	0.0093(9)	2.51(.2)	2.838(20)	0.0084(12)
10 Fe/7 Pd, $E_{\perp}$	6.76(.5)	2.492(15)	0.0059(3)	0.82(.1)	2.741(30)	0.0121(19)	1.21(.1)	2.924(32)	0.0151(27)

tetragonal distortion and the presence of a comparable amount of Pd.

An XRD study of Fe grown on single crystal Pd(001) shows no alloying occurring at room temperature at the Fe/Pd interface [17]. This seems to be in contradiction with our result of alloy formation on both Pd/Fe and Fe/Pd interfaces. However, this difference can be explained by different sample preparation techniques: the deposition of Fe on a single crystal Pd(001) whose surface was annealed in [17] versus deposition of Fe on fct distorted Pd that did not undergo annealing. The surface roughness of our MBE-grown untreated sample is expected to be greater than the roughness of the single crystal annealed surface, and leads to greater degree of alloying. Also, the same study reports that alloying starts to occur at mild annealing temperatures of 330 K and becomes more pronounced at 400 K. The alloy that is formed after the annealing is also a disordered $Fe_{50}Pd_{50}$. In this thesis a disordered alloy was observed, but the exact composition could not be determined.

Chapter 6

Conclusion

In this brief chapter the main results of this thesis are summarized, followed by propositions regarding possible future studies to facilitate better understanding of the Fe/Pd/Fe/GaAs(001)-4×6 ultrathin films structure.

The polarization-dependent EXAFS was used to study ultrathin Fe/Pd/Fe/GaAs(001)-4×6 films grown by MBE *in situ*. The findings are summarized in figure 6.1.

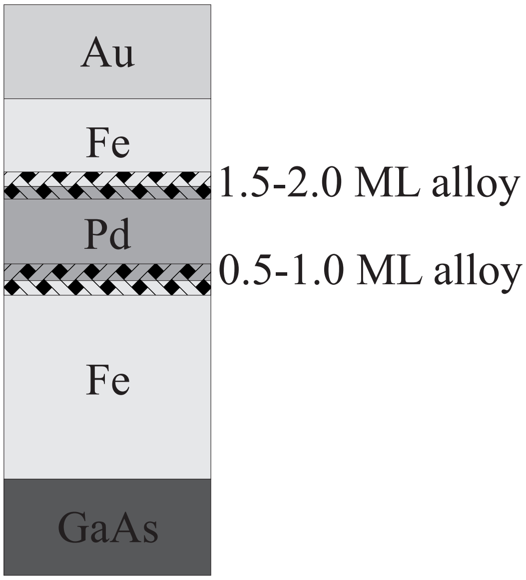

Figure 6.1: Overall picture of the structure of Fe/Pd/Fe/GaAs(001) ultrathin films. The capping Au layer is shown.

The structural evolution of the Fe grown on GaAs substrate was established via consistent analysis of the iron films ranging in thicknesses from 0.5 monolayers up to 38.5 monolayers. It has been shown that iron exhibits tetragonal distortion from its body-centered cubic bulk structure by contracting in-plane and expanding out-of-plane. The in-plane and out-of-plane lattice constants were found to be 2.830(14) Å and 2.915(17) Å, respectively, yielding a c/a ratio of 1.030(8). The in-plane lattice parameter is in close agreement to the GaAs $a_{GaAs}/2 = 2.827$ Å lattice parameter. Formation of the iron islands on the GaAs substrate was observed for thicknesses below 5 monolayers. Around 5 monolayers a transition to layer-by-layer growth mode was established, which persists up to the 38.5 monolayers (the thickest iron film measured). No visible lattice relaxation was found even for that thickness. The slight mismatch between the first bond lengths for the in-plane and out-of-plane data allowed one to speculate about possible in-plane structural anisotropy. This prompted Gordon and Crozier to perform a separate set of experiments that, indeed, confirmed the existence of such in-plane anisotropy ($R_1^{\langle\bar{1}10\rangle}/R_1^{\langle 110\rangle}$ ≈1.008 %).

The palladium films grown on the iron buffer were shown to be also tetragonally distorted from its natural face-centered cubic bulk structure. However, the distortion was of the opposite nature to that of the iron which has an in-plane contraction and out-of-plane expansion. This is within the model where the palladium face-diagonal fcc bond ($a_{Fe}/\sqrt{2} =$ 2.751 Å) expands to match the underlying iron. The in-plane and out-of-plane lattice parameters for the palladium were found to be 3.96 Å and 3.75 Å ($c/a = 1.056$), meaning that palladium does not match the iron exactly ($a_{Fe} = 2.83$ Å versus $a_{Pd}/\sqrt{2} = 2.80$ Å). Nonetheless, the distortion is significant and is retained up to 7 monolayers (the thickest palladium film measured). It is also worth mentioning that the obtained lattice parameters for palladium film are in agreement with the constant unit cell volume model within the experimental error.

The iron grown on palladium exhibits tetragonal distortion similar to the distortion of the iron grown directly on the GaAs(001)-4×6 surface. However, the lattice parameters obtained are slightly larger, both in-plane and out-of-plane: 2.84 Å and 2.93 Å, respectively. The larger lattice parameters can be attributed to the expansion of the iron lattice due to intermixing with palladium.

It was also established that palladium intermixes with iron at the lower interface throughout the thickness of about 0.5-1 monolayer. The upper interface intermixing is larger and estimated to be of the order of 1.5-2 monolayers. No ordered structure could be proposed from the results which is in agreement with the fact that an ordered FePd fcc structure (L01 alloy) forms at ≈ 920 K, while the investigated samples were studied at room temperature.

The EXAFS spatial resolution is limited due to finite k-range of the available data. The high-k cut-off is based on the signal-to-noise ratio which declines towards higher k. Because of that it was impossible to resolve the two close Pd-Pd bonds that are anticipated to be present in the in-plane polarization data. It will be beneficial to conduct a set of experiments at low temperatures. This will allow a reduction in the mean square relative displacement reduction factor, enhancing the signal-to-noise ratio in the high-k region and, thus, increasing the EXAFS spatial resolution.

Additional studies at low palladium on iron and iron on palladium coverages are required to establish the exact nature of the intermixing at the interfaces. Such techniques as Transmission Electron Microscopy can also be employed to help resolve the question.

Appendix A

Electric Field Amplitudes in a Layered Sample

The calculation of the electric field amplitudes presented in this appendix follows that given by Jiang [1, 2].

A schematic view of a layered sample with the electric field distribution within it is shown in Fig. (A.1). The substrate is depicted as layer $m = 0$ and subsequent layers have increasing indices in the direction of the sample growth ($-z$). In the shown case, the vacuum is denoted by $m = 3$, with E_3 and E_3^R being the incident and the reflected electric field components, respectively. Polarization of the electric field is taken to be in-plane of the sample, thus pointing out of the page.

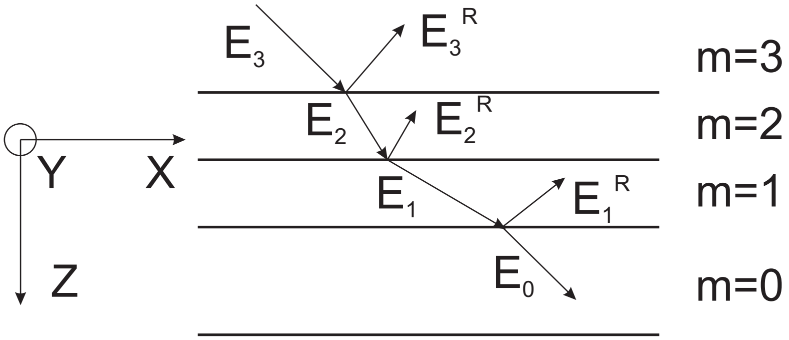

Figure A.1: A schematic view of a layered sample with the electric field distribution within it. $m = 0$ and $m = 3$ denote the substrate and the vacuum above the sample, respectively. The electric field is taken to have in-plane (out of the page) polarization.

If we consider a solid, in the simplest model, as a system of independent neutral atoms, then the effect of the plane monochromatic electromagnetic wave (angular frequency ω) on it is described by a complex dielectric constant, $\epsilon(\omega)$. In terms of the atomic scattering factor it is given by

$$\epsilon(\omega) = 1 - \frac{4\pi N e^2}{m_e \omega^2}(f_0 + f' + i f''), \tag{A.1}$$

where N is the number of atoms per unit volume, f_0 is the atomic number in the forward scattering case, and f' and f'' are real and imaginary parts of the anomalous scattering correction, respectively. Considering that the index of refraction $n = \sqrt{\epsilon(\omega)}$ and taking into account the second term in A.1 is of the order of magnitude 10^{-5} we can rewrite:

$$n = 1 - \delta - i\beta, \tag{A.2}$$

where

$$\delta = \frac{N_A}{2\pi}\frac{e^2}{m_e c^2}\frac{\rho}{M}\lambda^2(f_0 + f'), \tag{A.3}$$

and

$$\beta = \frac{N_A}{2\pi}\frac{e^2}{m_e c^2}\frac{\rho}{M}\lambda^2(f''). \tag{A.4}$$

In the last two equations the substitutions $N = N_A\rho/M$ and $\omega = 2\pi c/\lambda$ were made, with N_A being Avogadro's number, ρ - the mass density, M - atomic weight, and λ being the wavelength of the x-ray photon. The critical angle is defined by $\theta_C = \sqrt{2\delta}$.

The wavevector, $\overrightarrow{k_m}$, of the incident electromagnetic wave ($\|\overrightarrow{k_m}\| = k_m = \omega/c$) in homogeneous layer m is reflected and refracted at the layer interface in the x, z-plane. The reflected wave propagates in the same layer, while the refracted wave becomes incident for the next, $m-1$, layer with $k_{m-1} = \sqrt{\epsilon_{m-1}}k = n_{m-1}k$. Thus, there are two waves propagating in each layer, except for the infinitely thick substrate where no reflected wave exists. From the boundary conditions, the tangential components of the wavevectors, k_{x_m}, are equal on either side of the interface, while the normal components, k_{z_m}, are different due to different electric susceptibilities of adjacent layers. The total electric field in each layer m can be written as [2]:

$$\overrightarrow{E_m^{total}}(x, y, z) = [\overrightarrow{E_m}e^{-ik_{z_m}} + \overrightarrow{E_m^R}e^{ik_{z_m}}]e^{i(\omega t - k_{x_m}x)}, \tag{A.5}$$

where $\overrightarrow{E_m}$ and $\overrightarrow{E_m^R}$ are incident and reflected waves in the middle of the layer, respectively.

In the case of glancing-incidence (θ is small)

$$k_{x_2}^2 + k_{z_2}^2 = k_2^2 = n_2^2 k_3^2 = n_2^2(k_{x_3}^2/\cos^2\theta) \approx k_{x_3}^2(1 - 2\delta_2 - 2i\beta_2 + \theta^2), \tag{A.6}$$

where in the last step higher powers of the expansions for $\sqrt{1-\delta_2-i\beta_2}$ and $\cos^2\theta$ were neglected. From boundary conditions for tangential components of the wavevectors, $k_{x_2} = k_{x_3}$, and with the small angle approximation $k_{x_3} \approx k_3$, equation A.6 can be rewritten as

$$k_{z_2} \approx k_x\sqrt{\theta^2 - 2\delta_2 - 2i\beta_2} \equiv k_x f_m, \tag{A.7}$$

where in the last equality we introduced a new symbol f_m denoting the expression under the square root.

In the mth layer, the refracted wave now is

$$E_m = E_3 e^{i(\omega t - k_{x_m}x)} e^{-ik_3 f_m z_m}. \tag{A.8}$$

The conditions for continuity for the electric field $((\overrightarrow{E_m^{total}} - \overrightarrow{E_{m-1}^{total}}) \times \overrightarrow{n} = 0)$ and magnetic $((\overrightarrow{H_m^{total}} - \overrightarrow{H_{m-1}^{total}}) \times \overrightarrow{n} = 0)$ fields at the interface between adjacent layers m and $m-1$ can be written as (keeping in mind that $\overrightarrow{H} = \sqrt{\epsilon}\,\overrightarrow{k} \times \overrightarrow{E}$)

$$a_m E_m + a_m^{-1} E_m^R = a_{m-1}^{-1} E_{m-1} + a_{m-1} E_{m-1}^R \tag{A.9}$$

and

$$(a_m E_m - a_m^{-1} E_m^R) f_m = (a_{m-1}^{-1} E_{m-1} - a_{m-1} E_{m-1}^R) f_m, \tag{A.10}$$

where $a_m = e^{-ik_{z_m} d_m/2}$ with d_m being the thickness of the mth layer.

The reflection and transmission coefficients, R_m and T_m, at the interface between m and $m-1$ layers are defined as follows

$$R_m = \frac{a_m^{-1} E_m^R}{a_m E_m}, \tag{A.11}$$

and

$$T_m = \frac{a_{m-1}^{-1} E_{m-1}}{a_m E_m}, \tag{A.12}$$

In these expressions, the field amplitudes $a_m E_m$, $a_m^{-1} E_m^R$ and $a_{m-1}^{-1} E_m$ are values of the incident, reflected and refracted waves at the interface, respectively. From equations A.11 and A.12 after some rearranging and substitutions, recursive formulas for R_m and T_m can be obtained:

$$R_m = \frac{a_m^4 R_{m-1} + G_m}{1 + a_{m-1}^4 R_{m-1} G_m} \tag{A.13}$$

and

$$T_m = \frac{1 + R_m}{1 + a_{m-1}^4 R_{m-1}} \tag{A.14}$$

where

$$G_m = \frac{f_m - f_{m-1}}{f_m + f_{m-1}} \tag{A.15}$$

As it can be readily seen from these equations, if R is known at one interface, then R and T at every interface can be calculated, provided that optical constants δ and β for each layer are available. For the infinitely thick substrate there is no reflected wave and, thus, $R_0 = 0$, giving a starting point for the recursion. The final result of the recursive process is the reflectivity of the whole system at the top surface is given by

$$\|R_3\|^2 = \left\| \frac{E_3^R}{E_3} \right\|^2, \tag{A.16}$$

where $a_3 = 1$ and $f_3 = 0$. For a given layer within the layered structure the amplitude of the electric field within it can be expressed as well:

$$E_{m-1} = T_m a_m a_{m-1} E_m, \tag{A.17}$$

and

$$E_m^R = R_m a_m^2 Em, \tag{A.18}$$

It is now possible to evaluate the field amplitudes relative to the amplitude of the original incident wave for a particular system. These field amplitudes are used in analysis of the glancing incident XAFS technique in Chapter 2.

Appendix B

Undulator A

The undulator A at the APS is a planar device optimized for the hard X-ray region of the electromagnetic spectrum (Fig. B.1). It is 2.4 m long with 144 magnet pairs (72 periods, each period is 3.3 cm long). It provides high brilliance X-rays in the range from 4.2 keV to 30 keV utilizing either first or third harmonic radiation (discussed below) [1].

Figure B.1: Undulator A at the Advanced Photon Source [2].

The undulator is inserted in the path of the electron bunch in the storage ring in such a way that electrons go through the gap between the magnets' array. Due to the periodic magnet structure, electrons undergo oscillations and, consequently, emit EM radiation. To describe these oscillations and the resulting radiation to a good approximation it is sufficient to treat the electron as a classical relativistic particle moving in the periodic magnetic field $\overrightarrow{B} = B_0 \cos(\frac{2\pi z}{\lambda_u}) \cdot \widehat{j}$. Here, the electron is chosen to be moving along the z-axis with relativistic speed v in a periodic magnetic field oscillating along the y-axis with λ_u period. In reality, the magnetic field takes a more complex form, but we ignore it for the sake of a qualitative picture and briefly review it following the derivation in [3].

In the frame of the moving electron the spatial periodicity of the magnet structure is contracted to $\lambda' = \frac{\lambda_u}{\gamma}$, where $\gamma = \frac{1}{\sqrt{1-\frac{v^2}{c^2}}}$. In the laboratory frame of reference, the radiation wavelength is reduced even more due to the Doppler shift which depends on the relative velocity between the electron and the observer. Since the relative velocity depends on the angle between the actual electron velocity and direction to the observer, θ_o, this reduction factor depends on it as well [4]: $\lambda = \lambda_u(1 - \beta \cos\theta_o)$, where $\beta = \frac{v}{c}$. At the APS 7 GeV electrons are accelerated to a speed such that $\beta \approx 0.99999999$. Considering small angles of observation when θ_o lies within the narrow radiation cone (typical case for an insertion device, such as undulator) we can expand $\cos\theta_o = 1 - \frac{\theta_o^2}{2} + \ldots$ in the Taylor series. On the other hand, for a relativistic electron $\beta \approx 1$ and $1 - \beta \approx \frac{1}{2\gamma^2}$. The resulting wavelength of the radiation emitted by the electron is given then by

$$\lambda = \frac{\lambda_u}{2\gamma^2}(1 + \gamma^2\theta_o^2) \tag{B.1}$$

As follows from the equation (B.1) with θ_o equal to 0, the radiation has a greatly reduced wavelength, λ, comparing to the period of the magnet structure, λ_u. For the undulator A at the APS $\frac{\lambda}{\lambda_u} \approx 2.6645 \times 10^{-9}$.

In the approximation that effects of the EM field radiated by the electron itself due to its oscillations are weak and in the absence of any external electric field, the equation of motion for such electron can be written by the familiar equation

$$\frac{d\overrightarrow{p}}{dt} = -e(\overrightarrow{v} \times \overrightarrow{B}) \tag{B.2}$$

where $\overrightarrow{p} = \gamma m \overrightarrow{v}$ is the electron momentum, e and m are the electron's charge and its mass, respectively. Making the additional approximation of $\overrightarrow{v} \simeq v \cdot \widehat{k}$, the equation (B.2) can be rewritten as

$$m\gamma\frac{dv_x}{dt} = e\frac{dv_z}{dt}B_0\cos\left(\frac{2\pi z}{\lambda_u}\right) \tag{B.3}$$

and after rearranging and integrating it becomes

$$v_x = \frac{eB_0\lambda_u}{2\pi m\gamma}\sin\left(\frac{2\pi z}{\lambda_u}\right) = \frac{Kc}{\gamma}\sin\left(\frac{2\pi z}{\lambda_u}\right) \tag{B.4}$$

where we introduced $K = \frac{eB_0\lambda_u}{2\pi mc}$ as a dimensionless magnetic strength factor of the periodic magnet structure. Factor K is often referred to as the deflection parameter. It can be changed by changing the amplitude B_0 of the magnetic field. In practice this is done by varying the vertical gap between the magnets.

The angle between the instant electron velocity and z-axis (the direction of the overall electron propagation) is given by

$$\tan\theta_e = \frac{v_x}{v_z} \approx \frac{K}{\gamma}\sin\left(\frac{2\pi z}{\lambda_u}\right) \tag{B.5}$$

From equation (B.5) it can be seen that the maximum angle is $\approx \frac{K}{\gamma}$. Comparing it to the half-angle of the radiation emitted by the electron, given by $\theta_r \approx \frac{1}{2\gamma}$ [5], two important regimes can be seen. For $K \leq 1$ (undulator regime), the electron angular deviations lie within the radiation cone. As a result, interference effects play an important role leading to narrow radiation bandwidth and narrower radiation cones. For $K \gg 1$ (wiggler regime), interference does not play a dominating role, because oscillations from different magnet structure segments differ strongly in angle. This leads to increase in radiated power and wide radiation bandwidth with continuous spectrum as its limit.

In the solution (B.4), $z \approx ct$, but more precisely it is not a linear function of time. It is an oscillating function itself as is v_z. As a consequence it gives rise to harmonics in the EM radiation emitted by the electron. These harmonics are an extremely important feature in the undulator operation as will be seen later.

Using equation (B.4) and the fact that $\gamma = \frac{1}{\sqrt{1-\frac{v_x^2+v_z^2}{c^2}}}$, we obtain the expression for v_z [3]:

$$v_z = c\sqrt{1 - \frac{1}{\gamma^2} - \frac{K^2}{\gamma^2}\sin^2\left(\frac{2\pi z}{\lambda_u}\right)} \tag{B.6}$$

which in the relativistic limit of small parameter K/γ can be approximated with

$$v_z = c\left(1 - \frac{1+\frac{1}{2}K^2}{2\gamma^2} + \frac{K^2}{4\gamma^2}\cos\left(\frac{4\pi z}{\lambda_u}\right)\right) \tag{B.7}$$

where the trigonometric identity $\sin^2\alpha = \frac{1}{2}\left(1-\cos(2\alpha)\right)$ was used. It can be seen from the equation (B.7) that the electron's velocity component along the direction of its propagation (z-axis) has a reduced average part and an oscillating contribution with frequency twice that of the magnetic structure spatial frequency. Averaging over the length of the periodic magnetic structure, L, gives us the average value of the v_z (ignoring the higher order components):

$$\overline{v}_z = c\left(1 - \frac{1+\frac{1}{2}K^2}{2\gamma^2}\right) \tag{B.8}$$

Introducing an effective axial value of the relativistic factor $\gamma_a = \frac{\gamma}{\sqrt{1+\frac{1}{2}K^2}}$ that includes the deflection parameter of the magnet structure, we can rewrite the equation (B.8) as

$$\overline{v}_z = c\left(1 - \frac{1}{2\gamma_a^2}\right) \tag{B.9}$$

Now, we can also rewrite equation (B.1) using γ_a instead of γ. After substitution we obtain the undulator equation:

$$\lambda = \frac{\lambda_u}{2\gamma^2}\left(1 + \frac{1}{2}K^2 + \gamma^2\theta_o^2\right) \tag{B.10}$$

It describes the generation of X-ray radiation through the relativistic reduction factor $\frac{\lambda_u}{2\gamma^2}$, magnetic tuning through $\frac{1}{2}K^2$, and angular wavelength variation through $\gamma^2\theta_o^2$ factor.

The importance of the magnetic tuning is significant from the experimental point of view. It allows independent tuning at the beam station (by adjusting the magnets' gap), independent of the γ factor of electrons in the storage ring.

In practice it is convenient to operate with energy of the emitted radiation rather than its wavelength. By substituting constants and converting to energy scale using $E = 2\pi\frac{\hbar c}{\lambda}$, we obtain:

$$E[keV] = \frac{0.9496E_e^2[GeV]}{\lambda_u[cm]\left(1+\frac{1}{2}K^2+\gamma^2\theta_o^2\right)} \tag{B.11}$$

where E is photon energy in keV and E_e is electron beam energy in GeV.

Substituting $z \approx \overline{v}_z t$ and integrating equations (B.4) and (B.7) with respect to time one can obtain equations for x' and z' coordinates of the moving electron in the electron frame of reference [3]. The important result of somewhat complex solutions from the spectroscopy perspective is that both coordinates contain spectral contributions at wavelengths that are integer multiples of a fundamental wavelength. The odd harmonics appear in the oscillations along the x'-axis and the even - perpendicular to them, along the z'-axis. The photon energy of the nth harmonic, E_n, is related to the fundamental energy in equation (B.11) by a simple rule $E_n = nE$, where n is a integer positive number.

The even harmonics radiation produced by the oscillations in the z'-direction, after the Lorentz transformation, in laboratory frame of reference will form a hollow cone along the direction of electron's propagation ($\theta_o = 0$). It contributes little to the intensity along the z-axis. The intensity of the odd harmonics radiation, on the other hand, in the laboratory frame of reference will be concentrated in the cone along the z-axis. It has narrow spectral bandwidth and linear polarization in the plane of the storage ring. These harmonics are widely utilized in spectroscopic experiments.

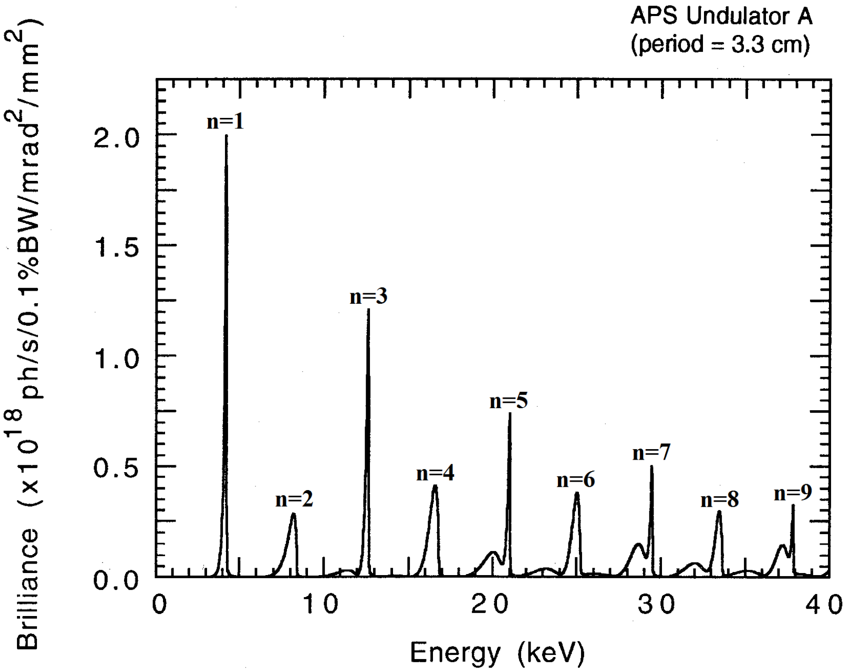

Figure B.2: Undulator A brilliance spectrum showing fundamental, even and odd harmonics for $K = 2.17$ (1.15 cm gap) at 7 GeV storage ring operating energy with electron current 100 mA [1].

Figure (B.2) shows spectral brilliance of undulator A along the z-axis ($\theta_o = 0$) with magnetic deflection factor $K = 2.17$ [1]. Spectral brilliance is defined as the photon intensity per unit phase space of the source, which is an invariant parameter. It is used to characterise the spectral properties of a SR source. It can be seen that the relative intensity of the odd harmonics drops as a function of energy, while the intensity of the even harmonics remains at a somewhat constant, but low value.

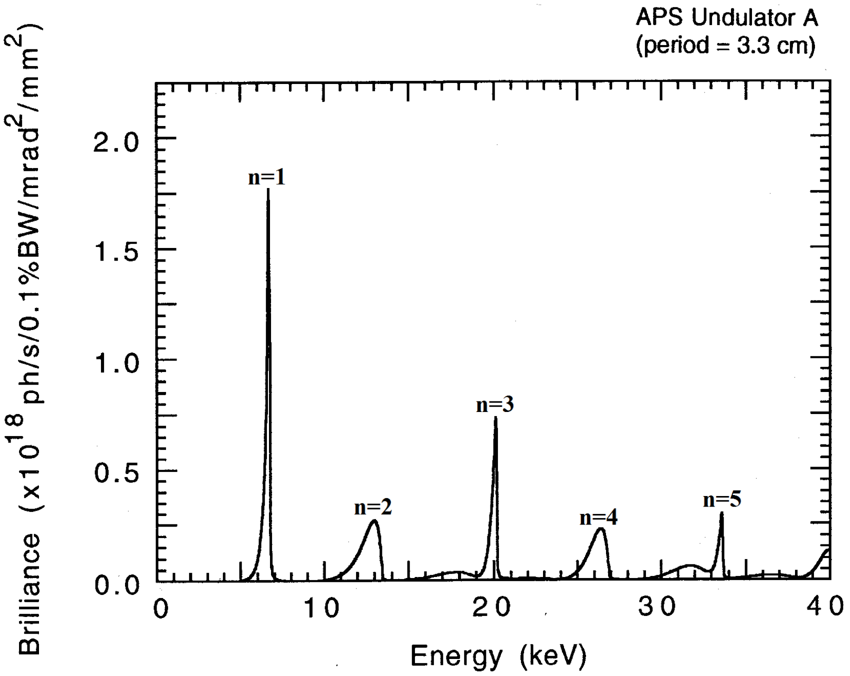

Figure B.3: Undulator A brilliance spectrum showing fundamental, even and odd harmonics for $K = 1.48$ (1.55 cm gap) at 7 GeV storage ring operating energy with electron current 100 mA [1].

Figure (B.3) shows a similar plot, but for a different, lower $K = 1.48$ (1.55 cm gap). Notice the shift in the harmonic energies and increase in spectral bandwidth of individual harmonics along with intensity drop. Effectively, this is the above mentioned magnetic tuning. It allows to utilize high brilliance of the undulator source without sacrificing spectral freedom: changing K and shifting the harmonic allows access to any energy of interest in the wide range from 4.2 keV to 30 keV.

Figures (B.4) and (B.5) show spectral brilliance of the fundamental and third harmonic, respectively, for a set of different K parameter values. By comparison, it's clear that around

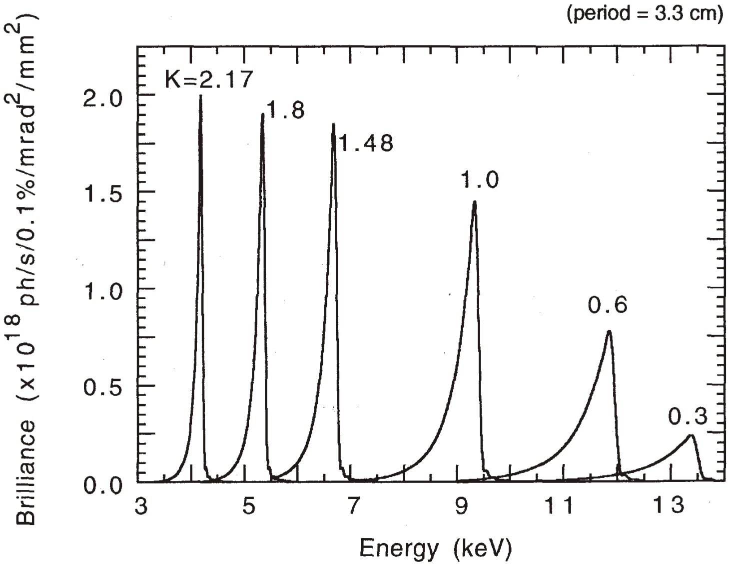

Figure B.4: Undulator A first harmonic spectral brilliance as a function of K magnetic deflection parameter at 7 GeV storage ring operating energy with electron current 100 mA [1].

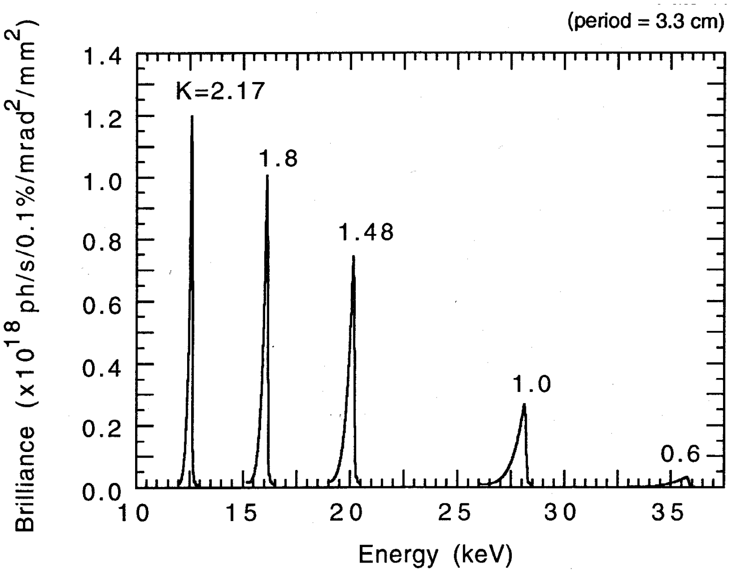

Figure B.5: Undulator A third harmonic spectral brilliance as a function of K magnetic deflection parameter at 7 GeV storage ring operating energy with electron current 100 mA [1].

13 keV, the brilliance of the fundamental harmonic drops significantly. It becomes about 5 times less than the brilliance of the third harmonic at this energy. At this point, one can switch to using the third harmonic in order to increase the brilliance.

Finally, figure (B.6) shows the tuning curve for the first three harmonics, obtained by plotting the peak of the brilliance as a function of K. It provides an illustrative guidance to selecting a particular harmonic for a specific energy range. In this thesis, for example, for the Fe K-edge energy the first harmonic was used, while for the Pd K-edge at much higher energy - the third.

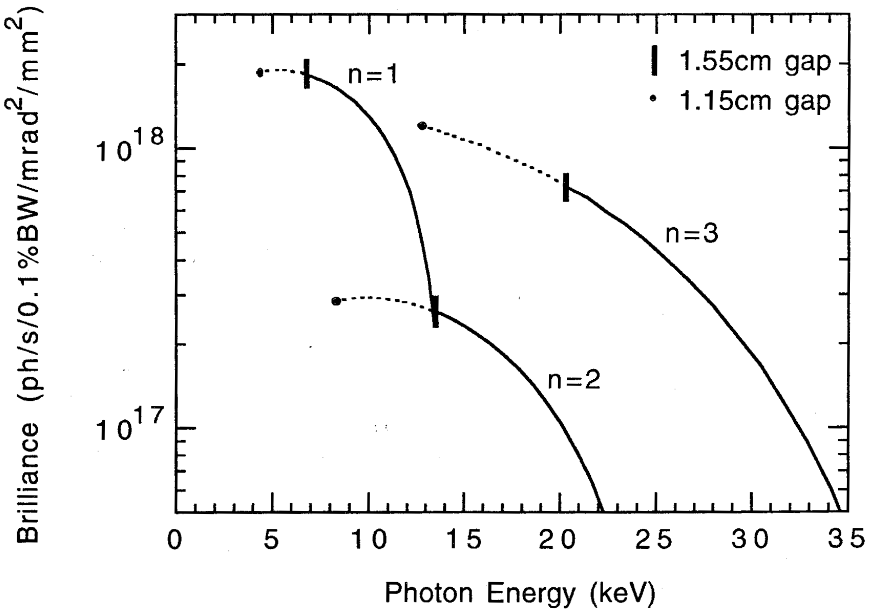

Figure B.6: Undulator A tuning curve for the fundamental, second and third harmonics at 7 GeV storage ring operating energy with electron current 100 mA [1].

At the PNC beamline, sector 20, the $n = 3$ harmonic has been used for XAFS measurements at the I K-edge (33.169 keV) and the $n = 7$ harmonic has been used for XAFS measurements at the Gd K-edge (55.239 keV).

Appendix C

Theoretical Backscattering Amplitude and Phase

To fit the EXAFS equation 4.1 (see Chapters 4) it is necessary to have backscattering amplitudes, $F(k)$, phase shifts, $\phi(k)$, plus absorber phase shift, $\delta(k)$, available. One possible approach is to extract these functions from experimental data of a known reference compound. Another approach is to calculate these functions theoretically. In this thesis the second approach was utilized, and the backscattering amplitudes and phase shifts were calculated using the FEFF7 software package [1]. FEFF7 calculates polarization-dependent effective backscattering amplitudes and phase shifts for an atomic cluster using the curved-wave photoelectron approximation, including multiple-scattering. As pointed out in Chapter 2, because of that both the FEFF7 backscattering amplitudes and phase shifts effectively become R-dependent, while the backscattering amplitudes also becomes a function of the angle between the polarization vector and the direction of the photoelectron propagation: $F(k, R, \alpha)$ and $\phi(k, R)$.

As mentioned in Chapter 4, in the fitting of thin iron films on GaAs, Ga and As were approximated by Ge for simplicity of calculations and fitting. Figures C.1 and C.2 show $F(k)$ and $\phi(k)$ for all three elements. It can be seen that the backscattering amplitudes and phase shifts for Ge lie in-between those of Ga and As, and, indeed, can be used as an approximation within XAFS experimental error for nearest neighbour coordination numbers, N_i. The calculations were performed in a cluster of 321 atoms in the face-centered cubic lattice structure for Pd K-edge with the absorber being Pd.

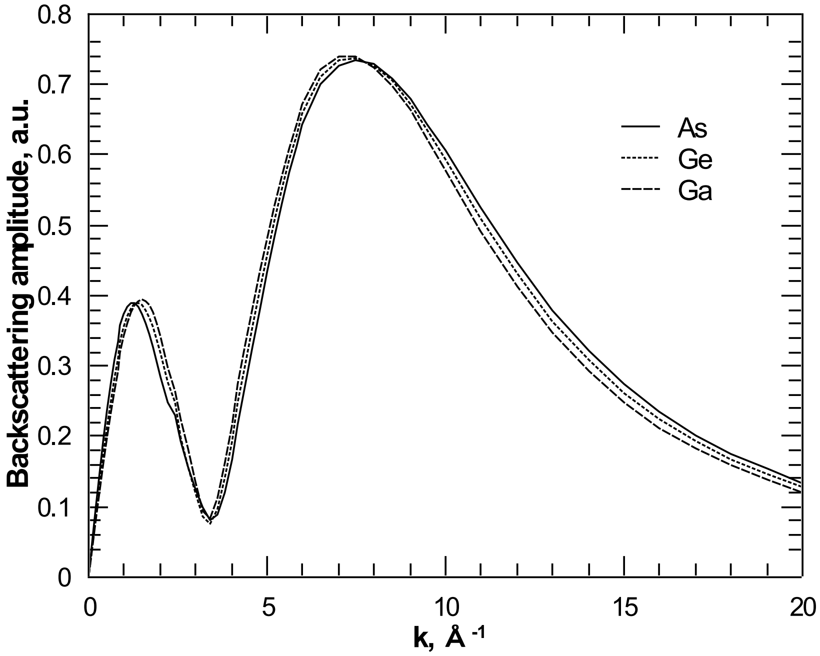

Figure C.1: As, Ga and Ge backscattering amplitudes. Averaged polarization with bond length equal to 2.75 Å.

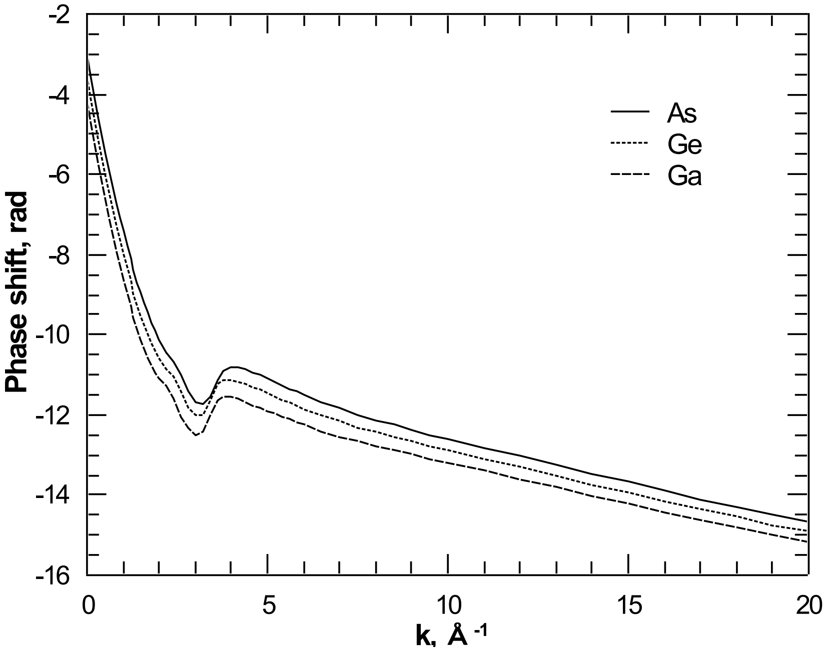

Figure C.2: As, Ga and Ge backscattering phase shifts. Averaged polarization with bond length equal to 2.75 Å.

The shown functions were obtained for a direct backscattering path using unpolarized incoming X-ray photons. Notice, that only the backscattering phase shift, $\phi(k)$, is shown in figure C.2 - the absorber phase shift, $\delta(k)$, virtually does not change (small changes due to different environment are negligible from the XAFS point of view).

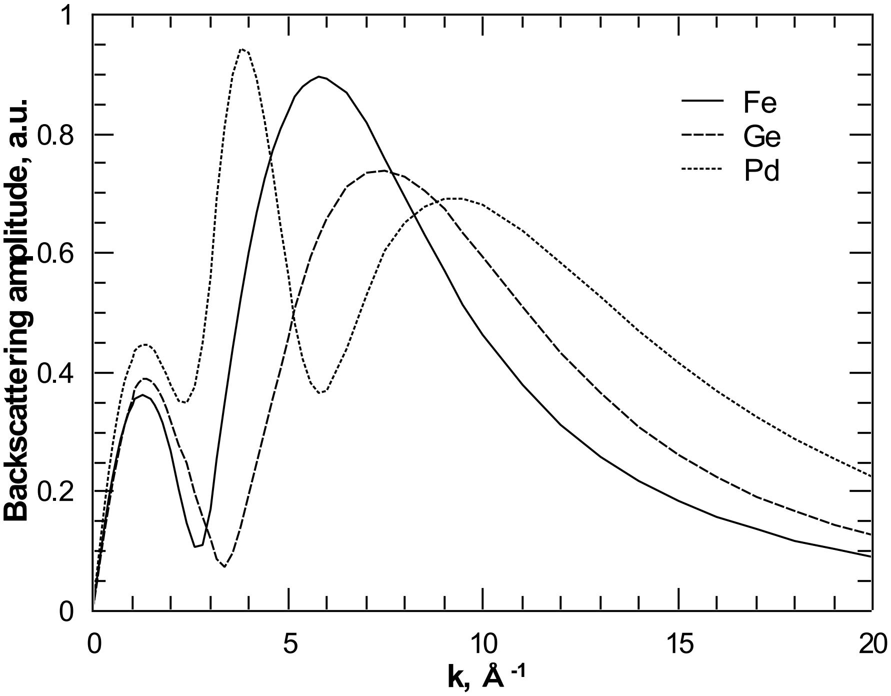

Figure C.3: Fe, Ge and Pd backscattering amplitudes. Averaged polarization with bond length equal to 2.75 Å.

In the approximation discussed above, it was desired that the backscattering amplitudes and phase shifts for the three elements were as similar as possible to allow for the substitution. However, in order to distinguish one atomic species from another it is required for $F(k)$ and $\phi(k)$ to be different. Figures C.3 and C.4 show the backscattering amplitude and phase shifts for Fe, Ge and Pd in averaged polarization. In this thesis, typically, the fitting k-range was between 1.5 Å^{-1} and 13 Å^{-1}. In this range, the difference between the three is pronounced, especially for Pd which has an extra minimum in $F(k)$ comparing to Fe and Ge since it has a significantly different atomic potential due to the extra electron shells. The calculations were performed for clusters similar to that described earlier.

When fitting the data it is inevitable that the initial model for which the theoretical calculations were done is not precise. That means, the bond length, being a fit parameter, will be adjusted from the value for which $F(k)$ was calculated. There are two approaches to include the polarization dependence of the data in the fit. One is to scale the coordination numbers based on the angle between the bond length vector and the polarization vector [2]. Another, used in FEFF7, is to implement polarization dependence directly into the back scattering amplitude $F(k)$. Figure C.5 shows the backscattering amplitude for Pd at different angles between the bond length vector and the polarization vector of the incoming photon. It is apparent, that if the fit would suggest a significant change in the bond angle with respect to the assumed polarization, adjustments to the theoretical model should be made accordingly in order to obtain reliable coordination numbers.

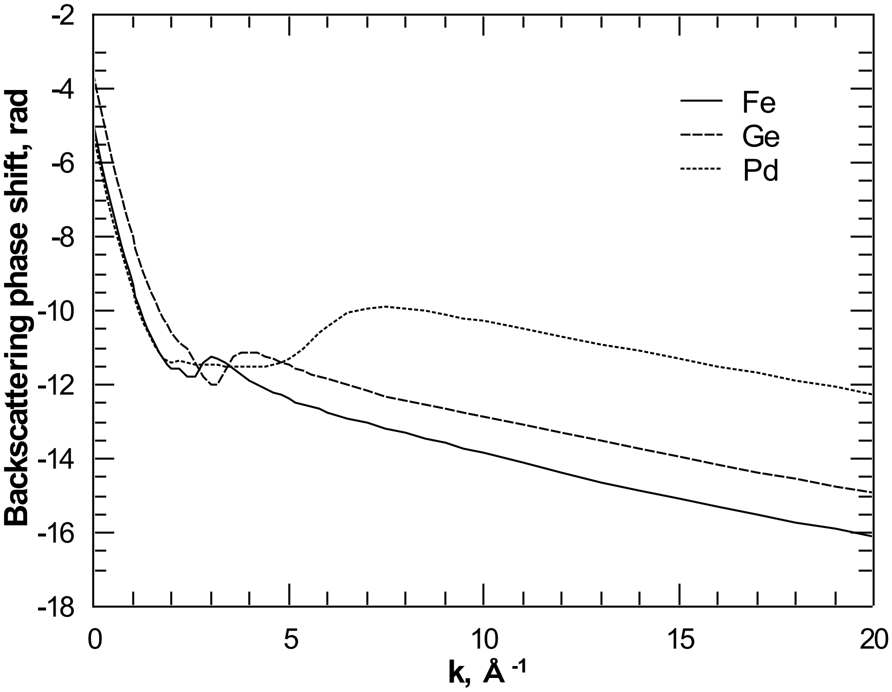

Figure C.4: Fe, Ge and Pd backscattering phase shifts. Averaged polarization with bond length equal to 2.75 Å.

Since backscattering amplitudes do depend on the bond length (due to the photoelectron propagating through the muffin-tin potential), it is important to ensure that these bond length variations are not significant during the fit, so the error in $F(k)$ will be small. Figures C.6 and C.7 show backscattering amplitudes and phase shifts for Pd for averaged polarization for different bond lengths as stated on the graph. It is clear that while the dependence is weak, any large deviations from the assumed bond lengths during the fit can result in additional error in nearest neighbour coordination numbers. To avoid this problem the fit was iterative: once a fit was obtained for the initial model, new theoretical calculations were performed for a model that matches the fit closer, and the fit was re-done.

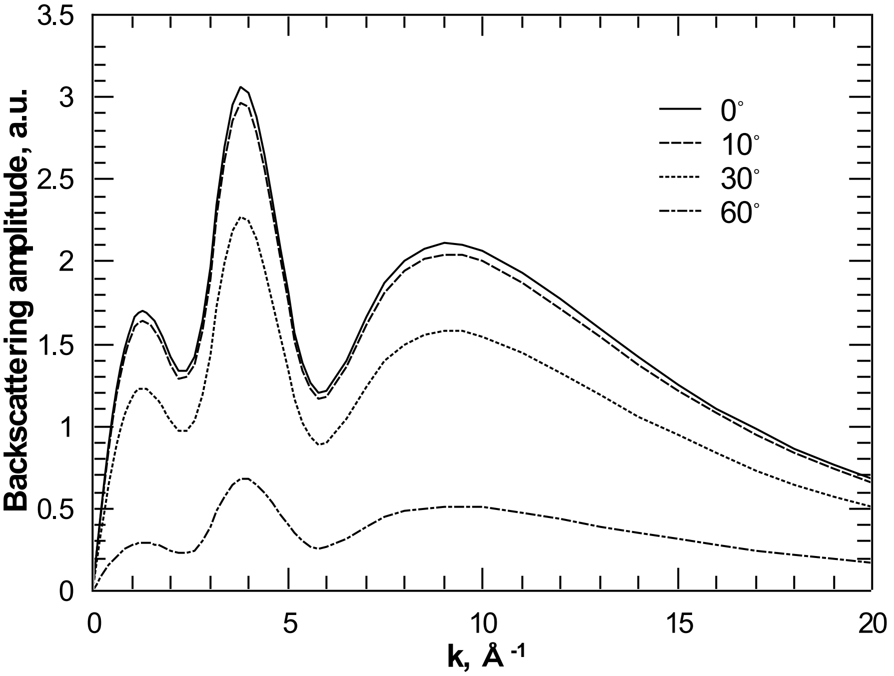

Figure C.5: Pd backscattering amplitudes for different polarization. Bond length is equal to 2.75 Å.

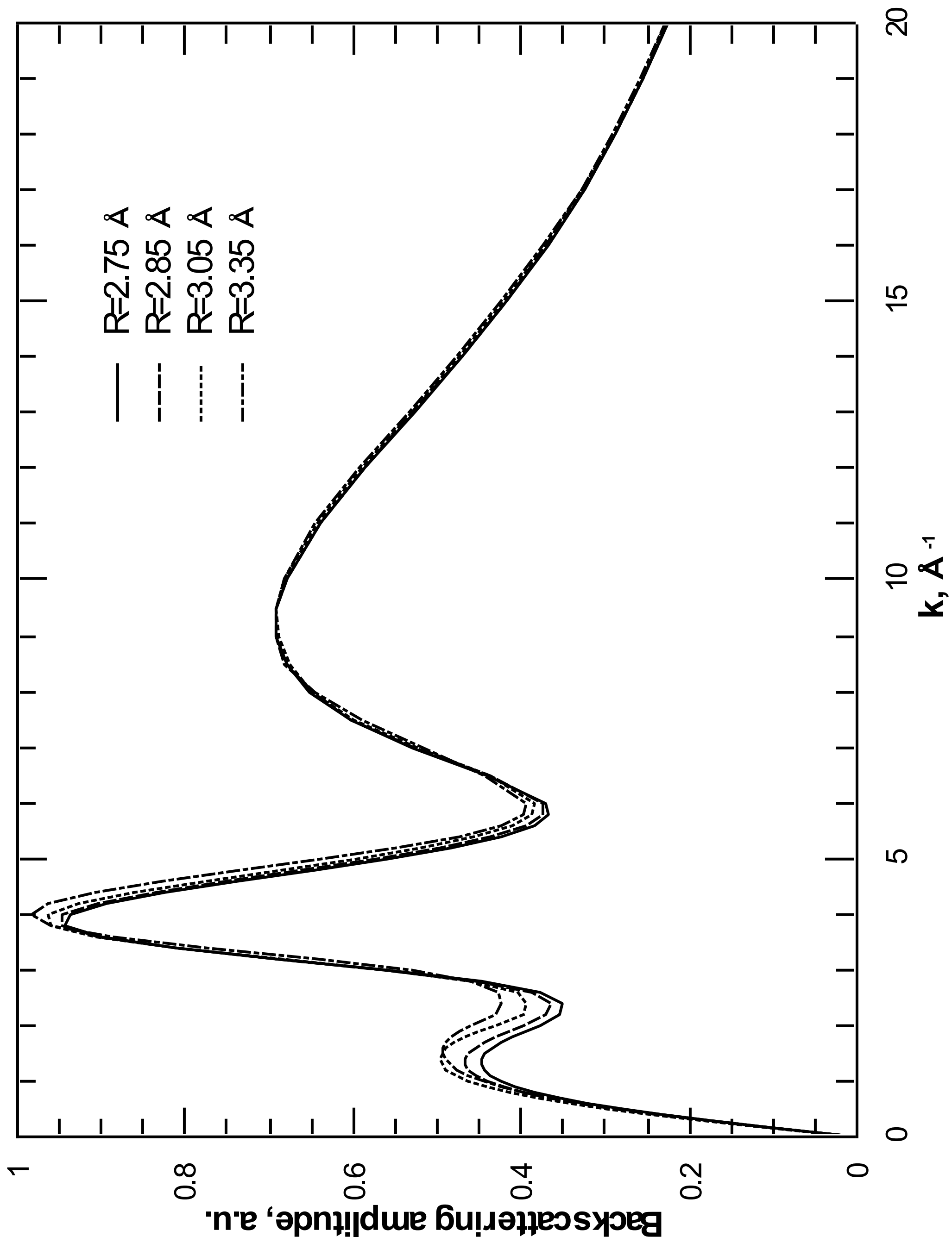

Figure C.6: Pd backscattering amplitudes for different bond lengths. Averaged polarization.

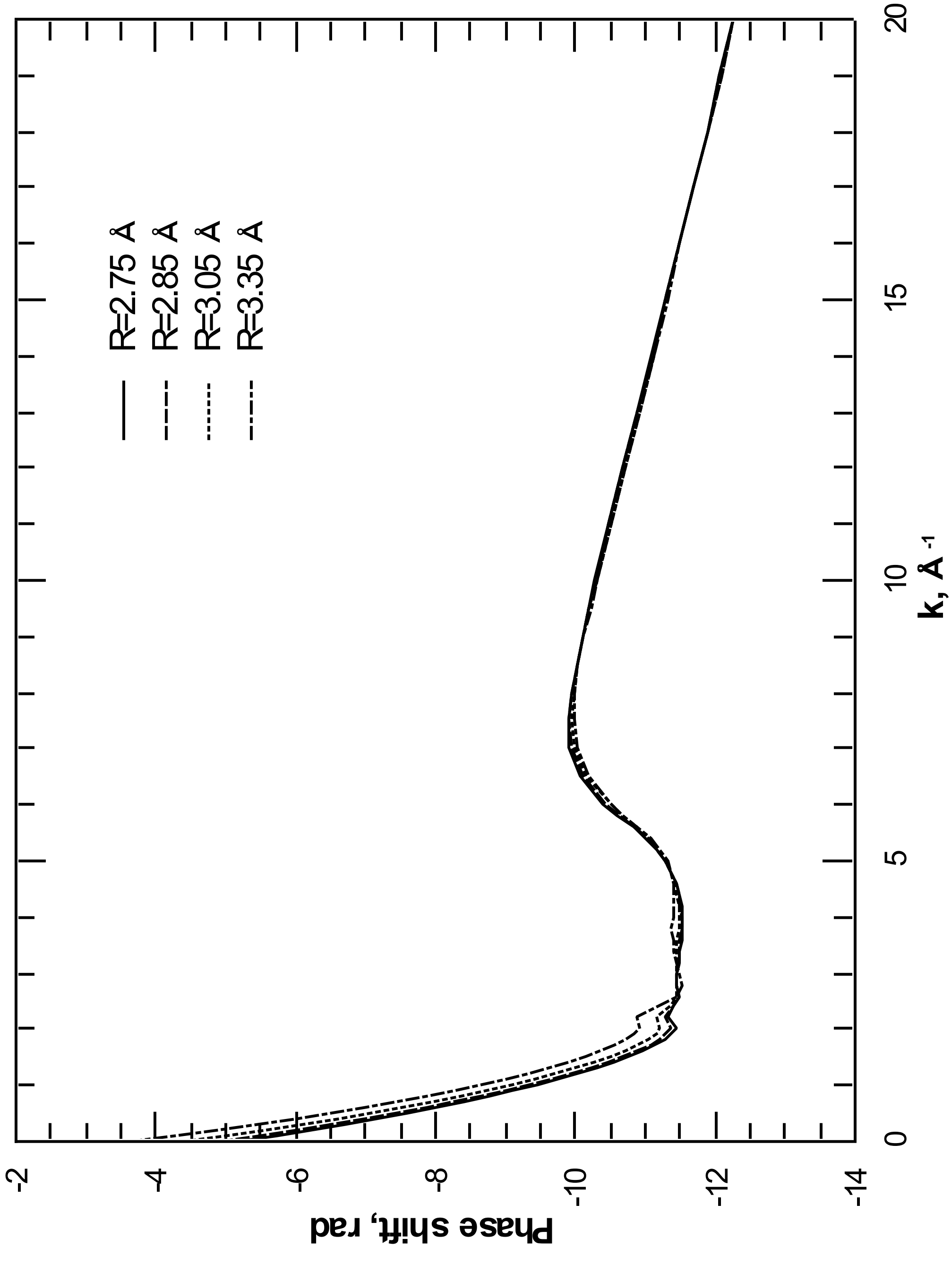

Figure C.7: Pd backscattering phase shifts for different bond lengths. Averaged polarization.

Bibliography for Chapter 1

[1] B. Heinrich and J.A.C. Blanc, editors. *Ultrathin Magnetic Structures*, volume 1: An Introduction to the Electronic, Magnetic and Structural Properties. Springer-Verlag: Berlin, 1994.

[2] B. Heinrich and J.A.C. Blanc, editors. *Ultrathin Magnetic Structures*, volume 2: Measurement Techniques and Novel Magnetic Properties. Springer-Verlag: Berlin, 1994.

[3] G.Wastlbauer and J.A.C. Bland. Structural and magnetic properties of ultrathin epitaxial Fe films on GaAs(001) and related semiconductor substrates. *Advances in Physics*, 54(2):137–219, 2005.

[4] T.L. Monchesky. *Magnetoresistance and Magnetic Properties Magnetic Multilayers Grown Directly on GaAs(001).* PhD thesis, Simon Fraser University, 2000.

[5] P. Bruno. Dipolar magnetic surface anisotropy in ferromagnetic thin films with interfacial roughness. *J. Appl. Phys.*, 64:3153–3156, 1988.

[6] P. Bruno. Magnetic surface anisotropy of cobalt and surface roughness effects within Neels model. *J. Phys. F*, 18:1291–1298, 1988.

[7] Wikipedia.org. MRAM. *(http://en.wikipedia.org/wiki/MRAM)*, 2012.

[8] T. Lee. Non-volatile MRAM is ready for prime time. *Electronic Products*, November Issue:39, 2006.

[9] G.A. Prinz, B.T. Jonker, J.J. Krebs, J.M. Ferrari, and F. Kovanic. Growth of single crystal bcc α-Fe on ZnSe via molecular beam epitaxy. *Appl. Phys. Lett.*, 48(25):1756–1758, 1986.

[10] S. Datta and B. Das. Electronic analog of the electro-optic modulator. *Appl. Phys. Lett.*, 56(7):665–667, 1990.

[11] G. Schmidt, D. Ferrand, L.W. Molenkamp, A. T. Filip, and B. J. van Wees. Fundamental obstacle for electrical spin injection from a ferromagnetic metal into a diffusive semiconductor. *Phys. Rev. B*, 62(8):R4790–R4793, 2000.

[12] H. J. Zhu, M. Ramsteiner, H. Kostial, M. Wassermeier, H.-P. Schönherr, and K. H. Ploog. Room-temperature spin injection from Fe into GaAs. *Phys. Rev. Lett.*, 87(1):016601–016605, 2001.

[13] A. T. Hanbicki, O. M. J. van 't Erve, R. Magno, G. Kioseoglou, C. H. Li, G. Itskos, R. Mallory, M. Yasar, and A. Petrou. Analysis of the transport process providing spin injection through an Fe/AlGaAs Schottky barrier. *Appl. Phys. Lett.*, 82(23):4092–4094, 2003.

[14] D.R. Lide, editor. *CRC Handbook of Chemistry and Physics: Internet Version 2007 (http://www.hbcpnetbase.com).* Taylor and Francis: Boca Raton FL, 87th edition, 2007.

[15] J.P. LaFemina. Total-energy calculations of semiconductor surface reconstructions. *Surf. Sci. Rep.*, 16:133–260, 1992.

[16] C.B. Duke. Semiconductor surface reconstruction: the structural chemistry of two-dimensional surface compounds. *Chem. Rev.*, 96:1237–1259, 1996.

[17] W.A. Harrison. *Electronic Structures and the Properties of Solids.* Freeman: San Francisco, 1980.

[18] M.D. Pashley. Electron counting model and its application to island structures on molecular-beam epitaxy grown GaAs(001) and ZnSe(001). *Phys. Rev. B*, 40(15):10481–10487, 1989.

[19] Q.-K. Xue, T. Hashizume, and T. Sakurai. Scanning tunneling microscopy study of GaAs(001) surfaces. *Appl. Surf. Sci.*, 141(3):244263, 1999.

[20] D.K. Biegelsen, R.D. Bringans, and and L.-E. Swartz J.E. Northrup. Surface reconstructions of GaAs(100) observed by scanning tunneling microscopy. *Phys. Rev. B*, 41:5701–5711, 1990.

[21] S.A. Chambers, F. Xu, H.W. Chen, I.M. Vitomirov, S.B. Anderson, and J.H. Weaver. Simultaneous epitaxy and substrate out-diffusion at a metal-semiconductor interface: Fe/GaAs(001)-$c(8\times2)$. *Phys. Rev. B*, 34:6605–6611, 1986.

[22] F. Bensch, G. Garreau, R. Moosbühler, G. Bayreuther, and E. Beaurepaire. Onset of ferromagnetism in Fe epitaxially grown on GaAs(001) (4×2) and (2×6). *J. Appl. Phys.*, 89(11):71337135, 2001.

[23] K. Sano and T.Miyagawa. Microscopic processes in deposition-concurrent surface segregation. *Appl. Surf. Sci.*, 60/61:813819, 1992.

[24] M. Zölfl, S. Kreuzer, T. Schweinböck, M. Brockmann, M. Köhler, S. Miethaner, F. Bensch, and G. Bayreuther. Magnetic films epitaxially grown on semiconductors. *J. Magn. Mag. Mater.*, 175:16–22, 1997.

[25] Y.B. Xu, E.T.M. Kernohan, D.J. Freeland, A. Ercole, M. Tselepi, and J.A.C. Bland. Evolution of the ferromagnetic phase of ultrathin Fe films grown on GaAs(100)-(4×6). *Phys. Rev. B*, 58(2):890–896, 1997.

[26] M. Brockmann, M. Zölfl, S. Miethaner, and G. Bayreuther. In-plane volume and interface magnetic anisotropies in epitaxial Fe films on GaAs(001). *J. Magn. Mag. Mater.*, 198/199:384–386, 1997.

[27] T.L. Monchesky, B. Heinrich, R. Urban, K. Myrtle, M. Klaua, and J. Kirschner. Magnetoresistance and magnetic properties of Fe/Cu/Fe/GaAs(100). *Phys. Rev. B*, 60(14):10242–10251, 1999.

[28] E.M. Kneedler, B.T. Jonker, P.M. Thibado, R.J. Wagner, B.V. Shanabrook, and L.J.Whitman. Influence of substrate surface reconstruction on the growth and magnetic properties of Fe on GaAs(001). *Phys. Rev. B*, 56(13):8163–8168, 1997.

[29] E. Kneedler, P.M. Thibado, B.T. Jonker, B.R. Bennett, B.V. Shanabrook, R.J.Wagner, and L.J. Whitman. Epitaxial growth, structure and composition of Fe films on GaAs(001)-(2×4). *J. Vacuum Science and Technology B*, 14(4):3193–3198, 1996.

[30] P.M. Thibado, E. Kneedler, B.T. Jonker, B.R. Bennett, B.V. Shanabrook, and L.J. Whitman. Nucleation and growth of Fe on GaAs(001)-(2×4) studied by scanning tunneling microscopy. *Phys. Rev. B*, 53(16):R10481–R10484, 1996.

[31] B.T. Jonker and G.A. Prinz. Auger electron diffraction study of the growth of Fe(001) films on ZnSe(001). *J. Appl. Phys.*, 69(5):2938–2941, 1991.

[32] E. Reiger, E. Reinwald, G. Garreau, M. Ernst, M. Zölfl, F. Bensch, S. Bauer, H. Preis, and G. Bayreuther. Magnetic moments and anisotropies in ultrathin epitaxial Fe films on ZnSe(001). *J. Appl. Phys.*, 87(9):5923–5925, 2000.

[33] M. Marangolo, F. Gustavsson, M. Eddrief, Ph. Sainctavit, V.H. Etgens, V. Cros, F. Petroff, J.M. George, P. Bencok, and N.B. Brookes. Magnetism of the Fe/ZnSe(001) interface. *Phys. Rev. Lett.*, 88(21):217–202, 2002.

[34] G.W. Anderson, P. Ma, and P.R. Norton. The growth of Fe on sulphur passivated Ge(100): a technique for avoiding intermixing. *J. Appl. Phys.*, 79(8):5641–5643, 1996.

[35] P. Ma and P.R. Norton. Growth of ultrathin Fe films on Ge(100): structure and magnetic properties. *Phys. Rev. B*, 56(15):9881–9886, 1997.

[36] B. Lépine, C. Lallaizon, S. Ababou, A. Guivarch, S. Députier, A. Filipe, F. Nguyen Van Dau, A. Schuhl, F. Abel, and C. Cohen. Fe/GaAs(001) and Fe/GaSb(001) heterostructures: epitaxial growth and magnetic properties. *J. Cryst. Growth*, 201/202:702–706, 1999.

[37] C. Adelmann, X. Lou, J. Strand, C. J. Palmstrom, and P. A. Crowell. Spin injection and relaxation in ferromagnet-semiconductor heterostructures. *Phys. Rev. B*, 71:121301–121305, 2005.

[38] F. Zavaliche, W. Wulfhekel, and J. Kirschner. Growth and magnetic properties of Fe films on InP(001). *Phys. Rev. B*, 65(24):245317–245326, 2002.

[39] C.M. Teodorescu, F. Chevrier, C. Richter, V. Ilakovac, O. Heckmann, L. Lechevalier, R. Brochier, R.L. Johnson, and K. Hricovini. Structure of Fe layers grown on InAs(100). *Appl. Surface Science*, 166:137–142, 2000.

[40] B. Lépine, P. Schieffer, and G. Jézéquel. Substrate disruption and surface segregation for Fe/InAs(001). *Surf. Sci.*, 497:341–348, 2002.

[41] C.M. Teodorescu, F. Chevrier, R. Brochier, C. Richter, V. Ilakovac, O. Heckmann, P. De Padova, and K. Hricovini. Reactivity and magnetism of Fe/InAs(100) interfaces. *Eur. Phys. J. B*, 28:305–313, 2002.

[42] Y.B. Xu, E.T.M. Kernohan, D.J. Freeland, M. Tselepi, A. Ercole, and J.A.C. Bland. Structure and magnetic properties of epitaxial Fe films on GaAs(100) and InAs(100). *J. Magn. Mag. Mater.*, 198/199:703–706, 1999.

[43] M. Tischer, O. Hjortstam, D. Arvanitis, J. Hunter Dunn, F. May, K. Baberschke, J. Trygg, J.M. Wills, B. Johansson, and O. Eriksson. Enhancement of orbital magnetism at surfaces: Co on Cu(100). *Phys. Rev. Lett.*, 75(8):1602–1605, 1995.

[44] J. Thomassen, F. May, B. Feldmann, M. Wuttig, and H. Ibach. Magnetic live surface layers in Fe/Cu(100). *Phys. Rev. Lett.*, 69(26):3831–3834, 1992.

[45] J. Hunter Dunn, D. Arvanitis, and N. Martensson. Magnetism of thin Fe films on Cu(100). *Phys. Rev. B*, 54(16):157–160, 1996.

[46] J. Shen, R. Skomski, M. Klaua, H. Jenniches, S. Sundar Manoharan, and J. Kirschner. Magnetism in one dimension: Fe on Cu(111). *Phys. Rev. B*, 56(2):2340–2343, 1997.

[47] H. J. Elmers, J. Hauschild, H. Höche, U. Gradmann, H. Bethge, D. Heuer, and U. Köhler. Submonolayer magnetism of Fe(110) on W(110): Finite width scaling of stripes and percolation between islands. *Phys. Rev. Lett.*, 73(6):898–901, 1994.

[48] C. Boeglin, H. Bulou, J. Hommet, and X. Le Cann. Influence of structural characteristics on magnetic properties in face-centered-tetragonal surface alloy of Fe/Pd(100). *Phys. Rev. B*, 60(6):4220–4230, 1999.

[49] M.K. McManus. *X-ray Absorption Fine Structure Measurments of the Lattice Strain in Magnetic Ultrathin Films.* PhD thesis, Simon Fraser University, 1996.

[50] D. Jiang. *Structural Investigations of Metastable Epitaxial Metallic Layers by Glancing-incidence X-ray Absorption Fine Structure.* PhD thesis, Simon Fraser University, 1991.

[51] Y.R. Bonin. *X-ray Absorption Fine Structure study of magnetic films.* PhD thesis, Simon Fraser University, 1999.

[52] J.A. Gupta. *Layer perfection in ultrathin InA quantum wells in GaAs(001).* PhD thesis, Simon Fraser University, 1999.

[53] S. Kahwaji, R. A. Gordon, E. D. Crozier, and T. L. Monchesky. Local structure and magnetic properties of B2- and B20-like ultrathin Mn films grown on Si(001). *Phys. Rev. B*, 85:014405–014414, 2012.

[54] H. L. Meyerheim, E. D. Crozier, R. A. Gordon, Q. F. Xiao, K. Mohseni, N. N. Negulyaev, V. S. Stepanyuk, and J. Kirschner. Direct proof of mesoscopic misfit in nanoscale islands by x-ray absorption spectroscopy. *Phys. Rev. B*, 85:125405–125414, 2012.

Bibliography for Chapter 2

[1] D.C. Koningsberger and R. Prins, editors. *X-Ray Absorption: Principles, Applications, Techinques of EXAFS, SEXAFS and XANES*. John Willey & Sons, 1988.

[2] D.C. Koningsberger and R. Prins, editors. *see for example: E.A. Stern, in X-Ray Absorption: Principles, Applications, Techinques of EXAFS, SEXAFS and XANES*. John Willey & Sons, 1988.

[3] D.C. Koningsberger and R. Prins, editors. *P.J. Durham, in X-Ray Absorption: Principles, Applications, Techinques of EXAFS, SEXAFS and XANES*. John Willey & Sons, 1988.

[4] B.K. Teo and D.C.Joy, editors. *B.K. Teo, in EXAFS Spectroscopy: Techniques and Applications*. Plenum Press, 1981.

[5] E.A. Stern. Theory of the extended x-ray-absorption fine structure. *Phys. Rev. B*, 10:3027–3037, 1974.

[6] F. W. Lytle, D. E. Sayers, and E. A. Stern. Extended x-ray-absorption fine-structure technique. ii. experimental practice and selected results. *Phys. Rev. B*, 11:4825–4835, 1975.

[7] E. A. Stern, D. E. Sayers, and F. W. Lytle. Extended x-ray-absorption fine-structure technique. iii. determination of physical parameters. *Phys. Rev. B*, 11:4836–4846, 1975.

[8] E.D. Crozier and A.J. Seary. Asymmetric effects in the EXAFS analysis of solid and liquid Zn. *Can. J. Phys.*, 58:1388–1399, 1980.

[9] D.C. Koningsberger and R. Prins, editors. *E.D. Crozier, in X-Ray Absorption: Principles, Applications, Techinques of EXAFS, SEXAFS and XANES*. John Willey & Sons, 1988.

[10] E.D. Crozier. Impact of the asymmetric pair distribution function in the analysis of XAFS. *Physica B: Cond. Matt.*, 208/209:330–333, 1995.

[11] G. Bunker. Application of the ratio method of EXAFS analysis to disordered systems. *Nucl. Inst. Meth. Phys. Res.*, 207:437–444, 1983.

[12] J. J. Rehr, E. A. Stern, R. L. Martin, and E. R. Davidson. Extended x-ray-absorption fine-structure amplitudes¯wave-function relaxation and chemical effects. *Phys. Rev. B*, 17:560–565, 1978.

[13] John J. Rehr, Joshua J. Kas, Fernando D. Vila, Micah P. Prange, and Kevin Jorissen. Parameter-free calculations of X-ray spectra with FEFF9. *Phys. Chem. Chem. Phys.*, 12:5503–5513, 2010.

[14] S.I. Zabinsky, J.J. Rehr, A. Ankudinov, R.C. Alberts, and M.J. Eller. Multiple-scattering calculations of X-ray-absorption spectra. *Phys. Rev. B*, 52(4):2995–3009, 1995.

[15] J.J. Rehr and R.C. Alberts. Theoretical approaches to X-ray absorption fine structure. *Rev. Mod. Phys.*, 72(3):621–654, 2000.

[16] N. Alberding and E. D. Crozier. Multiple scattering and disorder in extended x-ray-absorption fine-structure analysis. *Phys. Rev. B*, 27:3374–3382, 1983.

[17] D.T. Jiang and E.D. Crozier. Glancing-angle XAFS of buried ultrathin films. *Can. J. Phys.*, 76(8):621–643, 1998.

[18] D.C. Koningsberger and R. Prins, editors. *J. Stöhr, in X-Ray Absorption: Principles, Applications, Techinques of EXAFS, SEXAFS and XANES.* John Willey & Sons, 1988.

[19] E.A. Stern, P. Livins, and Z. Zhang. Thermal vibration and melting from a local perspective. *Phys. Rev. B*, 43(11):8850–8860, 1991.

[20] D.C. Koningsberger and R. Prins, editors. *Sayers, D. E. and Bunker, B. A., in X-Ray Absorption: Principles, Applications, Techinques of EXAFS, SEXAFS and XANES.* John Willey & Sons, 1988.

[21] M. Newville, P. Livins, Y. Jacoby, J.J. Rehr, and E.A. Stern. Near-edge x-ray-absorption fine structure of Pb: A comparison of theory and experiment. *Phys. Rev. B*, 47(21):14126–14131, 1993.

[22] Karl Rudolf Bauchspiess. *A Study of the Pressure-induced Mixed Valence Transition in SmSe and SmS by X-ray Absorption Spectroscopy.* PhD thesis, Simon Fraser University, 1990.

[23] T. Ressler. WinXAS: a Program for X-ray Absorption Spectroscopy Data Analysis under MS-Windows. *J. Synch. Rad.*, 5(2):118–122, 1998.

[24] M. Newville. IFEFFIT: interactive XAFS analysis and FEFF fitting. *J. Synch. Rad.*, 8(2):322–324, 2001.

[25] L.G. Parratt. Surface Studies of Solids by Total Reflection of X-Rays. *Phys. Rev. B*, 95(2):359–369, 1954.

[26] D. Jiang. *Structural Investigations of Metastable Epitaxial Metallic Layers by Glancing-incidence X-ray Absorption Fine Structure*. PhD thesis, Simon Fraser University, 1991.

[27] W. Bambynek, B. Crasemann, R. W. Fink, H.-U. Freund, H. Mark, C. D. Swift, R. E. Price, and P. V. Rao. X-Ray Flourescence Yields, Auger, and Cster-Kronig Transition Probabilities. *Rev. Mod. Phys.*, 44(4):716–813, 1972.

Bibliography for Chapter 3

[1] R. A. Gordon, E. D. Crozier, D.-T. Jiang, J. Shoults, B. Barg, and P. S. Budnik. Characteristics of the MBE1 End-Station at PNC/XOR. *X-RAY ABSORPTION FINE STRUCTURE - XAFS13: 13th International Conference. AIP Conference Proceedings*, 882:887–889, 2007.

[2] T.L. Monchesky. *Magnetoresistance and Magnetic Properties Magnetic Multilayers Grown Directly on GaAs(001)*. PhD thesis, Simon Fraser University, 2000.

[3] T. L. Monchesky, B. Heinrich, R. Urban, K. Myrtle, M. Klaua, and J. Kirschner. Magnetoresistance and Magnetic Properties of Fe/Cu/Fe/GaAs(100). *Phys. Rev. B*, 60:10242–10251, 1999.

[4] P. P. Ewald. Introduction to the dynamical theory of x-ray diffraction. *Acta Crystallographica Section A*, 25(1):103–108, 1969.

[5] E. Bauer. Phänomenologische Theorie der Kristallabscheidung an Oberflächen. I. *Zeitschrift für Kristallographie*, 110:372–394, 1958.

[6] A. Pimpinelli and J. Villain. *Physics of Crystal Growth (Chapter 4)*. Collection Aléa-Saclay. Cambridge University Press, 1998.

[7] S. A. Chambers, F. Xu, H. W. Chen, I. M. Vitomirov, S. B. Anderson, and J. H. Weaver. Simultaneous epitaxy and substrate out-diffusion at a metal-semiconductor interface: Fe/GaAs(001)-c(8x2). *Phys. Rev. B*, 34:6605–6611, 1986.

[8] J. D. Jackson. *Classical Electrodynamics (Chapter 14)*. Wiley, New York, 1998.

[9] H. Winich and S. Doniach. *Synchrotron Radiation Research (Chapter 2)*. Plenum Press, New York, 1980.

[10] B. Lai, A. Khounsary, R. Savoy, L. Moog, and E. Glushkin. Undulator A Characteristics and Specifications. Technical report, Advanced Photon Source, 1993.

[11] S. Heald, E. Stern, D. Brewe, R. Gordon, E. D. Crozier, D.-T. Jiang, and J. Cross. XAFS at the Pacific Northwest Consortium-Collaborative Access Team undulator beamline. *Journal of Synchrotron Radiation*, 8(2):342–344, 2001.

[12] J. A. Bearden and A. F. Burr. Reevaluation of X-Ray Atomic Energy Levels. *Rev. Mod. Phys.*, 39:125–142, 1967.

[13] D. Jiang. *Structural Investigations of Metastable Epitaxial Metallic Layers by Glancing-incidence X-ray Absorption Fine Structure*. PhD thesis, Simon Fraser University, 1991.

[14] D.T. Jiang and E.D. Crozier. Glancing-angle XAFS of buried ultrathin films. *Can. J. Phys.*, 76(8):621–643, 1998.

Bibliography for Chapter 4

[1] T. Ressler. WinXAS: a Program for X-ray Absorption Spectroscopy Data Analysis under MS-Windows. *J. Synch. Rad.*, 5(2):118–122, 1998.

[2] M. Newville, P. Livins, Y. Jacoby, J.J. Rehr, and E.A. Stern. Near-edge x-ray-absorption fine structure of Pb: A comparison of theory and experiment. *Phys. Rev. B*, 47(21):14126–14131, 1993.

[3] C. de Boor. *A Practical Guide to Splines (Chapters IX, X and XI).* Number v. 27 in Applied Mathematical Sciences. Springer-Verlag, 1978.

[4] R.A. Gordon, E.D. Crozier, D.-T. Jiang, P.S. Budnik, T.L. Monchesky, and B. Heinrich. In situ XAFS study of Fe epitaxially grown by MBE on GaAs(001)-4×6. *Surf. Science*, 581:47–57, 2005.

[5] P. S. Budnik, R. A. Gordon, and E. D. Crozier. Structure of the Magnetic Trilayer System Fe/Pd/Fe Epitaxially Grown on GaAs(001)-4×6. *Physica Scripta*, T115:495–497, 2005.

[6] P. S. Budnik, R. A. Gordon, and E. D. Crozier. The Pd/Fe Interface in the Epitaxial System Pd/Fe/GaAs(001)- 4×6. *X-RAY ABSORPTION FINE STRUCTURE - XAFS13: 13th International Conference. AIP Conference Proceedings*, 882:398–400, 2007.

[7] D.C. Koningsberger and R. Prins, editors. *Sayers, D. E. and Bunker, B. A., in X-Ray Absorption: Principles, Applications, Techinques of EXAFS, SEXAFS and XANES.* John Willey & Sons, 1988.

[8] M. Newville. IFEFFIT: interactive XAFS analysis and FEFF fitting. *J. Synch. Rad.*, 8(2):322–324, 2001.

[9] S.I. Zabinsky, J.J. Rehr, A. Ankudinov, R.C. Alberts, and M.J. Eller. Multiple-scattering calculations of X-ray-absorption spectra. *Phys. Rev. B*, 52(4):2995–3009, 1995.

[10] B. Ravell. ATOMS: crystallography for the X-ray absorption spectroscopist. *J. Synchrotron Rad.*, 8(2):314–316, 2001.

[11] T. L. Monchesky, B. Heinrich, R. Urban, K. Myrtle, M. Klaua, and J. Kirschner. Magnetoresistance and Magnetic Properties of Fe/Cu/Fe/GaAs(100). *Phys. Rev. B*, 60:10242–10251, 1999.

Bibliography for Chapter 5

[1] T. L. Monchesky, B. Heinrich, R. Urban, K. Myrtle, M. Klaua, and J. Kirschner. Magnetoresistance and Magnetic Properties of Fe/Cu/Fe/GaAs(100). *Phys. Rev. B*, 60:10242–10251, 1999.

[2] S. Mirbt, B. Sanyal, C. Isheden, and B. Johansson. First-principles calculations of Fe on GaAs(100). *Phys. Rev. B*, 67:155421–155429, 2003.

[3] E.D. Crozier, A.J. Seary, M.K. Manus, and D.-T. Jiang. Effective coordination numbers in ultrathin metalic films. *J. Phys. IV France*, 7, 1997.

[4] Qikun Xue, T. Hashizume, J. M. Zhou, T. Sakata, T. Ohno, and T. Sakurai. Structures of the Ga-rich 4×2 and 4×6 reconstructions of the GaAs(001) surface. *Phys. Rev. Lett.*, 74:3177–3180, 1995.

[5] R.A. Gordon, E.D. Crozier, D.-T. Jiang, T.L. Monchesky, and B. Heinrich. Distorted iron films on GaAs(001)-(4×6). *Phys. Rev. B*, 62:2151–2157, 2000.

[6] W.A. Brantley. Calculated elastic constants for stress problems associated with semiconductor devices. *J. Appl. Phys.*, 44:534–535, 1973.

[7] J. Hornstra and W.J. Bartels. Determination of the lattice constant of epitaxial layers of III-V compounds. *J. Crys. Growth*, 44(5):513–517, 1978.

[8] B. Heinrich, M. Kowalewski, and J.F. Cochran. Engineering of magnetic properties using ultrathin metallic structures prepared by Molecular Beam Epitaxy. *Can. J. Chem*, 77(11):1595–1605, 1998.

[9] S. Chikazumi and S.H. Charap. *Physics of Magnetism.* Wiley, New York, 1964.

[10] E. W. Lee. Magnetostriction and Magnetomechanical Effects. *Rep. Prog. Phys.*, 18(1):184–229, 1955.

[11] Karl Rudolf Bauchspiess. *A Study of the Pressure-induced Mixed Valence Transition in SmSe and SmS by X-ray Absorption Spectroscopy.* PhD thesis, Simon Fraser University, 1990.

[12] O. Thomas, Q. Shen, P. Schieffer, N. Tournerie, and B. Lepine. Interplay between Anisotropic Strain Relaxation and Uniaxial Interface Magnetic Anisotropy in Epitaxial Fe Films on (001) GaAs. *Phys. Rev. Lett.*, 90:017205–017209, 2003.

[13] R. A. Gordon and E. D. Crozier. In-plane structural anisotropy of ultrathin Fe films on GaAs(001)-4×6: X-ray absorption fine-structure spectroscopy measurements. *Phys. Rev. B*, 74:165405–165411, 2006.

[14] Georg Woltersdorf. *Spin-Pumping and Two-Magnon Scattering in Magnetic Multilayers*. PhD thesis, Simon Fraser University, 2004.

[15] Eric E. Fullerton, D. Stoeffler, K. Ounadjela, B. Heinrich, Z. Celinski, and J. A. C. Bland. Structure and magnetism of epitaxially strained Pd(001) films on Fe(001): Experiment and theory. *Phys. Rev. B*, 51:6364–6378, 1995.

[16] C. Boeglin, H. Bulou, J. Hommet, X. Le Cann, H. Magnan, P. Le Fevre, and D. Chandesris. Influence of structural characteristics on magnetic properties in face-centered-tetragonal surface alloy of Fe/Pd(100) ultrathin films. *Phys. Rev. B*, 60:4220–4230, 1999.

[17] H. L. Meyerheim, R. Popescu, and J. Kirschner. No alloying in Fe deposited on Pd(001) at room temperature. *Phys. Rev. B*, 73:245432–245440, 2006.

Bibliography for Appendix A

[1] D.T. Jiang and E.D. Crozier. Glancing-angle XAFS of buried ultrathin films. *Can. J. Phys.*, 76(8):621–643, 1998.

[2] D. Jiang. *Structural Investigations of Metastable Epitaxial Metallic Layers by Glancing-incidence X-ray Absorption Fine Structure.* PhD thesis, Simon Fraser University, 1991.

Bibliography for Appendix B

[1] B. Lai, A. Khounsary, R. Savoy, L. Moog, and E. Glushkin. Undulator A Characteristics and Specifications. Technical report, Advanced Photon Source, 1993.

[2] STI Optronics Inc. APS Undulator A Characteristics. Technical report, Advanced Photon Source, 1998.

[3] D. Attwood. *Soft X-Ray and Extreme Ultraviolet Radiation (Chapter 5).* Cambridge University Press, 2000.

[4] L. Landau and E. Lifshitz. *The Classical Theory of Fields (page 121).* Addison-Wesley, Reading, MA, 1951.

[5] J. D. Jackson. *Classical Electrodynamics (Chapter 14).* Wiley, New York, 1998.

Bibliography for Appendix C

[1] S.I. Zabinsky, J.J. Rehr, A. Ankudinov, R.C. Alberts, and M.J. Eller. Multiple-scattering calculations of X-ray-absorption spectra. *Phys. Rev. B*, 52(4):2995–3009, 1995.

[2] E.D. Crozier, A.J. Seary, M.K. Manus, and D.-T. Jiang. Effective coordination numbers in ultrathin metalic films. *J. Phys. IV France*, 7(2):251–252, 1997.